Investigating Heavy-Ion Internuclear Potentials Using Inversion And Other Methods

Thesis

Investigating Heavy-Ion Internuclear Potentials Using Inversion and Other Methods

by

Michael Anthony Russell, B.A.(Hons)

A thesis submitted to the Faculty of Science at the Open University for the degree of Master of Philosophy

Department of Physics and Astronomy, the Open University

December 2000

ProQuest LLC.
789 East Eisenhower Parkway
P.O. Box 1346
Ann Arbor, MI 48106 – 1346

Abstract

The interaction of heavy-ion nuclei via the strong nuclear force can be usefully approximated by a mean-field local potential. Such potentials contain much information concerning nuclear structure and the relative importance and radial dependence of the various reaction channels involved in the interaction. Existing methods of fitting optical potentials to scattering cross-sections, both model-dependent and -independent, have various problems. Phenomenology based on S-matrix fitting followed by iterative-perturbative (IP) inversion enables us to obtain fits to the cross-section with $\chi^2/N \sim 1$. The calculations in this thesis represent an exploration of the viability of the IP method applied to heavy-ion scattering.

There are two parts to the thesis. The first uses the IP method to investigate the heavy-ion phenomenological potential, in particular ^{16}O+^{12}C at $E_{\rm lab} = 608$ MeV and ^{12}C+^{12}C from $E_{\rm lab} = 159$ to 2400 MeV. The second uses the IP method in conjunction with coupled reaction channels calculations to examine the dynamic polarization potentials which represent the contribution of specific reaction channels to the heavy-ion interaction. This is applied to the case of ^{16}O+^{62}Ni near the Coulomb threshold, specifically to investigate the quadrupole Coulomb DPP, and the fusion cross-section and spin distribution. Both parts of the thesis are therefore linked by a common thread—the use of the IP inversion methodology to understand the heavy-ion interaction at low and intermediate energies.

Contents

List of Figures

List of Tables

Chapter 1

Introduction

This thesis will investigate the heavy-ion interaction potential at energies close to the Coulomb barrier, using S-matrix-to-potential inversion (the iterative-perturbative method) and coupled reaction channels calculations.

The interaction of heavy-ion nuclei is in general very complicated; however, in many cases such interactions can be reduced to a complex local mean-field potential called the 'optical potential'. Although it is at first sight surprising that the interaction of such composite bodies as heavy-ion nuclei via the strong nuclear force can be usefully approximated by a mean-field local potential, such potentials are extremely useful and contain much information concerning nuclear structure and the relative importance and radial dependence of the various reaction channels involved in the interaction.

Two of the main questions concerning the representation of heavy-ion nuclear interactions by local optical potentials are (i) how unique are such potentials?, and (ii) how accurate are they? Existing methods of fitting optical potentials to scattering

cross-sections, both model-dependent and -independent, have various problems. While the usual methods (such as Woods-Saxon fitting, or folding model potentials) may be useful for investigating systematics over bombarding energy or other parameters, it should be asked how accurate and meaningful they are when considered in isolation for a given energy or over a restricted radial range. The non-linearity involved in obtaining a local potential from elastic scattering data means that there may exist several possible 'families' of potentials, each with different physical characteristics, which all give an acceptably accurate fit to the scattering data. Only one of these families will be the 'correct' set of solutions, and to select which it is, further criteria must be applied, such as consistency with accurate local potentials at nearby energies (i.e., 'smoothness' over the energy range) and for nearby atomic masses (i.e., 'smoothness' over the atomic number range), or general physical considerations.

Phenomenology based on S-matrix fitting followed by inversion enables us to obtain fits to the scattering cross-section with $\chi^2/N \sim 1$. Such an accurate model-independent inversion technique is potentially very powerful when applied to the case of heavy-ion scattering, and it is one of the main purposes of the first part of this thesis to investigate the radial shape (which is usually rigidly constrained by many other fitting methods) and depth at certain radial ranges, of potentials which accurately fit the scattering data. Furthermore, the same inversion method can be applied to obtain accurate local potentials which represent the contribution of particular reaction channels to the interaction. The radial shape and relative depths of these dynamic polarization potentials (DPP) can then be investigated, to yield information about the relative

importance of such channels to the interaction and their physical characteristics.

Because of the non-linear relationship between the potentials and the scattering cross-section, there are ambiguity problems involved whenever elastic scattering data is fitted with a potential model. A methodology based on phase shift fitting followed by inversion is not immune to these ambiguity problems; however, because of the wide range of 'starting reference potentials' (SRPs) and possible sets of basis functions required by the inversion method, together with the high level of accuracy of inversion, our method can be used to explore the solution space to identify the different families of inverse potentials which fit the scattering data, and physical considerations can often be used to select one particular solution family as the most physically reasonable. This is quite difficult for a methodology such as Woods-Saxon fitting, which is 'locked in' to a particular radial form for the potential, or folding model potentials, which can only vary the normalisation of the potential.

This thesis is divided into two parts. The first is devoted to using the iterative-perturbative inversion methodology to investigate the heavy-ion phenomenological optical model at intermediate energies, in particular the cases of ^{16}O on ^{12}C at $E_{\rm lab} = 608$ MeV and ^{12}C on ^{12}C from $E_{\rm lab} = 159$ to 2400 MeV. An introduction to the iterative-perturbative inversion method which is used throughout this thesis is contained in Chapter 3, Section 3.1. The first part of the thesis consists of Chapters 2 and 3.

The second part of this thesis uses coupled reaction channels calculations and the iterative-perturbative inversion method to examine the dynamic polarization potentials representing the contribution of particular reaction channels to the interaction. We

investigate especially the case of ^{16}O on ^{62}Ni near the Coulomb threshold. The second part of this thesis consists of Chapters 4 and 5. A sixth chapter, containing some general conclusions relating to both parts of the work, ends the thesis.

The two parts of the thesis are complementary, with the first part introducing the inversion methodology to be used throughout the thesis and applying that methodology to important examples of heavy-ion scattering over a range of energies. The second part extends the methodology by using coupled reaction channels calculations to obtain S-matrices representing the contribution of particular reaction channels to the scattering. These S-matrices can then be inverted using the iterative-perturbative method to obtain accurate dynamic polarization potentials representing the contribution of those channels to the interaction potential. The two parts are therefore linked by a common thread — the use of a highly accurate inversion methodology to understand the heavy-ion nucleus-nucleus interaction at low and intermediate energies.

Part I

Heavy-ion phenomenology by inversion

Chapter 2

The heavy-ion phenomenological optical model

In this chapter, I shall present a brief description of basic scattering theory, together with an introduction to the heavy-ion optical model.

Section 2.1 is divided into three parts: the scattering of chargeless and spinless particles, the scattering of charged spinless particles, and finally a few paragraphs presenting the inverse scattering problem.

Section 2.2 gives an introduction to the concept of the heavy-ion optical model, which uses a mean-field potential to represent the many-body scattering of heavy ions. This thesis will be devoted to an investigation of some of the properties of these heavy-ion mean-field potentials. Section 2.2 is in three parts, dealing in turn with the derivation of the optical model via the truncation of the scattering wavefunction and the use of an effective interaction, the phenomenological optical model, and the microscopic

optical model which is based upon the more fundamental nucleon-nucleon interaction. A more detailed treatment of the optical model using the Feshbach formalism will be given in Chapter 4.

2.1 Elastic scattering theory

I shall be concerned with elastic nuclear scattering, in which the internal energies of the target and projectile are unchanged by the collision. The projectile-target interaction, $V(r)$, will be spherically symmetric, depending only on r, the distance between the centres of mass of the two nuclei. The centre-of-mass frame will be used, with an equation of motion for a single particle with position r moving in the potential $V(r)$, with reduced mass of the system $\mu = \frac{m_1 m_2}{(m_1+m_2)}$, and centre-of-mass energy $E_{\rm cm} = \frac{m_2}{(m_1+m_2)} E_{\rm lab}$, where $E_{\rm lab}$ is the laboratory energy of the projectile and m_1 and m_2 are the masses of the projectile and the target respectively.

The total internuclear potential is $V_{\rm tot}(r) = V_{\rm Cou}(r) + V_{\rm nuc}(r)$, where $V_{\rm nuc}(r)$ is the nuclear part of the total potential between the two particles and $V_{\rm Cou}(r)$ is the Coulomb term. I first describe the direct scattering theory for chargeless (and spin-zero) particles, and then extend the description to deal with the Coulomb interaction between the nuclei. The charge-free case will be presented first, since the analysis is simpler for potentials which go to zero faster than $1/r$ for large r.

2.1.1 The scattering of chargeless and spinless particles

To solve the 'direct' scattering problem (i.e., $V(r) \rightarrow \sigma(\theta)$) for chargeless and spinless particles, we solve the Schrödinger equation for $V_{\rm nuc}(r)$, and impose the appropriate boundary conditions. In fact, we only need to find steady-state solutions of the time-independent Schrödinger equation:

$$\nabla^2\psi + \frac{2\mu}{\hbar^2}(E_{\rm cm} - V_{\rm nuc}(r))\psi = 0. \tag{2.1}$$

Correct boundary conditions must be imposed on the solutions of Eq. 2.1. For elastic scattering by a central potential, the wavefunction at large distances will consist of the incident plane wave plus a outgoing scattered wave with axial symmetry multiplied by a complex function of the polar scattering angle θ, which will depend on the form of the potential. That is,

$$\psi \underset{r\rightarrow\infty}{\longrightarrow} \mathrm{e}^{ikz} + f(\theta)\frac{\mathrm{e}^{ikr}}{r} = \psi_{\rm inc} + \psi_{\rm sc}, \tag{2.2}$$

where $\psi_{\rm inc}$ is the incident plane wave and $\psi_{\rm sc}$ is the scattered wave.

The wavefunction can be decomposed into 'partial waves', each of which has a definite value of l (the orbital angular momentum quantum number) associated with it. This allows us to separate the spherical variables in the Schödinger equation, and solve immediately for the non-radial variables θ and ϕ since $V(r)$ is radial. Since the strong nuclear force has only a short range, only the partial waves below some maximum value

$l_{\max}$ need be included, thus reducing the number of one-dimensional radial equations (labelled by l) to a (usually) manageable level. For heavy ions, this maximum value of l is typically of the order of a few hundred.

The incident plane wave for neutral spinless particles e^{ikz} can be written as a superposition of spherical partial waves:

$$\psi_{\text{inc}} = e^{ikz} = \sum_{l=0}^{\infty} i^l (2l+1) j_l(kr) P_l(\cos\theta). \tag{2.3}$$

The angular functions $P_l(\cos\theta)$ are Legendre polynomials, and the radial functions $j_l(kr)$ are the spherical Bessel functions, which are regular at the origin and are asymptotic solutions of the radial part of the Schrödinger equation as $V_{\text{nuc}} \to 0$. The spherical Bessel functions have the useful asymptotic property that

$$j_l(kr) \underset{r\to\infty}{\longrightarrow} \frac{\sin(kr - l\pi/2)}{kr} = i\frac{e^{-i(kr-l\pi/2)} - e^{+i(kr-l\pi/2)}}{2kr}, \tag{2.4}$$

so that we can write

$$\psi_{\text{inc}} = \frac{1}{2kr} \sum_{l=0}^{\infty} i^{l+1} (2l+1)[e^{-i(kr-l\pi/2)} - e^{+i(kr-l\pi/2)}] P_l(\cos\theta). \tag{2.5}$$

The first term represents an incoming and the second an outgoing spherical wave.

Scattering changes both the phase and amplitude of the outgoing waves. Any change in amplitude will be caused by inelastic processes and nuclear reactions taking flux out of the elastic channel, thereby decreasing the amplitude of the outgoing wave.

We represent the change in the l'th outgoing partial wave by the complex coefficient S_l, called the scattering-matrix element:

$$\psi \underset{r\to\infty}{\longrightarrow} \frac{1}{2kr}\sum_{l=0}^{\infty} i^{l+1}(2l+1)[e^{-i(kr-l\pi/2)} - S_l e^{+i(kr-l\pi/2)}]P_l(\cos\theta). \tag{2.6}$$

These scattering-matrix, or S-matrix, elements can be written in the form $|S_l|e^{2i\delta_l}$, where δ_l is a real number. $|S_l|$ is a measure of the absorption of the corresponding partial wave; a small value of $|S_l|$ corresponds to strong absorption; $|S_l|$ is often called the 'reflection coefficient'. The physical significance of δ_l can be seen if we substitute the expression for the S-matrix elements into the l'th term of Eq. 2.6; we find that ψ_l is asymptotically proportional to:

$$\frac{1}{2kr} i^{l+1}(2l+1)[e^{-i(kr-l\pi/2)} - |S_l|e^{+i(kr-l\pi/2+2\delta_l)}]P_l(\cos\theta) \tag{2.7}$$

Compared with Eq. 2.5, this has the same radial form as the corresponding partial wave of the incident plane wave, $\psi_{\mathrm{inc},l}$, except that the outgoing spherical wave has been phase shifted.

To find the scattered wave, we subtract the asymptotic equation for ψ_{inc} from the one for ψ itself:

$$\begin{aligned} \psi_{\mathrm{sc}} &\longrightarrow \frac{1}{2kr}\sum_{l=0}^{\infty} i^{l+1}(2l+1)(1-S_l)e^{i(kr-l\pi/2)}P_l(\cos\theta) \\ &= \frac{e^{ikr}}{r}\frac{1}{2ik}\sum_{l=0}^{\infty}(2l+1)(S_l-1)P_l(\cos\theta). \end{aligned} \tag{2.8}$$

Comparing Eqs. 2.2 and 2.8, we see that the complex scattering amplitude $f(\theta)$ is related to the scattering-matrix elements S_l by the expression:

$$f(\theta) = \frac{1}{2ik}\sum_{l=0}^{\infty}(2l+1)(S_l - 1)P_l(\cos\theta). \tag{2.9}$$

The elastic differential cross-section, $\frac{d\sigma_{el}}{d\Omega}(\theta)$, is defined to be the ratio of the flux through a given element of solid angle $d\Omega$ to the incident flux, per unit solid angle. Clearly,

$$|\mathbf{j}_{inc}| = \frac{\hbar}{2i\mu}(\psi^*_{inc}\nabla\psi_{inc} - \psi_{inc}\nabla\psi^*_{inc}) \rightarrow \frac{\hbar k}{\mu} \tag{2.10}$$

(since $\hbar k/\mu$ is the speed v of the particles in the beam, $|\mathbf{j}_{inc}|$ corresponds to v particles crossing a unit area of the incident beam per second). In the same way,

$$|\mathbf{j}_{sc}| = \frac{\hbar}{2i\mu}(\psi^*_{sc}\nabla\psi_{sc} - \psi_{sc}\nabla\psi^*_{sc}) \rightarrow \frac{\hbar k}{\mu r^2}|f(\theta)|^2. \tag{2.11}$$

Since the element of area on the surface of a sphere is $r^2 d\Omega$, it follows that the probability current passing through a given element of solid angle $d\Omega$ must be $(\hbar k/\mu)|f(\theta)|^2 d\Omega$.

The elastic differential cross-section for chargeless and spinless non-identical particles is then given by

$$\frac{d\sigma_{el}}{d\Omega}(\theta) = |f(\theta)|^2, \tag{2.12}$$

while in the case of identical chargeless and spinless particles it is given by

$$\frac{d\sigma_{el}}{d\Omega}(\theta) = |f(\theta) + f(\pi - \theta)|^2. \tag{2.13}$$

It follows that $\frac{d\sigma_{el}}{d\Omega}(\theta)$ for chargeless and spin-zero non-identical particles is related to the S-matrix elements by the formula:

$$\frac{d\sigma_{el}}{d\Omega}(\theta) = \frac{1}{4k^2}\left|\sum_{l=0}^{\infty}(2l+1)(S_l-1)P_l(\cos\theta)\right|^2. \tag{2.14}$$

The foregoing analysis is, however, only applicable to the case of spinless neutral pion or neutron scattering, which obviously does not occur in nature. To make the discussion physically realistic, we must therefore introduce the long-range Coulomb potential into the analysis.

2.1.2 The scattering of charged spinless nuclei

When there is a Coulomb interaction between the two nuclei, we can no longer use Eq. 2.2 for the asymptotic form of the scattering wavefunction ψ. Because of the long range of the Coulomb potential, we must modify the asymptotic form of ψ. Since the analytic solutions of the wave equation for two point particles interacting purely by means of a Coulomb potential are well known [1], it is convenient to describe the scattering of charged particles starting from these Coulomb-distorted waves instead of the plane and spherical waves of Eq. 2.2. We accordingly replace the plane wave ψ_{inc} in Eq. 2.2 with the wave for purely Coulomb (ie, Rutherford) scattering of point charges, $\psi_{inc,Cou}$, which has the form $(1+\frac{\eta^2}{ik(r-z)})\exp(ikz+i\eta\ln k(r-z))$. The symbol η represents the Sommerfeld (or Coulomb) parameter, $\frac{\mu Z_1 Z_2 e^2}{4\pi\varepsilon_0\hbar^2 k}$. If the projectile or target were uncharged (ie, $\eta \to 0$), we would of course have $\psi_{inc,Cou} \to e^{ikz}$. The

radial part of the asymptotic scattered wave in Eq. 2.2, $\psi_{\rm sc}$, is likewise replaced by the wavefunction $\frac{1}{r}\exp(ikr - i\eta \ln 2kr)$ which has a phase shift (relative to the undisturbed wave $\frac{1}{r}\exp ikr$) which depends logarithmically on the distance r. The presence of the Coulomb field also modifies the scattering amplitude $f(\theta)$ (and the corresponding S_l) due to the purely nuclear part of the potential relative to what would be obtained in the absence of the Coulomb field. For example, a repulsive Coulomb barrier tends to shield the specifically nuclear interactions, thereby modifying the scattering for a given nuclear potential $V_{\rm nuc}(r)$.

The asymptotic form of the scattering wavefunction is now

$$\begin{aligned} \psi &\longrightarrow \left(1 + \frac{\eta^2}{ik(r-z)}\right) \exp(ikz + i\eta \ln k(r-z)) + f_{\rm tot}(\theta)\frac{e^{i(kr - \eta \ln 2kr)}}{r} \qquad (2.15) \\ &= \psi_{\rm inc,Cou} + f_{\rm tot}(\theta)\psi_{\rm sc,Cou} \end{aligned}$$

instead of Eq. 2.2. The Coulomb-distorted waves, $\psi_{\rm inc,Cou}$ and $\psi_{\rm sc,Cou}$ can still be interpreted as incident and scattered waves because the current density $\mathbf{j}_{\rm inc}$ calculated from $\psi_{\rm inc,Cou}$ is directed along the positive z-axis and has magnitude $\hbar k/\mu r^2 = v$ at large negative values of z, and the current density $\mathbf{j}_{\rm sc}$ calculated from $\psi_{\rm sc,Cou}$ is directed radially outwards from the scattering centre and has magnitude $v|f_{\rm Cou}|^2/r^2$ at large values of r.

Since the Coulomb-distorted waves now implicitly include the effect of purely Rutherford scattering, the $f_{\rm nuc}(\theta)$ scattering amplitude now describes the effect on the scattering of any *additional* interactions beyond the Coulomb for point particles, as

well as any modification to the Rutherford scattering due to the charges of the nuclei being spread over a finite region of space rather than concentrated at a point. The total scattering amplitude can therefore be written as the sum of two terms:

$$f_{\rm tot}(\theta) = f_{\rm Cou}(\theta) + f_{\rm nuc}(\theta), \tag{2.16}$$

where $f_{\rm Cou}(\theta)$ is the well-known Rutherford scattering amplitude:

$$f_{\rm Cou}(\theta) = -\frac{\eta}{2k\sin^2(\theta/2)} \exp(-i\eta \ln(\sin^2(\theta/2)) + 2i\sigma_0), \tag{2.17}$$

and $|f_{\rm Cou}(\theta)|^2$ is the Rutherford cross-section [1].

The partial wave expansion is still valid, and the expansion of the scattering wavefunction for pure Rutherford scattering is:

$$\psi = \sum_{l=0}^{\infty} i^l (2l+1) {\rm e}^{i\sigma_l} F_l(kr) P_l(\cos\theta). \tag{2.18}$$

The Coulomb functions $F_l(kr)$ have the following asymptotic behaviour as $r \to \infty$:

$$\begin{aligned} F_l(kr) &\longrightarrow \frac{\sin(kr - l\pi/2 - \eta \ln 2kr + \sigma_l)}{kr} \\ &= i\frac{{\rm e}^{-i(kr - l\pi/2 - \eta \ln 2kr + \sigma_l)} - {\rm e}^{i(kr - l\pi/2 - \eta \ln 2kr + \sigma_l)}}{2kr}, \end{aligned} \tag{2.19}$$

where σ_l is called the Coulomb phase shift because the l'th part of the scattering wave

ψ for pure Coulomb scattering has the asymptotic form

$$\frac{\sin(kr - l\pi/2 - \eta \ln 2kr + \sigma_l)}{kr}, \tag{2.20}$$

which is just like the phase-shifted scattering wave of Eq. 2.7 for purely nuclear scattering except for the additional logarithmic term. The Coulomb phase shifts are defined by the equation $e^{2i\sigma_l} = \Gamma(1 + l + i\eta)/\Gamma(1 + l - i\eta)$. We can therefore write ψ as

$$\psi \underset{r\to\infty}{\longrightarrow} \frac{1}{2kr} \sum_{l=0}^{\infty} i^{l+1}(2l+1)(e^{-i(kr-l\pi/2-\eta \ln 2kr)} - e^{2i\sigma_l} e^{i(kr-l\pi/2-\eta \ln 2kr)}) P_l(\cos\theta). \tag{2.21}$$

Eq. 2.21 is the direct analogue, for scattering by a pure Coulomb potential, of Eq. 2.6 for a pure nuclear potential.

The l'th partial wave of the Coulomb-distorted ψ can still be thought of as an incoming wave superposed on a modified outgoing wave, $I_l - S_l O_l$, but the incoming and outgoing waves are now Coulomb wavefunctions, $\frac{1}{r}\exp(\pm i(kr - l\pi/2 - \eta \ln 2kr))$, rather than the simpler spherical waves $\frac{1}{r}\exp(\pm i(kr - l\pi/2))$ derived from the Bessel function in Eq. 2.4.

When the total potential $V_{\text{tot}}(r)$ contains both a long-range Coulomb term $V_{\text{Cou}}(r)$ and a short-range nuclear term $V_{\text{nuc}}(r)$, then the asymptotic behaviour of ψ must be compared with that of the Coulomb functions F_l rather than the spherical Bessel functions j_l in order to obtain the phase shifts δ_l. These phase shifts are the *additional* phase shifts due to the specifically nuclear potential $V_{\text{nuc}}(r)$ and the difference between the Coulomb potential due to nuclear charges of finite size and that due to point

charges.

Since $e^{2i(\sigma_l+\delta_l)} - 1 = (e^{2i\sigma_l} - 1) + e^{2i\sigma_l}(e^{2i\delta_l} - 1)$ (where δ_l may now be complex to allow for absorption), the total scattering amplitude can be separated into two terms:

$$f_{\rm tot} = \frac{1}{2ik}\sum_{l=0}^{\infty}(2l+1)(e^{2i\sigma_l}-1)P_l(\cos\theta) + \frac{1}{2ik}\sum_{l=0}^{\infty}(2l+1)e^{2i\sigma_l}(e^{2i\delta_l}-1)P_l(\cos\theta). \quad (2.22)$$

The first of these terms can be identified with $f_{\rm Cou}(\theta)$, the scattering amplitude for pure Rutherford scattering given in Eq. 2.17, and the second term,

$$f_{\rm nuc}(\theta) = \frac{1}{2ik}\sum_{l=0}^{\infty}(2l+1)e^{2i\sigma_l}(S_l-1)P_l(\cos\theta), \quad (2.23)$$

is the expansion of $f_{\rm nuc}(\theta)$ for charged particles corresponding to Eq. 2.9 for neutral particles.

The Coulomb effects show themselves explicitly not only through the $f_{\rm Cou}(\theta)$ term in the total scattering amplitude, but also through the appearance of the Coulomb phase shifts in the amplitude $f_{\rm nuc}(\theta)$ in Eq. 2.23. This presence of the Coulomb phase shifts in the expression for $f_{\rm nuc}(\theta)$ is very significant. It means that 'switching off' the Coulomb potential does not simply eliminate $f_{\rm Cou}(\theta)$ from the expression for $f_{\rm tot}(\theta)$; it also modifies $f_{\rm nuc}(\theta)$. Furthermore, the phase shifts δ_l themselves are also modified by the presence of the Coulomb field compared to what they would have been if the particles were uncharged. This has important implications concerning the additivity of phase shifts. If we consider the phase shifts describing the scattering from two

potentials V and U when these potentials act singly or together, we find that

$$\delta_l(V+U) = \delta_l^U(V) + \delta_l(U) \neq \delta_l(V) + \delta_l(U), \tag{2.24}$$

where $\delta_l(V+U)$ is the phase shift due to potentials V and U acting together, $\delta_l(V)$ is that due to V alone (and likewise with $\delta_l(U)$), and $\delta_l^U(V)$ is the phase shift due to the potential V acting in the presence of the potential U.

The same conclusion is still valid even if U is a long-range Coulomb potential, so that the phase shift $\delta_l^U(V)$ is the additional phase shift due to scattering from a short-range nuclear potential V (plus a correction to the Coulomb potential due to the charges being of finite size) in the presence of a point Coulomb potential.

The differential cross-section for scattering from the potential $V_{\rm tot}(r)$ is simply

$$\begin{aligned} \frac{\mathrm{d}\sigma_{\rm el}}{\mathrm{d}\Omega}(\theta) &= |f_{\rm Cou}(\theta) + f_{\rm nuc}(\theta)|^2 \\ &= \left| f_{\rm Cou}(\theta) + \frac{1}{2ik}\sum_{l=0}^{\infty}(2l+1)\mathrm{e}^{2i\sigma_l}(S_l-1)P_l(\cos\theta) \right|^2 . \end{aligned} \tag{2.25}$$

The two amplitudes $f_{\rm Cou}(\theta)$ and $f_{\rm nuc}(\theta)$ interfere.

The Rutherford amplitude $f_{\rm Cou}(\theta)$ (Eq. 2.17) is inversely proportional to the bombarding energy E; it therefore becomes less important as the bombarding energy increases, so that the 'nuclear' amplitude $f_{\rm nuc}(\theta)$ begins to dominate the scattering. However, as Eq. 2.17 shows, $f_{\rm Cou}(\theta)$ diverges for $\theta = 0$, so that it is never negligible at the smallest angles. This divergence is due to the long-range of the Coulomb field —

even particles at arbitrarily large values of r will be deflected to some extent.

Since we are concerned with the elastic scattering of heavy ions, the semi-classical approximation will usually be a good one. This allows us to define a semi-classical deflection function, which will be given by the simple expression

$$\Theta_l = 2\frac{\partial}{\partial l}(\sigma_l + \delta_l), \tag{2.26}$$

where σ_l is the Coulomb phase shift and δ_l is the nuclear phase shift for the l'th partial wave. Since the Coulomb phase shifts are known analytically, the deflection function is just

$$\Theta_l = 2\arctan\frac{\eta}{l} + 2\frac{\partial}{\partial l}\delta_l. \tag{2.27}$$

2.1.3 The inverse scattering problem

We can solve the *direct scattering problem* for elastic scattering from a central potential $V(r)$ by solving the Schrödinger equation with appropriate boundary conditions to obtain the S-matrix elements (or, equivalently, the nuclear phase shifts), and using Eq. 2.25 to calculate the elastic differential cross-section (which is the quantity actually observed in a scattering experiment). This procedure can be represented schematically as follows:

$$V(r) \rightarrow S \rightarrow \frac{\mathrm{d}\sigma_{\mathrm{el}}}{\mathrm{d}\Omega}. \tag{2.28}$$

However, given the fact that it is the quantity $\frac{\mathrm{d}\sigma_{\mathrm{el}}}{\mathrm{d}\Omega}$ which is observed experimentally, it is interesting to ask if we can solve the *inverse scattering problem*; that is,

can we reverse the direction of the arrows in the above scheme? It should be noted that this presents *two* inverse problems which can be considered separately— $\frac{d\sigma_{el}}{d\Omega}$-to-$S$ inversion and S-to-$V(r)$ inversion. The first part of this thesis will involve both inverse problems, while the second part will be concerned with only the second, along with coupled reaction channels calculations.

It is, in fact, possible to solve the inverse problem, but at the cost of introducing ambiguities into the calculation, especially when obtaining S-matrix elements that yield a given $\frac{d\sigma_{el}}{d\Omega}$. It turns out that many quite different sets of S-matrix elements are capable of yielding the same differential cross-section [2]. This is the problem of phase shift ambiguity, and it is one of the factors which make inverse scattering more difficult than direct scattering. Having said this, however, it is actually possible to eliminate many of the inherent ambiguities in fitting phase shifts to scattering data by imposing *a priori* conditions on the behaviour of the S-matrix elements; for example, by insisting on continuity and smoothness as a function of l or E. This is especially useful for heavy ion scattering, where many hundreds of partial waves may participate in the scattering.

The ambiguities involved in S-matrix to potential inversion are somewhat different to those involved in cross-section to S-matrix inversion. It turns out that, in nuclear scattering, the internuclear potential is very often a non-local and l-dependent one. The ambiguities involved in solving the inverse scattering problem for non-local and l-dependent potentials are very great, since there is far too much freedom to choose parametrized forms. However, for every non-local and l-dependent potential there ex-

ists an 'equivalent' local and l-independent potential — 'equivalent' in the sense that it reproduces the observed differential cross-section just as well as the 'true' non-local and l-dependent potential. Specifically, S-matrix-to-potential inversion is always possible in principle.

2.2 The heavy-ion optical model

It is not *a priori* obvious that the many-body problem of heavy-ion scattering can be described adequately using only the simple model of two particles interacting via a smooth potential which behaves in a regular way with energy. The optical model is a mean-field approach to the problem of nuclear scattering, and our aim is to find a potential which describes smooth variations of the elastic scattering cross-section as a function of the bombarding energy and target nucleon number, E and A.

In the following three subsections, we shall (i) give a derivation of the optical model potential using the Feshbach formalism of projection operators, (ii) describe some semi-empirical phenomenological forms of the optical model potential, and (iii) describe some of the microscopic optical potentials, which are based upon the more fundamental nucleon-nucleon interactions.

2.2.1 Truncation of the wavefunction— the effective interaction

We wish to solve the time-independent Schrödinger equation for a given Hamiltonian:

$$(E - H)\Psi = 0. \tag{2.29}$$

Since we are interested in solving the equation for only a few channels, it is sensible to introduce a projection operator which projects the total wavefunction Ψ onto a subspace containing only those particular channels in which we are interested. In what follows, we shall be even more restrictive and assume that we wish to find only the elastic part of the wavefunction. Following the Feshbach formalism [3, 4, 5], we therefore define a projection operator P such that $P\Psi = \chi_0\Phi_0$, where $\chi_0\Phi_0$ is that part of the total wavefunction for which the scattering system is in its ground state (χ_0 is the radial part of the wavefunction, and Φ_0 the product of the ground states of both nuclei). The appropriate form for P in this case is $P = |\Phi_0 >< \Phi_0|$. A complementary projection operator Q can be defined such that $Q = 1 - P$, so that $P\Psi + Q\Psi = \Psi$. It can easily be seen that $P^2\Psi = P\Psi$, $Q^2\Psi = Q\Psi$ and $PQ\Psi = QP\Psi = 0$. What we have done is to introduce a model wavefunction $\Psi_{\text{model}} = P\Psi$ by truncating the total wavefunction Ψ to a few basis states (in this case only the ground states of both nuclei). The truncation can be compensated for by replacing the original Hamiltonian with an effective one.

The Schrödinger equation can be trivially rewritten as

$$(E - H)(P\Psi + Q\Psi) = 0. \tag{2.30}$$

By applying the projection operators P or Q from the left, and using the properties of P and Q described above, we can obtain a pair of coupled equations relating $P\Psi$ and $Q\Psi$:

$$\begin{aligned} (E - PHP)P\Psi &= (PHQ)Q\Psi \\ (E - QHQ)Q\Psi &= (QHP)P\Psi. \end{aligned} \tag{2.31}$$

We can eliminate $Q\Psi$ from the first equation by formally expressing it as:

$$Q\Psi = \frac{1}{E^{(+)} - QHQ}(QHP)P\Psi. \tag{2.32}$$

The algebraic manipulation must be treated with caution, however, since $(E^{(+)} - QHQ)^{-1}$ is an integral operator rather than a number. To avoid divergence, and to guarantee that the solution is an outgoing wave when $Q\Psi$ includes one or more open channels, an infinitesimal imaginary quantity $i\varepsilon$ is added to the energy E, so that $E^{(+)} = E + i\varepsilon$. The operator $(E^{(+)} - QHQ)^{-1}$ implicitly contains multiple scattering in the $Q\Psi$ subspace to all orders.

The Schrödinger equation for $P\Psi$ can therefore be written in the form

$$(E - \mathcal{H})P\Psi = 0, \tag{2.33}$$

where the effective Hamiltonian $\mathcal{H}$ has the form

$$\mathcal{H} = PHP + PHQ\frac{1}{E^{(+)} - QHQ}QHP. \tag{2.34}$$

The notation can be abbreviated if we let $P\Psi = \Psi_P$, $Q\Psi = \Psi_Q$, $QHP = H_{QP}$ etc., so that

$$\mathcal{H} = H_{PP} + H_{PQ}\frac{1}{E^{(+)} - H_{QQ}}H_{QP}. \tag{2.35}$$

The physical interpretation of the effective Hamiltonian is quite straightforward. Reading it from right to left (since these are operators), H_{QP} represents an excitation of the system from the $P\Psi$ subspace into the $Q\Psi$ subspace, the propagator $(E^{(+)} - H_{QQ})^{-1}$ represents the multiple interactions in the $Q\Psi$ subspace to all orders, and H_{PQ} represents the de-excitation of the system back into the $P\Psi$ subspace to contribute to the elastic scattering. The H_{PP} term simply represents the interaction which would be expected if the $P\Psi$ subspace were equal to the total wavefunction.

The Schrödinger equation is therefore

$$\left\{E - H_{PP} - H_{PQ}\frac{1}{E^{(+)} - H_{QQ}}H_{QP}\right\}\Psi_P = 0. \tag{2.36}$$

If we multiply the equation from the left by $< \Phi_0|$ and integrate over the internal coor-

dinates, we obtain an equation for the relative motion part of the elastic wavefunction, χ_0:

$$\left\{E - < \Phi_0|H|\Phi_0 > - < \Phi_0|HQ\frac{1}{E^{(+)} - H_{QQ}}QH|\Phi_0 >\right\}\chi_0 = 0. \tag{2.37}$$

Solving this equation, with the effective interaction, gives us the optical model elastic wavefunction.

If we choose the zero point of our energy scale to be the ground state energy of the system (as is the usual practice), then we can write Eq. 2.37 as

$$\left\{E - T_0 - < \Phi_0|V|\Phi_0 > - < \Phi_0|VQ\frac{1}{E^{(+)} - H_{QQ}}QV|\Phi_0 >\right\}\chi_0 = 0, \tag{2.38}$$

where V is the interaction potential, E is the centre-of-mass energy and T_0 is the kinetic energy.

Eq. 2.37 can be written in the abbreviated form

$$(E - T_0 - \mathcal{V})\chi_0 = 0, \tag{2.39}$$

where the equivalent potential $\mathcal{V}(\mathbf{r})$ is just

$$\mathcal{V} = < \Phi_0|V|\Phi_0 > + < \Phi_0|VQ\frac{1}{E^{(+)} - H_{QQ}}QV|\Phi_0 > . \tag{2.40}$$

If we let $V_0 = < \Phi_0|V|\Phi_0 >$ and

$$\Delta V(E) = < \Phi_0|VQ\frac{1}{E^{(+)} - H_{QQ}}QV|\Phi_0 >, \tag{2.41}$$

then we can write the Schrödinger equation in a concise form:

$$(E - T_0 - V_0 - \Delta V(E))\chi_0 = 0, \tag{2.42}$$

where $\Delta V(E)$ is an energy dependent complex-valued correction to V_0 which takes account of the contributions to the elastic scattering amplitude from virtual (Re ΔV) and actual (Im ΔV) excitations into the omitted channels in the $Q\Psi$ subspace. It is often called the 'dynamic polarization potential' (DPP). The energy dependence of $\Delta V(E)$ is due to the fact that the probability of transitions into and out of the eliminated Q channels will depend on the bombarding energy of the projectile; as the energy increases above the Coulomb threshold, for example, more channels become open to the system. Above the inelastic threshold the optical potential is complex, so that the loss of flux from the incident channel into the Q channels is represented by the absorptive imaginary potential.

The effective interaction $\mathcal{V}$ is in general *non-local*; that is, the potential acting at one point of space depends on the value of the wavefunction elsewhere. Physically, this means that the scattering system is excited into one of the omitted Q channels by an interaction at the point $\mathbf{r}'$ in configuration space may undergo a second interaction at the point $\mathbf{r}$ which causes it to reappear in the $P\Psi$ subspace. In practice, the non-local optical potential is usually approximated by a local potential, which will now have an additional energy dependence due to the non-locality of the 'underlying' optical potential. The reason for this additional energy dependence is that the non-locality in

space can be represented by a momentum dependence of the potential, since position and momentum are conjugate variables. Furthermore, the 'bare' interaction V may itself be non-local due to exchange processes, in which case the term H_{PP} will also be non-local. It follows that there are two kinds of energy dependence in the local equivalent to the effective interaction $\mathcal{V}$ — the first due to the non-locality of $\mathcal{V}$, which is known as 'spurious energy dependence' since it is not caused by any dynamic effect, and the second being due to the explicit energy dependence of the effective Hamiltonian, which is known as 'intrinsic energy dependence'. The distinction between the two forms of energy dependence is sometimes crucial in the interpretation of data, as will be seen in Subsection 5.2 of Chapter 5 of this thesis. Further details concerning the general properties of the effective Hamiltonian will be given in Chapter 4.

Writing the Schrödinger equation in the form of Eq. 2.37 may appear to be fruitless, since the complications of the scattering problem have simply been shifted from the wavefunction (which has been truncated to include only a few basis states) onto the Hamiltonian. However, the form of Eq. 2.37 allows us to apply a second simplification to the problem, by constructing a simple model U_{opt} for $\mathcal{V}$. The necessary but not sufficient criterion such a model must fulfil to be successful is that it reproduce the observed scattering data. This means that the wavefunction corresponding to the use of U_{opt} (u_0, say) must be *asymptotically* the same as the wavefunction corresponding to $\mathcal{V}$ (which is χ_0). In other words, u_0 and χ_0 must be *phase equivalent*, or give the same S-matrix elements. It is important to remember that u_0 and χ_0 may be very different in the region of interaction even though they are asymptotically equivalent at large

r. Furthermore, there could well be ambiguities between the S-matrix elements and the cross-section so that more than one U_{opt} could reproduce the same scattering data equally well within the error bars, but be very different in the region of interaction. We shall see examples of this in Chapter 3.

2.2.2 The phenomenological optical model

The fact that the strong nuclear force between nucleons has a short range means that the shape of the optical model potential should approximately follow the nucleon distribution. The simplest somewhat realistic form of the nucleon distribution is a two-parameter Fermi form,

$$f(r, R_0, a) = \frac{1}{1 + \exp\{(r - R_0)/a\}}, \tag{2.43}$$

where $R_0 = r_0 A^{1/3}$. When such a factor is used in the optical model, it is called a Woods-Saxon form factor. It constitutes the *volume term* of the optical potential, so called because it follows the volume distribution of the nucleons. This volume term is complex in general:

$$U_{\text{vol}}(\mathbf{r}) = -\{V_0 f(r, R_v, a_v) + iW_0 f(r, R_w, a_w)\}. \tag{2.44}$$

The usual phenomenological approach to the optical potential takes the parameters of the potential (as defined within a Woods-Saxon model, for example) as free parameters to be determined from experimental scattering data. This involves the

assumption that the radial dependence of the potential follows the form of the Fermi distribution of the nucleons, so that this is often referred to as *model-dependent* optical model fitting. The two-step procedure, in which an S-matrix is fitted to the data followed by iterative-perturbative S-matrix-to-potential optical model fitting, is used in the first part of this thesis. This is a *model-independent* method which makes no *a priori* assumptions regarding the radial form of the optical potential, although similar assumptions may or may not be incorporated into the $\sigma(\theta)$-to-S-matrix fitting. Other model-independent methods are also possible, such as direct spline fitting or the TELP.

As well as having a volume term, the absorptive imaginary potential may also have a *surface term.* The existence of an absorptive volume term is physically understandable in terms of the propagation of the projectile through the near-uniform nuclear matter of the interior of the target resulting in excitations out of the elastic channel, so that volume absorption is to be expected for all scattering systems. The surface absorption is due to the excitation of collective surface modes of vibration, together with possible nucleon transfer reactions or projectile breakup during peripheral collisions. The enhanced surface absorption brought about by these reactions can sometimes be represented by a volume absorption which extends to larger radii than the real volume term (i.e., $R_w > R_v$); alternatively, an actual peaking of the absorption at the surface can be represented by the surface term of the imaginary optical potential:

$$W_{\mathrm{sur}}(r) = 4W_D \frac{df(r, R_D, a_D)}{dr} = 4a_D W_D \frac{\exp\{(r - R_D)/a_D\}}{(\exp\{(r - R_D)/a_D\} + 1)^2}. \qquad (2.45)$$

This has a extremal value of $-W_D$ at $r = R_D$ (hence the factor of 4 in the definition) and a FWHM of $\Delta x_D = 3.525$.

Although both the volume and surface absorption terms are expected to exist for theoretical reasons, it is often the case that only one of these terms is actually used in a phenomenological analysis. This is because including both terms would result in a larger number of parameters in the optical model than could be determined from the scattering data. For this reason, if both terms are used, it is frequently assumed that $R_D = R_w$ and $a_D = a_w$.

Some scattering data have been found to require a more general form of optical potential volume term, especially for the real part. These data are often fitted satisfactorily by using a low power of the Woods-Saxon form factor $f(r, R_{v,w}, a_{v,w})$ instead of $f(r, R_{v,w}, a_{v,w})$ itself:

$$V(r) = -V_0[f(r, R_v, a_v)]^\nu. \tag{2.46}$$

The particular case $\nu = 2$ is commonly used, and is referred to as a Woods-Saxon-squared potential. Any such potential with $\nu \neq 1$ loses the skew symmetry about $r = R_v$ displayed when $\nu = 1$.

The Woods-Saxon volume terms were first developed for nucleon scattering, and it is not obvious that these forms would remain valid for heavy ion scattering. However, the scattering of composite particles is characterised by strong absorption, which leaves the scattering sensitive only to the region of the real potential around the strong absorption radius. In such circumstances, the simple Woods-Saxon forms may still be

used, although their validity for radii less than the strong absorption radius is dubious.

When one or both of the nuclei possess an intrinsic spin, the optical potential has a spin dependence. This means that the result of the scattering depends upon the relative orientation of the projectile spin before and after the collision.

For charged particle scattering, a Coulomb term must be included. It is usual to assume that the target nucleus can be approximated as a uniformly charged sphere, so that

$$U_{\rm Cou}(r) = \left[\frac{1}{4\pi\epsilon_0}\right] \frac{Z_p Z_t e^2}{2R_c} \left(3 - \frac{r^2}{R_c^2}\right) \tag{2.47}$$

for $r < R_c$ and

$$U_{\rm Cou}(r) = \left[\frac{1}{4\pi\epsilon_0}\right] \frac{Z_p Z_t e^2}{r} \tag{2.48}$$

for $r \geq R_c$, where R_c is the Coulomb radius:

$$R_c \sim \left[\frac{5}{3} < r^2 >_c\right]^{1/2}. \tag{2.49}$$

If both nuclei are heavy ions, then the Coulomb radius is the sum of the Coulomb radii of each nucleus:

$$R_c \sim R_{c,t} + R_{c,p}. \tag{2.50}$$

The Coulomb radius is therefore often taken to be $R_c = 1.3\{A_t^{1/3} + A_p^{1/3}\}$ fm (using the heavy ion convention).

The complete phenomenological optical model potential is then the sum of com-

plex volume, surface, spin-orbit and Coulomb terms:

$$U_{\rm opt}(\mathbf{r},\mathbf{l},\sigma) = U_{\rm vol}(\mathbf{r}) + U_{\rm sur}(\mathbf{r}) + U_{\rm s.o.}(\mathbf{r},\mathbf{l},\sigma) + U_{\rm Cou}(\mathbf{r}). \tag{2.51}$$

The total number of adjustable parameters is 12 if we take R_c to be fixed and the geometry of the real and imaginary parts to be identical. Relaxing the assumption of identical geometry gives 20 adjustable parameters. If the surface and spin-orbit terms are sometimes omitted and identical geometry is assumed, the number of parameters can be reduced to six. In a typical elastic scattering experiment, the angular distribution of the differential scattering cross-section, as well as the analysing power if the scattering is spin-dependent, are observed and the free parameters of the optical model are adjusted until a best fit to the data is obtained. By means of such optical model fitting, a large amount of information has been gathered about the phenomenological optical potential.

There are several problems with the phenomenological approach, aside from the fact that the potential cannot be directly linked with the more fundamental nucleon-nucleon interactions within the heavy ions. These problems include the fact that (i) although there exist phenomenological potentials for proton scattering over a wide range of energies and targets, this knowledge has not yet been comprehensively extended to other projectiles, especially heavy ions. It is difficult to extrapolate the potentials to energies where scattering data are sparse because of the phenomenological nature of the potentials (i.e., they are not derived from an underlying microscopic theory);

(ii) the functional forms of the radial dependence of the potentials (e.g., Woods-Saxon volume and surface terms) become increasingly inadequate as the bombarding energy is increased; and (iii) as mentioned in Section 2.1, there is an ambiguity problem in relating the potential to the cross-section. This means that the parametrization of the potential is not unique, so that very different values of the parameters can give equally good fits to the scattering data. The model-independent approach described below goes some way to ameliorating this problem by obtaining as accurate fits to the data as possible (i.e., much lower χ^2/N than is typical of Woods-Saxon fits), so that any ambiguity is inherent rather than due to the poor quality of fit. However, the ambiguity cannot be eliminated entirely, and several different ways of characterizing the potential can give equally good fits to the cross-section data. This ambiguity problem is tied up with the fact that the parameters of the Woods-Saxon model are interdependent in a complicated way, so that there are many sets of values which provide an equally good fit to the scattering data. This problem is especially acute in the case of heavy ion scattering: the strong absorption leads to the scattering being insensitive to the potential except at the region near the strong absorption radius, and many different sets of values of the parameters can give the same potential in this region.

2.2.3 The microscopic optical model

The 'microscopic' optical model is an attempt to obtain a one-body potential from the individual nucleon-nucleon forces within the scattering ions. It is more 'fundamental' than the purely phenomenological potentials so far discussed, although there still

remains a strong element of phenomenology in the use of a normalisation parameter for the real potential and a phenomenological form for the absorptive potential. This is particularly dubious, since the DPPs for such things as nucleon transfer or inelastic scattering are surface terms and therefore cannot be incorporated into the bare potential without changing its geometry rather than just its normalisation.

The most commonly used microscopic optical potential is the 'folding model' potential. The basic idea is that the local interaction between individual nucleons $v(r_{12})$ is 'folded in' with the density distributions of the nuclei $\rho_A(\mathbf{r}_1)$ and $\rho_a(\mathbf{r}_2)$ in a double integral:

$$U_F(\mathbf{r}) = \int\int \rho_A(\mathbf{r}_1)\rho_a(\mathbf{r}_2)v(r_{12})d\mathbf{r}_1 d\mathbf{r}_2. \tag{2.52}$$

where $r_{12} \doteq |\mathbf{r} + \mathbf{r}_2 - \mathbf{r}_1|$. This is usually called the double-folding model because it is a double integration over two density distributions. The single-folding model is used if the projectile a is a single nucleon, so that $\rho_a = \delta(\mathbf{r}_2)$. This reduces the integration to the single-folded form

$$U_F(\mathbf{r}) = \int \rho_A(\mathbf{r}_1)v(|\mathbf{r}_\alpha - \mathbf{r}_1|)d\mathbf{r}_1. \tag{2.53}$$

The single-folding form could also be used if we assume that the interaction between individual nucleons and the projectile a is known, and that interaction v was folded in over the density distribution of the target A. This has often been done for alpha particle scattering; however, for heavy ion scattering, the double-folding model is almost always used.

The actual calculation of the folding model integral is easiest if carried out in

momentum space. The integration then reduces to a product of three Fourier transforms (of the density distributions and the nucleon-nucleon interaction), while if the single-folding model is being used, it is a product of only two Fourier transforms.

It turns out that for most forms of ρ_i and v used in practice, the folding potential is sensitive mainly to the low momentum Fourier components of ρ_i and v. It follows that the characteristics of these component functions most relevant to physics are overall quantities such as their volume integrals and mean square radii rather than their detailed shape at larger momentum values.

If one or both of the density distributions are nonspherical, U_F will also be nonspherical. In this chapter we will restrict ourselves to spherical densities. The nucleon-nucleon interaction v is often assumed to be real rather than complex; this means that the imaginary potential must be treated phenomenologically. This is usually done by assuming a Woods-Saxon or Woods-Saxon-squared form for the absorptive potential.

It is important to note that a folded potential does not have the Woods-Saxon radial form. In fact, it often has a radial shape which is closer to that of the Woods-Saxon form raised to some power ν with $\nu \sim 2$. In cases where the scattering is sensitive to the shape of the potential over a wide radial range, it is often found that the folded shapes, or those close to it, give better fits to the data than the unmodified Woods-Saxon.

An important characteristic of the folded potential is that it has a more diffuse surface than would be obtained by simply folding the two densities alone, due to the finite range of v. This means that even in the presence of strong absorption, where the

scattering is only sensitive to the folded potential in the region of the strong absorption radius, the effect of the finite range of v on the folding integrals allows the scattering to probe the nuclear *densities* at smaller radii than it probes the *potential.* The outcome of this is that an accurate knowledge of the folded potential even in the tail of the potential at the strong absorption radius requires knowledge of the density distribution down to relatively low radial values.

Two important quantities associated with the folded potential are the volume integral per nucleon pair J_F and the root mean square radius $< r^2 >_F^{1/2}$. These quantities are defined as:

$$J_F = \frac{4\pi}{A_1 A_2} \int U_F(r) r^2 dr \tag{2.54}$$

and

$$< r^2 >_F^{1/2} = \{ \int U_F(r) r^4 dr / \int U_F(r) r^2 dr \}^{1/2}. \tag{2.55}$$

Similar quantities can be defined for the components of the folding integral. However, in my own work presented in this thesis, these quantities will not be used as extensively as they would be in Woods-Saxon or folding-model phenomenology. The reason for this is that obtaining an accurate fit to the data (so that $\chi^2/N \sim 1$) in heavy-ion cases often leads to the presence of slight oscillations in the potential at large radial values. Since the volume integral and the mean square radius contain high powers of r in their integrands, it follows that their numerical values will be influenced strongly by the presence of these oscillations in the potential tail. This makes it almost impossible to obtain systematic values of the volume integral and the mean square radius which are

consistent over a range of bombarding energy and target mass number.

A review of the application of the folding model to heavy ion scattering has been given by Satchler and Love [8].

Chapter 3

Heavy-ion elastic-scattering phenomenology by inversion

In this chapter, I present a new optical model fitting method. Section 3.1.1 introduces the rationale behind our method of optical model fitting, and Section 3.1.2 presents the method of 'two-step phenomenology' which we used to obtain local optical model potentials from elastic cross-section data. A brief comparison is made between the iterative-perturbative (IP) S-matrix-to-potential inversion method and alternative methods. Section 3.1.3 provides a detailed description of the mathematical basis of the IP inversion method, together with the assumptions and approximations underlying it. Section 3.2 presents the results of investigations of $^{16}O+^{12}C$ elastic scattering at $E_{lab} = 608$ MeV, and Section 3.3 presents results for $^{12}C+^{12}C$ from $E_{lab} = 159$ to 2400 MeV.

3.1 The method of 'two-step phenomenology' for the heavy-ion optical model

3.1.1 Introduction

The ongoing important rôle of phenomenology in nuclear physics is due to the fact that there are several distinct nuclear models employed in the study of the atomic nucleus (e.g., the optical model, the shell model, etc.), each with its own restricted domain of validity. Furthermore, the nucleus-nucleus interaction is a many-body problem which cannot be solved exactly. Since we cannot hope to formulate a fundamental theory directly from the experimental data, the several nuclear models serve as intermediate phenomenological theories between the raw data and fundamental theory.

The iterative-perturbative inversion method of doing $S(l)$ to $V(r)$ inversion can be incorporated in a procedure for getting precise fits to elastic scattering data. This allows us to reduce such data to local potentials which contain the full information content of the scattering data. The IP method readily produces potentials which uniquely reproduce $S(l)$ down to l corresponding to radii much lower than those which are of significance in the light of current experimental data, thus enabling us to produce extremely accurate phenomenological local potentials.

In many circumstances, a critical test for a theoretical analysis is to reduce it by inversion to a local potential which can then be compared with phenomenological local potentials. For these purposes phenomenology is useful if and only if either $\chi^2/N \sim 1$ is

achieved, or one can conclude from the analysis that systematic errors in the scattering data make $\chi^2/N \sim 1$ impossible with physically reasonable models (see Section 3.3). In this thesis we present a method that not only enables us to fit data which had not previously been fitted to the precision we achieve, but which motivates experiments of greater precision and angular range by showing how the information contained in such data can be extracted in the theoretically useful form of a potential.

I have used this method to investigate the heavy ion cases $^{16}O+^{12}C$ at 608 MeV, and $^{12}C+^{12}C$ from 159 to 2400 MeV, the results of which are presented in Sections 3.2 and 3.3.

3.1.2 Two-stage phenomenology

Most methods of $\sigma(\theta)$-to-$V(r)$ inversion involve direct ('one-stage') optical model searching using a parametrized form of the potential. However, this method fails in many cases (i.e., χ^2 per data point is very much greater than unity), probably because the parametrized form of the potential is too restrictive, since it imposes certain prejudices upon the potential which may or may not be valid. In this chapter, I shall be concerned instead with the application of a two stage inversion procedure which has been advocated by various authors [6, 7] and carried out with varying degrees of success [9, 10, 11]. I shall apply this procedure to the case of heavy ion elastic scattering. The two stages are as follows:

1. Find S-matrix elements which give elastic-scattering differential cross-sections which fit experimentally obtained data. This is also done in two steps:

(a) Express the S-matrix as a continuous function of l with a smooth parametrized form which gives an optimal fit to the data for that parametrization. In all the cases investigated here, we have used the McIntyre-Wang-Becker (MWB) [12] parametrization, and used a search code [13] to optimise the parameters of this continuous function $S(l)$.

(b) Add a correction, which in our case is expanded in spline functions of l, to the S-matrix in order to obtain an optimal fit to the experimental data. We refer to these as 'spline-improved S-matrices' (SIM) or 'parameter-improved phase shifts' (PIPS).

2. The second stage involves inverting the spline-improved S-matrices to obtain the corresponding local potentials $V(r)$.

This two stage procedure has been made feasible by the emergence of practical methods [2, 14, 15, 16, 17] of $S(l)$-to-$V(r)$ inversion.

Of the above references, the closest to this work is that of Allen *et al.* [18] who invert from $S(l)$ of MWB form with parameters previously fitted to the data by Mermaz *et al.* [19, 20]. Our own method differs in two main respects:

1. Our inversion method is not based upon the semi-classical WKB approximation. This means that we can do accurate inversions even at lower energies, where the WKB approximation is no longer valid. Furthermore, we are not limited to smooth functions $S(l)$.

2. We use a fitting procedure [13] that can in principle reproduce elastic scatter-

ing data very precisely. Indeed, using spline-improved S-matrices, we can often obtain values of χ^2 per data point of less than unity.

These two differences are crucial. It is our opinion that *a priori* assumptions concerning the smoothness of, or the form of, the potential or S-matrix should not be imposed when it is likely that an underlying l-dependence of the internuclear potential due to channel coupling etc. exists, and would be represented in an l-independent potential by some degree of non-smoothness.

Stage 1: Cross-section to S-matrix fitting. The MWB parameterization of the S-matrix elements $S(l) = |S(l)| \exp 2i\delta_l$ is given in terms of the reflection coefficient and the real part of the nuclear phase shift by the following two expressions:

$$|S^M(l)| = \frac{1}{1 + \exp((l_g - l)/\Delta)} \tag{3.1}$$

$$\delta^M(l) = \frac{\mu}{1 + \exp((l - l'_g)/\Delta')}. \tag{3.2}$$

For low partial waves ($l \ll l_g$), corresponding to small impact parameters, the modulus of the S-matrix vanishes, representing strong absorption. For large l, corresponding to scattering with impact parameters outside the nuclear surface, $|S_l| = 1$, which represents total reflection of these partial waves. There is a smooth transition between these two extreme values at the nuclear surface (where $l \sim l_g$). On the other hand, the nuclear phase shift has an almost constant value for low l-values but becomes negligible for large l-values, with a smooth transition over the region where

$l \sim l'_g$. Fig. 3.1 shows a typical MWB S-matrix.

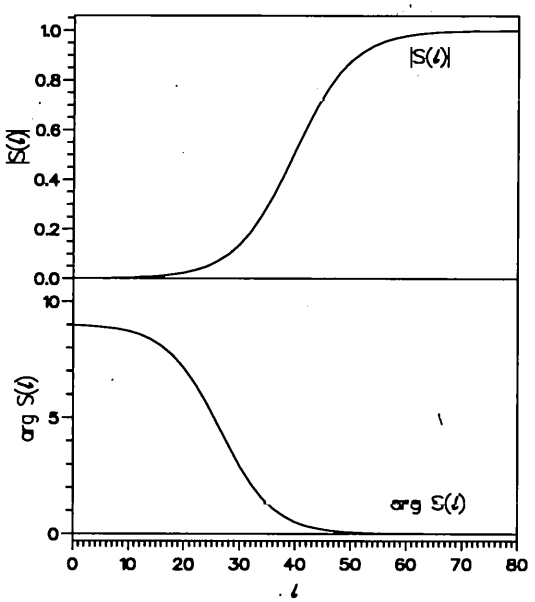

Figure 3.1: The modulus and argument of the MWB parameterized form of $S(l)$ for 1016 MeV ^{12}C+^{12}C. Note that arg $S(l) = 2\delta(l)$.

If the grazing angular momenta for the modulus and phase, l_g and l'_g, and their related widths, Δ and Δ', are set equal to each other, there are just three parameters. However, Mermaz [19] found that the five-parameter fit is significantly better in all cases for ^{12}C+^{12}C scattering at 360 and 1016 MeV, and for ^{16}O+^{12}C at 1503 MeV, and we will only use the five parameter form of the MWB S-matrix elements.

As a bonus, using the MWB formula for the nuclear phase shift enables us to write the deflection function in a convenient analytic form:

$$\Theta_l = 2\arctan\frac{\eta}{l} - \frac{2\mu}{\Delta'}\frac{\exp((l-l'_g)/\Delta')}{(1+\exp((l-l'_g)/\Delta'))^2}. \tag{3.3}$$

The five parameters of the MWB S-matrix are optimised using the interactive search code CSFIT [13], and the S-matrices obtained are inverted to find the corresponding internuclear potentials. Once this has been done, we take the optimised MWB S-matrices and add a correction, which is expanded in spline functions of l, to improve the fit to the data. The final S-matrix can therefore be written as the sum of two terms:

$$S(l) = S^{\mathrm{MWB}}(l) + S^{\mathrm{c}}(l) \tag{3.4}$$

where $S^{\mathrm{c}}(l)$ is a spline correction chosen so that the unitarity limit is preserved. Searching is performed on $|S_l|$ and on $\arg S_l$ separately, so we can constrain $|S_l|$ to be less than or equal to unity at the spline knots. This yields the 'spline improved MWB' (SIM) S-matrix. We then invert the SIM S-matrix to obtain the potential $V(r)$.

We obtain two potentials for each set of scattering data corresponding to the MWB S-matrix, and the SIM S-matrix. The direct comparison of these two potentials can give us useful information concerning those features of the final SIM potential which are needed to fit the experimental data at large angles, where the MWB S-matrix almost invariably fails to fit the data.

Stage 2: S-matrix to potential inversion. There are several different categories of S-matrix to potential inversion. Three of these are:

- Fixed energy inversion. We take given S-matrix elements for 'all' values of l (from 0 to ∞) for some particular energy, and invert to find $V(r)$ for 'all' r. In practice, of course, we take a specified restricted range of l and a corresponding restricted

range of r. This is particularly appropriate to the case of nuclear scattering, since the strong nuclear force has only a finite range.

- Fixed angular momentum inversion. Pioneered by Gel'fand and Levitan [2], this method takes given S-matrix elements for 'all' energies for some particular partial wave, and inverts to obtain $V(r)$ for 'all' r. Obviously we cannot know the S-matrix elements for all energies, since we do not wish to go above the pion production threshold, and in practice a limited energy range is involved.

- Mixed case inversion, as its name implies, combines the previous two cases. S-matrix elements over a selected range of partial waves and for selected values of energy are inverted to find $V(r)$ for a restricted range of r.

A good general reference to quantum inverse scattering problems is the book by K. Chadan and P.C. Sabatier [2].

There are many methods of fixed energy inversion; some of these include:

1. Newton Sabatier [14]

   (Newton, Münchow and Scheid, etc.)

2. WKB methods [18]

   (Fiedeldey, da Silveira and LeClerq-Willain, etc.)

3. Bargmann methods [15]

   (Lipperheide, Fiedeldey, Leeb, etc.)

4. Iterative-perturbative (IP) [16, 17]

   (Mackintosh, Kobos, Ioannides, Cooper)

5. Algebraic methods

   (Kermode, Malik)

We shall apply the iterative-perturbative (IP) method. At the present time, only this method has been used for mixed case inversion [11, 21], and this constitutes one of its main advantages over other methods, along with its applicability to projectiles with spin, etc. For the cases to be discussed here only fixed energy inversion for spin zero nuclei is used.

The two stage inversion procedure has advantages over the more usual direct optical model searching, one of which is the possibility it offers of gaining insight into the ambiguities involved in establishing potentials from scattering data. These ambiguities are not fully explicit in the single stage procedure, since the high degree of non-linearity in that case is actually a compounding of the non-linearities of the $\sigma(\theta)$-to-$S(l)$ and $S(l)$-to-$V(r)$ inversions.

Furthermore, the two stage inversion procedure, especially when used in conjunction with the iterative-perturbative inversion method (see Section 3.1.3), has computational advantages for heavy ions. Indeed, it may be the simplest way of finding almost perfect fits to elastic scattering data for heavy ions at high energies where the number of partial waves, the number of mesh points and the number of potential parameters used in the model-independent fitting are all very high. This is because S-matrix searching

is much faster than multiparameter potential searching, particularly for heavy ions. The initial $\sigma(\theta)$-to-$S(l)$ inversion using CSFIT [13] was found to be generally straightforward, being characterized by a considerable degree of linearity. Much the same could be said for the iterative-perturbative $S(l)$-to-$V(r)$ inversion using the program IMAGO [23], which was also carried out interactively with the cross-section fits and S-matrices being monitored graphically on-line.

3.1.3 The iterative-perturbative inversion method

The iterative-perturbative (IP) method for fixed energy inversion [16] is based upon the observation [24, 6] that the response of the S-matrix elements to small perturbations in the potential is rather linear.

The inverse potential should be a close approximation to the 'target potential' V^{tar} which obeys the radial Schrödinger equation for a selected partial wave,

$$\left[\frac{\hbar^2}{2\mu}\left(-\frac{\mathrm{d}^2}{\mathrm{d}r^2}+\frac{l(l+1)}{r^2}\right)+V_{\mathrm{Cou}}(r)+V^{\mathrm{tar}}(r)-E\right]u_l(r)=0. \tag{3.5}$$

Since, asymptotically, $u_l \rightarrow I_l - S_l O_l$, we obtain a radial wave function $u_l(r)$, which matches onto I_l and O_l, the incoming and outgoing Coulomb wave functions for a given l and E, at some matching radius r_m, to give

$$u_l(r_m) = I_l(r_m) - S_l^{\mathrm{tar}} O_l(r_m). \tag{3.6}$$

The potential $V_{\rm Cou}(r)$ is the Coulomb potential, $V^{\rm tar}(r)$ is the complex nuclear potential corresponding to $\mathbf{S}^{\rm tar}$, and $u_l(r)$ is the l'th partial wave of the scattered wavefunction.

In practice the inverse potential $V^{\rm inv}(r)$ will not be identical to $V^{\rm tar}(r)$, and it is therefore desirable to define a measure for how closely the target S-matrix is reproduced by $V^{\rm inv}$. This 'phase shift distance', σ^2, is defined as

$$\sigma^2 = \sum_{l=0}^{N_l} |S_l^{\rm tar} - S_l^{\rm curr}|^2, \tag{3.7}$$

where N_l is the number of active partial waves.

To minimise σ^2, we must add perturbations to $V^{\rm inv}(r)$. We separate the new nuclear potential $V^{\rm new}(r)$ into a linear sum,

$$V^{\rm new}(r) = V^{\rm inv}(r) + \sum_{i=1}^{N_b} \lambda_i v_i(r), \tag{3.8}$$

where λ_i are complex constants and v_i $(i = 1, 2, \ldots, N_b)$ are a set of N_b small perturbations which can be thought of as a set of 'basis functions' in terms of which the additive correction to $V^{\rm inv}$ has been expanded. The perturbations v_i are small compared to $V^{\rm inv}$ (in fact, $v_i/V^{\rm inv} \ll 0.1$ in most cases). Each potential component, real imaginary, central, spin-orbit, etc., can be assigned a separate expansion basis.

If the potential perturbation $\lambda_i v_i(r)$ is small, the Born approximation can be used to obtain an approximate expression for the corresponding change in the S-matrix

element, $\delta S_l = S_l^{\text{new}} - S_l^{\text{inv}}$, caused by the potential perturbation:

$$\delta S_l \simeq \Sigma_i \left(\frac{i\lambda_i \mu}{\hbar^2 k}\right) \int_0^\infty |u_l(r)|^2 v_i(r) \mathrm{d}r, \tag{3.9}$$

where u_l is the radial wavefunction obtained from the Schrödinger equation using $V^{\text{inv}}(r)$. In practice, the integral is integrated numerically up to the matching radius r_{m}.

An expansion matrix $\mathbf{\Delta}$ can be defined from Eq. 3.9, such that $\Delta_{li} = \partial S_l / \partial \lambda_i$. Applying this to Eq. 3.8 with the 'linearity assumption' that the amplitudes λ_i are small gives us an approximate correction to the S-matrix:

$$\mathbf{S}^{\text{new}} \approx \mathbf{S}^{\text{curr}} + \mathbf{\Delta\lambda}. \tag{3.10}$$

Putting this approximation into the definition of σ^2 provides a least squares solution to minimise the phase shift distance, thus obtaining a set of linear equations to determine $\boldsymbol{\lambda}$ whose components are the expansion coefficients of the potential perturbation, λ_i:

$$\mathbf{\Delta}^\dagger \mathbf{\Delta\lambda} = \mathbf{\Delta}^\dagger \boldsymbol{\delta}. \tag{3.11}$$

In principle, direct matrix inversion could be used to find $\boldsymbol{\lambda}$:

$$\boldsymbol{\lambda} = (\mathbf{\Delta}^\dagger \mathbf{\Delta})^{-1} \mathbf{\Delta}^\dagger \boldsymbol{\delta}. \tag{3.12}$$

However, direct matrix inversion often fails because of inaccuracy in the linearity approximation, so in IMAGO the technique of singular value decomposition (SVD) is used [25]. This gives

$$\mathbf{\Delta} = \mathbf{U}\mathbf{D}\mathbf{V}^{\dagger}, \tag{3.13}$$

where $\mathbf{V}$ is square, $\mathbf{V}^{\dagger}\mathbf{V} = \mathbf{1}$ and $\mathbf{U}^{\dagger}\mathbf{U} = \mathbf{1}$, although $\mathbf{U}$ will not be square since this is a system of overdetermined equations.

The matrix $\mathbf{D}$ is diagonal with the non-zero components being the set of singular values d_j. Directly evaluating $\boldsymbol{\lambda}$ gives

$$\boldsymbol{\lambda} = \mathbf{V}\mathbf{D}^{-1}\mathbf{U}^{\dagger}\boldsymbol{\delta}, \tag{3.14}$$

where $\mathbf{D}^{-1}$ is diagonal in $1/d_j$. The value of the SVD method is that the smallest values of d_j, which are the least accurately determined and whose inclusion can greatly distort the solution $\boldsymbol{\lambda}$, can be eliminated, thereby guaranteeing the convergence of σ^2. The SVD formalism ensures that for each included basis function v_j, the final solution corresponds to a least squares sum over the amplitude of included basis functions.

The solution for λ defines a new current potential which will have a smaller phase shift distance σ^2. Since the linearity assumption implicit in the IP method is only approximate, the process must be repeated starting from the new potential. Thus, there will be a set of iterations (typically on the order of 5–10 for heavy ions) which will converge on a particular (small) value of σ^2.

Successive iterations converge to a potential which corresponds to either a global

or a local minimum of σ^2. The convergence is apparent when σ^2 is constant over a few iterations, and occurs when the inversion amplitudes λ_i are all zero within the numerical accuracy to which we are working. The magnitude of σ^2 after convergence reflects the extent to which an inverted potential which comes closest to reproducing $\mathbf{S}^{\mathbf{tar}}$ is outside the space spanned by the basis functions $v_i(r)$. For this reason the magnitude of σ^2 after convergence is related to the range of uncertainty in the inverted potential. If the inversion converges to a fairly large value of σ^2, then starting with different choices of SRP or $v_i(r)$ will yield potentials with the same quality of fit to $\mathbf{S}^{\mathbf{tar}}$, but which differ over some radial regions. If the converged value of σ^2 is made smaller, for example by increasing the number of basis functions N_b, the range of different inverted potentials which give the same fit to $\mathbf{S}^{\mathbf{tar}}$ decreases. A key part of the procedure is to use the fact that the SRP, N_b and v_i are not unique to check that different choices which converge to comparable values of σ^2 give the same inverted potential. For all the cases investigated in this chapter, such potentials were independent of the SRP, and the number and type of the basis functions, at radii beyond 1–2 fermi.

The above discussion implies that there is an irreducible element of choice involved in the implementation of the iterative-perturbative method; namely, the selection of the starting reference potential V^0 and the set of N_b basis functions. Clearly, the algorithm will perform faster and more efficiently if the SRP is close to the 'true' potential, but we found that good convergence could be achieved for all the cases investigated in this chapter even with an SRP which was identically zero for all r. The set of basis functions v_i can of course be any linearly independent set of functions which spans the

radial range strongly influencing the S-matrix elements $\mathbf{S}^{\mathbf{tar}}$. In our implementation of the method, we have the choice of three different kinds of basis function—zeroth order bessel functions, spline functions or gaussians.

The iterative-perturbative method has many advantages over alternative inversion methods. One of these is a consequence of the fact that it is an iterative method. The results of a converged calculation have the inherent reliability of a converging iterative method insofar as the potential which is found automatically reproduces $\mathbf{S}^{\mathbf{tar}}$ at a level of precision defined by the converged value of σ^2. The result may be checked by using alternative sets of basis functions and starting potentials. Furthermore, the range of potential forms which can be determined are not confined to smooth shapes and this range is limited only by the requirement that the potential be within the space spanned by the basis functions. The dimension of this basis is limited by the requirement that the system be overdetermined (the number of active partial waves must exceed the number of basis functions). Indeed, it is a particular virtue of the iterative-perturbative over other inversion methods that it lays bare the range of potentials that fit $\mathbf{S}^{\mathbf{tar}}$ with a given degree of imprecision. The reliability of the method is not compromised by the need for a reasonable starting potential, as I have verified for the cases dealt with in this chapter—very often a *zero* SRP gave almost perfect results.

One of the limitations of the method (and all other methods) for heavy ions is that the low value of $|S_l^{\mathbf{tar}}|$ for small l inhibits the determination of $V^{\mathbf{tar}}(r)$ in the nuclear interior. This problem is especially acute when $\mathbf{S}^{\mathbf{tar}}$ is an MWB S-matrix. However,

this problem is not as severe as might be thought, as the internuclear potential between two heavy ions is not a very meaningful concept when the charge density of each nucleus at the point of overlap is greater than about 80% of its value at the nuclear centre. For ^{12}C on ^{12}C, this means internuclear separations of about 2–3 fermi. For deeper interpenetration than this, the nuclei would tend to lose their separate identity, and the strong absorption at such radii in any case means that the cross-section is insensitive to details of the 'potential' in that radial region.

Fixed energy inversion procedures can be applied to nuclear physics in two main ways:

1. To invert theoretically determined S-matrix elements; for example, those obtained from a coupled-channel calculation. The potential so obtained would then be a local potential representing in a convenient form the effects of channel coupling. In the same way, we can obtain local potentials which are equivalent to any given non-local potential, or to any given l-dependent potential. It is a fundamental theorem of inverse scattering theory that such a local equivalent potential always exists for any physically possible S-matrix [2].

2. To invert S-matrix elements which have been obtained by fitting experimental scattering data. This approach to local potential phenomenology is a means of escaping current theoretical prejudices and leads to a greater exploitation of the information content of the best experimental data with a fast inversion method.

Hitherto, most work has concentrated on the first category of application. This is

mainly due to the ambiguity problems associated with phase shift searches to fit experimentally obtained data. In this chapter, we shall be concerned with the second type of application.

3.2 $^{16}O+^{12}C$ at E_{lab}=608 MeV

The experimental data for this case, which is of considerable physical interest, was obtained by Brandan *et al.* [26].

The procedure which was followed (see Section 3.1.2) was to:

(i) use the program CSFIT to optimise the five parameters of the MWB S-matrix to obtain an optimal fit to the cross-section,

(ii) use the program IMAGO to obtain an inverted optical potential corresponding to the optimised MWB S-matrix,

(iii) use CSFIT again to add a correction to the MWB S-matrix, expanded in spline functions of l, to obtain a better fit to the cross-section (we refer to the S-matrix so obtained as a SIM S-matrix),

(iv) use IMAGO again to obtain an inverted potential corresponding to the SIM S-matrix.

Fig. 3.2 compares $|S(l)|$ and $\arg S(l)$ for the inverted potentials corresponding to the MWB and SIM fits to the cross-section, and a Woods-Saxon optical fit by Brandan [27]. The inversion produces S-matrices which are visually indistinguishable

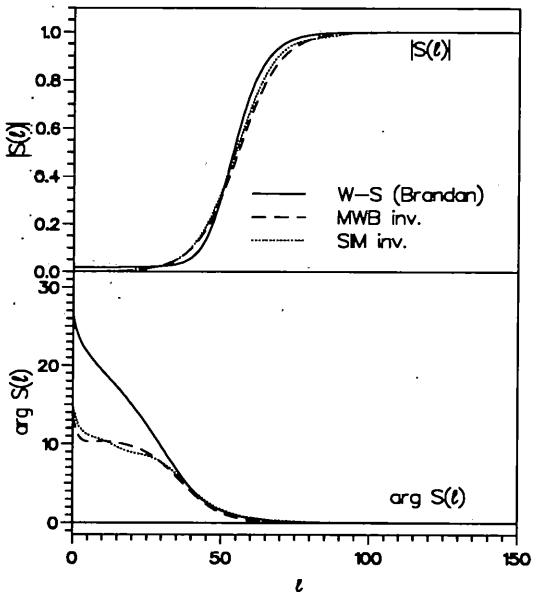

Figure 3.2: S-matrices derived from the inverted potentials for 608 MeV $^{16}O+^{12}C$ scattering, compared with that derived from a Woods-Saxon optical fit by Brandan [27].

from the 'target' S-matrices obtained using CSFIT. The SIM S-matrix has a longer tail on $\arg S(l)$ and a slight bend in $|S(l)|$ at about $l \sim 70$ at which a generally sharper slope towards unity with increasing l than the MWB $|S(l)|$ crosses the MWB curve to give a more gradual approach to unity for $l \geq 75$. This feature is visually quite small, the SIM S-matrix generally being close to the MWB, but since these slight differences occur over an l-range which semi-classically corresponds to a region close to the strong absorption radius, these differences are not necessarily negligible in their effects on the inverse potentials. The behaviour of the S-matrices for $l < 20$ is not well established, due to the strong absorption of the low partial waves, and the fits shown must be considered artefacts of the MWB starting form. The long tail on $\arg S(l)$ is a most interesting physical feature of the SIM $S(l)$, and lies beyond the scope of the MWB

form. It is, however, essential for a good fit to the data, the quality of fit being greatly improved by the objective measure of χ^2/N as well as by more subjective standards of appearance. The tail seems particularly essential for a correct representation of the cross-section at the Fraunhofer diffraction minima at 7° and 11° (see Fig. 3.3, showing fits to the cross-section data using potentials inverted from the $S(l)$). The quality of fit for the $\frac{d\sigma_{el}}{d\Omega}(\theta)$-to-$S(l)$ inversion stage is shown in the first column of Table 3.1. For the MWB $S(l)$ I obtained $\chi^2/N = 3.023$, while for SIM I obtained $\chi^2/N = 0.897$, which is substantially better. The quality of fit of the inverted potentials to the experimental data is presented in the second column of Table 3.1.

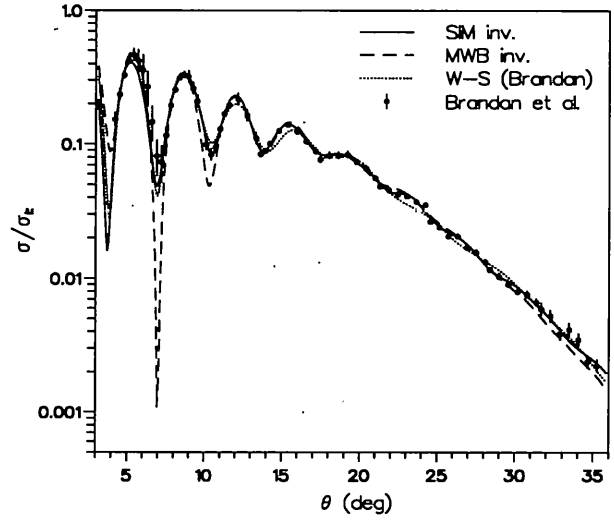

Figure 3.3: Differential cross-sections derived from the inverted potentials for 608 MeV $^{16}O+^{12}C$ scattering.

The IP inversion method gave local potentials representing the phase shifts shown in Fig. 3.2 *uniquely* for $l > 20$; for lower values of l, $|S(l)|$ is very small and these phase

	S_l	$S_l \rightarrow V(r) \rightarrow S_l$
W-S	—	4.72
MWB	3.023	3.014
SIM	0.897	0.951

Table 3.1: χ^2/N for the Woods-Saxon potential of Brandan, the MWB S-matrix, and the SIM S-matrix. The first column gives χ^2/N for the S-matrix elements obtained in the first stage of inversion, the second for the S-matrix elements derived from the potentials obtained in the second stage of inversion.

shifts are not physically significant in determining the cross-section. Whether I started the IP inversion iterations from a Woods-Saxon or even from a *zero* potential made no difference to the final potential beyond $r = 1$ fm. The quality of the inversion is reflected in the fact that the final χ^2/N for the potential obtained from the SIM S-matrix was 0.951, close to the value quoted above for the SIM $S(l)$ itself. For the potential obtained by inverting the MWB $S(l)$, we have $\chi^2/N = 3.014$ compared with 3.023 for the MWB $S(l)$ itself. From these figures, it can readily be seen that the $S(l)$-to-$V(r)$ inversion is almost perfect.

One of the key qualitative features characterizing a heavy-ion potential is the ratio of the imaginary to real potential in the nuclear surface, which is here denoted by W/V. In this respect, the difference between the MWB and SIM potentials is very significant—W/V in the surface is entirely different for the two cases. At the strong absorption radius (SAR, defined using $|S(l)|^2 = 0.5$), I found that $W/V = 0.70$ for

the SIM potential (the SAR being at 6.73 fm), whereas $W/V = 1.09$ for the MWB potential (the SAR is at 6.82 fm). The disparity rapidly increases with radius (see Table 3.2). Thus the SIM potential may be classified as surface transparent, but the potential derived from the MWB $S(l)$ is not. As a result, there is a large difference between the MWB and SIM differential cross-sections regarding the shape of the cross-section in the Fraunhofer interference region. This is responsible for a large measure of improvement of the fit. I examined the nearside/farside decomposition following the formalism of Fuller [28] and found that, in going from MWB to SIM, the farside component is enhanced in this angular region, and the nearside component depressed. This enhancement of the farside component would seem to tally with the greater surface transparency of the SIM potential compared to the MWB potential.

I applied a notch test to determine the minimum radius for which the given data determines the potential; it is about 3 fm. More specifically, a gaussian notch of width 0.3 fm and of depth equal to 5% of the local real potential increases χ^2/N by a factor of two when centred at 3.6 fm.

The χ^2/N values quoted in Table 3.1 show that the fits for the SIM-derived potential are much better than for the potential derived from the MWB S-matrix. To establish the reasonableness of my results I compared them with a standard optical model potential, using the published Woods-Saxon parameters of Brandan [27]. In Fig. 3.3, I compare the SIM fit (solid line) with the Woods-Saxon fit of Brandan (dotted line) which was found to give $\chi^2/N = 4.72$; the Fraunhofer interference region between 10° and 20° is fitted much better by the SIM potential, with oscillations of

greater magnitude. There are weak oscillations in the shape between 20° and 30° which are missed by the conventional potential. The SIM does slightly worse only at the maximum near 6 degrees. Fig. 3.3 also compares the SIM and MWB (dashed line) fits; the SIM potential gives a very much better fit than the MWB potential to $\sigma(\theta)$ at the Fraunhofer region between 5° and 15°; as mentioned above, the origin of this is in the relative strengths of nearside and farside amplitudes.

I have not presented figures comparing the differential cross-sections calculated directly from MWB of SIM $S(l)$ with cross-sections calculated from the respective inverted potentials; in both cases they are virtually indistinguishable over the entire angular range where there is experimental data.

Improved optical model fits, reaching χ^2/N close to unity have been obtained by using generalised Woods-Saxon shapes and spline real potentials [29], but the present comparison serves well to demonstrate one of the main conclusions: that *un*corrected MWB $S(l)$ can lead to erroneous qualitative results. Fig. 3.4 compares the SIM potential with Brandan's Woods-Saxon and with the 'MWB' potential. For $r \geq 5$ fm the agreement of the real part of the SIM potential with that of Brandan is remarkable, but not complete: I find a long tail in the real part of the SIM potential that is an evident concomitant of the SIM $\arg S(l)$; the real part of the MWB potential, also shown in Fig. 3.4, entirely lacks such a long tail.

The fundamental disagreement between MWB and SIM potentials is more evident in Table 3.2, which also shows that the SIM potential and Brandan's Woods-Saxon potential have the same general W/V behaviour. The disagreement between the SIM

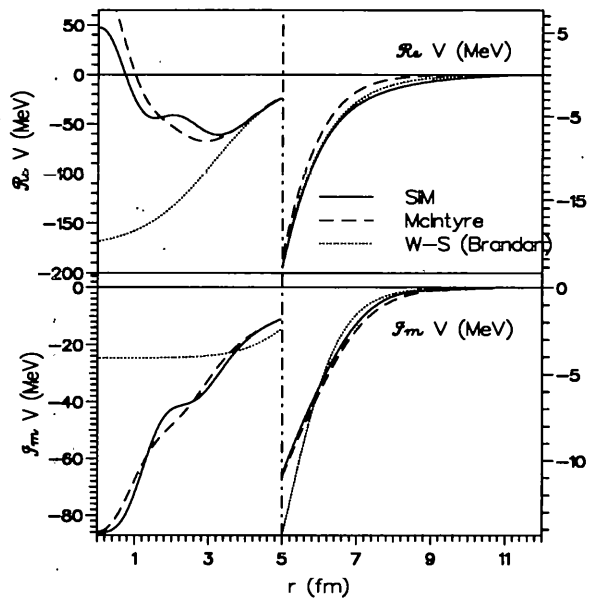

Figure 3.4: Potentials obtained by inversion from MWB and SIM S-matrices compared with Brandan's optical model for 608 MeV $^{16}O+^{12}C$ scattering.

and MWB results, the agreement between SIM and Woods-Saxon and the much better fit to $\frac{d\sigma_{el}}{d\Omega}(\theta)$ given by the SIM potential all suggest that the potentials derived from the MWB $S(l)$ can lead to incorrect conclusions concerning qualitative features such as surface transparency. This is an important point, and it underlines the essential difference between this work and that of Allen *et al.* [18].

The inverted potentials shown in Fig. 3.4 should not be taken seriously for radii below 3 fm, the repulsion at $r = 0$ being a clear artefact of the underlying MWB form which the data could not discriminate against. However, I found evidence to suggest that data over a wider angular range might actually lead to information concerning the behaviour of the potential around 3 fm or below. I mentioned above the notch test relating to the effect upon χ^2/N of small localised perturbations in the potential; it

Radius (fm)	5.5	6.0	6.5	7.0	7.5	8.0	8.5
W-S	0.68	0.66	0.58	0.48	0.40	0.31	0.24
MWB	0.65	0.86	0.96	1.30	1.52	1.69	1.57
SIM	0.57	0.67	0.64	0.66	0.52	0.36	0.22

Table 3.2: The ratio W/V at various radii for the Woods-Saxon potential of Brandan, the potential corresponding to the MWB parametrization of the S-matrix, and the SIM potential.

turns out that the quantity σ^2 that we use to study the quality of the inversion (see Section 3.1.3) is sensitive to perturbations in the potential down to about $r = 2$ fm.

3.3 ^{12}C+^{12}C from $E_{\rm lab}$=159 to 2400 MeV

Please note: These data have also been analysed in a previously published paper co-authored by myself [22] (N.B.: I have since changed my surname from McEwan to Russell). The inversions for the paper were done by me, together with the main bulk of the analysis and the first draft. S.G. Cooper provided help with the programs used in the analysis (CSFIT and IMAGO) and R.S. Mackintosh helped with the interpretation of some of the results. The present analysis differs from that of the published paper in some important respects. Due to limitations of space, the analysis in the published paper was brief and contained only a minimal number of figures, while the analysis in this thesis presents new inversions and a fuller range of figures; a visual comparison of the inverted potentials and their associated S-matrices and deflection functions is

extremely important for this kind of inversion analysis. The inversions presented here are not the same as those of the published paper. I felt that it would be useful to have a check on the consistency of the inversion process if all the inversions were repeated and the results analysed afresh. The inversions agree with those obtained previously. The lowest energy case presented in the published paper, 139.5 MeV, has been omitted here due to the relatively poor quality of the data which made inversion difficult and the results ambiguous.

3.3.1 Introduction

The case of $^{12}C+^{12}C$ elastic scattering is of great interest, both from a kinematic and a dynamic point of view. There have been many attempts to determine whether there are rainbows at certain energies, and many attempts to calculate the internuclear potential. Here, I establish by inversion local potentials reproducing the elastic scattering of ^{12}C from ^{12}C at laboratory energies of 158.8, 161.1, 288.6, 360, 1016, 1449 and 2400 MeV. I have not attempted to fit the scattering data at energies where the data were of insufficient angular range for unambiguous inversion to be possible, and for certain energies the data were unavailable. The references for the experimental data are given in Table 3.3.

Energy (MeV)	158.8	161.1	288.6	360	1016	1449	2400
Reference	[30]	[31]	[31]	[32]	[32]	[33]	[33]

Table 3.3: References for the experimental data for $^{12}C+^{12}C$ at various energies.

The Coulomb potential used is that of a point charge in the presence of a uniformly charged sphere, with a Coulomb radius $R_C = 0.95(A_p^{1/3} + A_t^{1/3})$ fm. This value for the reduced radius gives a reasonable approximation to the potential between two uniformly charged spheres [34], and it is the same as the Coulomb potential employed by Brandan [27] and Brandan and Satchler [35] in their analyses of these cases. My calculations were fully symmetrized, and the highest energies were treated relativistically. Although the scattering in the centre-of-mass system is always described by a non-relativistic Schrödinger equation, it can make a significant difference [36] to the results of calculations done at the higher energies whether the transformation of the data from the laboratory to the centre-of-mass frame is done relativistically or not. The 1016, 1449 and 2400 MeV data were therefore reduced relativistically, which corresponded to using the following parameters in the non-relativistic Schrödinger equation:

1016 MeV case: E_{lab}=994 MeV, ^{12}C mass=12.270 u.

1449 MeV case: E_{lab}=1404 MeV, ^{12}C mass=12.382 u.

2400 MeV case: E_{lab}=2278 MeV, ^{12}C mass=12.644 u.

The four highest energy cases have been studied by Allen *et al.* [18] using MWB S-matrices with parameters determined by Mermaz *et al.* [20] and using a WKB inversion procedure which failed at 360 MeV. In this investigation, I show that the fully quantal IP inversion procedure gives unique potentials at all physically significant radii, giving potentials that precisely reproduce S_l for all relevant l not only for 360 MeV, but down to 158.8 MeV as well.

My analysis differs from some previous S-matrix searches, and also from some

conventional optical model studies of the same data in one respect—the weighting of the experimental errors. It is significant in that it leads to somewhat different sets of S_l even within the restricted scope of the parametrized forms. In references [19, 20] etc. the experimental weights were abandoned in favour of equal weights (10 percent errors, typically) at each angle, the intention being to increase the influence of the backward angles. This introduction of subjective elements into the analysis is an expression of the failure of the parametrization being used to fit the data. A necessary, but not sufficient, criterion for a correct model is a low value of χ^2/N, *based on experimental weights*, assuming these are correctly estimated and that systematic errors are not greater than quoted statistical errors. In particular, it is possible that there is significant uncertainty in the overall normalisation of the cross-section, and this could be very important; in fact such problems seem to be at the root of inconsistency between results at 360 MeV and other energies, as discussed below.

For all the results to be presented in this section, the inverted local potential has the following two characteristics: (i) uncertainties in the potential due to the S_l-to-$V(r)$ inversion are always less than uncertainties in the $\frac{d\sigma_{el}}{d\Omega}(\theta)$ to S_l inversion, and (ii) it is a unique representation of the S-matrix over a radial range significantly greater than the sensitive range over which changes to the potential have an appreciable effect at angles where $\frac{d\sigma_{el}}{d\Omega}(\theta)$ is measurable. Table 3.4 shows the parameters used in the inversion procedure, including the maximum l value of the S-matrices and the radial step and maximum radius of the potentials. In Subsection 3.3.2, I give more specific details of the problems involved in determining S_l from the cross-sections, and in Subsection 3.3.3

Energy (MeV)	max. l (MWB, PIPS)	radial step (fm)	max. radius (fm)
158.8	80, 56	0.035	12.0
161.1	80, 58	0.035	12.0
288.6	120, 80	0.035	12.0
360	100, 80	0.025	11.0
1016	130, 130	0.020	12.0
1449	200, 200	0.020	14.0
2400	180, 180	0.015	10.5

Table 3.4: Parameters used in the inversion procedure.

the degree of uniqueness of the S_l-to-$V(r)$ inversion.

3.3.2 S-matrices fitted to $^{12}C+^{12}C$ elastic scattering data

The first step was to obtain MWB S-matrices by fitting the elastic differential cross-section data for the various bombarding energies. Starting from the MWB parameters of Mermaz *et al.* [19, 20], the code CSFIT was used to further optimize the five parameters. This was especially important for the 1449 MeV case, where (as Allen *et al.* [18] point out) Mermaz *et al.*'s parameter values do not give an optimal fit to the scattering cross-section. In fact, I was able to reduce Mermaz *et al.*'s χ^2/N value of 9.68 down to 4.47 (see Table 3.5). Once having obtained these optimal smooth S-matrix elements based on the strong absorption model, they were the starting point in a search with

E_{lab} (MeV)	158.8	161.1	288.6	360	1016	1449	2400
S_l	21.82	8.19	3.66	4.03	3.57	4.47	17.44
$S_l \rightarrow V(r) \rightarrow S_l'$	24.19	8.22	3.65	4.03	3.57	4.59	17.63

Table 3.5: χ^2/N for the MWB S-matrices. The second row gives χ^2/N for the S_l obtained in the first stage of inversion, the third for the S_l' derived from the potentials obtained in the second stage of inversion.

CSFIT to improve the fit to the data by adding corrections to the MWB form. The corrected S-matrices were called 'parameter-improved phase shifts' (PIPS), and are essentially the same as the 'SIM' S-matrices used in the analysis of $O^{16}+C^{12}$ at 608 MeV in this thesis. The only difference is that splines only were used as the basis functions for the 'spline-improved' (SIM) S-matrices while other types of basis function, such as bessels, were available when fitting the 'parameter-improved phase shifts' (PIPS) to the cross-section data. The PIPS S-matrices are displayed alongside their MWB starting points and (in all cases except 161.1 MeV) a standard optical model S-matrix for each energy in Figs. 3.5 through 3.25, together with the cross-section fits and the semiclassical deflection functions. The quality of fit at each energy is measured by the value of χ^2 per data point, as given in Table 3.6. These 'target' S-matrices were used as input for the IP inversion method to obtain local potentials, from which 'inverse' S-matrix elements could be calculated. The consistency of the inversion could be checked by comparing the 'target' S_l obtained by directly fitting cross-section data with the 'inverse' S_l calculated from the potentials. In all cases, it was found that the

$E_{\rm lab}$ (MeV)	158.8	161.1	288.6	360	1016	1449	2400
S_l	3.21	5.13	1.16	2.10	1.57	1.49	10.54
$S_l \rightarrow V(r) \rightarrow S'_l$	4.62	5.35	1.49	2.19	1.57	1.47	10.53

Table 3.6: χ^2/N for the PIPS S-matrices.

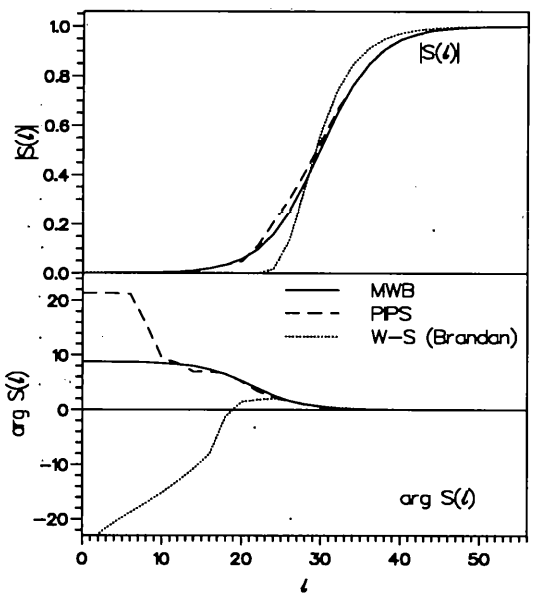

Figure 3.5: Fitted S-matrices for 158.8 MeV ^{12}C+^{12}C scattering.

'inverse' S_l were indistinguishable from the 'target' S_l on the scale of these graphs for all relevant partial waves.

158.8 MeV: It can be seen from Fig. 3.5 that both the MWB and PIPS S-matrix fits for the 158.8 MeV case are very different from that of the best-fit Woods-Saxon potential found by Brandan [27]. While the grazing angular momentum value for the reflection coefficient $|S(l)|$ is almost exactly the same, the MWB S-matrix has a more

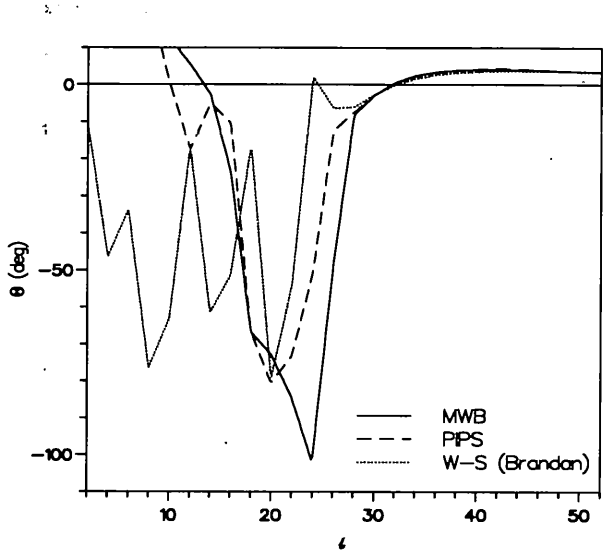

Figure 3.6: Semiclassical deflection functions for 158.8 MeV $^{12}C+^{12}C$ scattering.

diffuse reflection coefficient than that of Brandan's S-matrix, and the real phase shifts are very different for $\ell \leq 26$. This is especially significant in view of the fact that Brandan claims to have obtained completely unambiguous Woods-Saxon parameters for this case. Her claim is based upon the existence of a region of exponential falloff in the cross-section at large angles, indicating the presence of a nuclear rainbow. An examination of Fig. 3.6 shows that the semiclassical deflection function derived from Brandan's S-matrix does indeed have a minimum for $\Theta > -90°$, so that both the criteria for eliminating discrete ambiguities in the real potentials laid out in Goldberg and Smith's paper [37] are satisfied. These criteria are that:

1. the measurements must be performed at a bombarding energy high enough that the monotonic exponential falloff at large angles appears; i.e., that the nuclear

rainbow angle ($\Theta_R(l_R)$) is less than 180° for non-identical particles and less than 90° for identical particles,

2. the measurements must extend to angles beyond the nuclear rainbow angle.

This is not really true for the MWB S-matrix, since the rainbow is predicted at $\Theta_R \sim 100°$. However, it *is* true for the parameter-improved phase shifts (PIPS) fit, which interestingly predicts *exactly the same* rainbow angle as Brandan's Woods-Saxon fit at *exactly the same* l-value. This is intriguing, since the PIPS and Brandan's S-matrix were arrived at from completely different starting points. This indicates that both the PIPS S-matrix fit and Brandan's Woods-Saxon potential fit have succeeded in incorporating information from the nuclear rainbow and exponential falloff region of the cross-section. Figs. 3.7 and 3.8 show the superiority of the PIPS fit to the cross-section data, especially beyond $\sim 30°$. The phase shifts for Brandan's W-S potential seem to behave strangely for the low partial waves, becoming very large and negative as $l \to 0$. The corresponding deflection function also has irregular behaviour, predicting several spurious rainbows at $l = 26$, $l = 18$, $l = 12$, etc. The PIPS deflection function, on the other hand, has the advantage of being related to an analytically smooth MWB $\Theta(l)$, and so has a much more regular and physically reasonable behaviour while still predicting the same physical phenomena (e.g., rainbow angle) as the Brandan $\Theta(l)$. Combining these advantages with the very much lower χ^2/N for the PIPS fit (3.2 for the 'target' PIPS $S(l)$ against 24 for Brandan's Woods-Saxon fit), we believe that the PIPS S-matrix, and by implication its inverted potential, is preferable to Brandan's 'unique' Woods-Saxon potential.

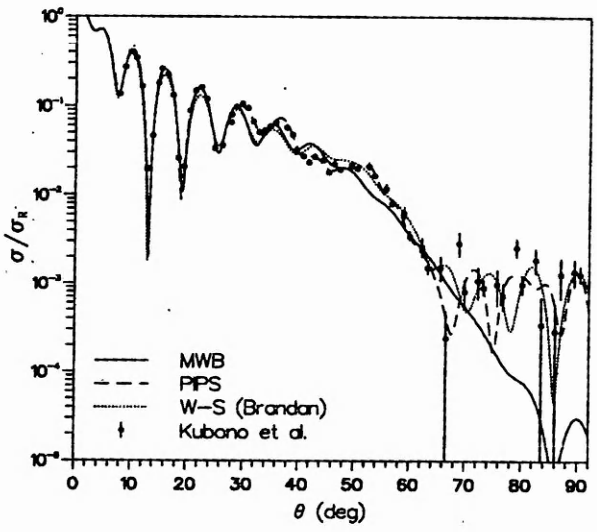

Figure 3.7: Elastic differential cross-sections for 158.8 MeV ^{12}C+^{12}C scattering.

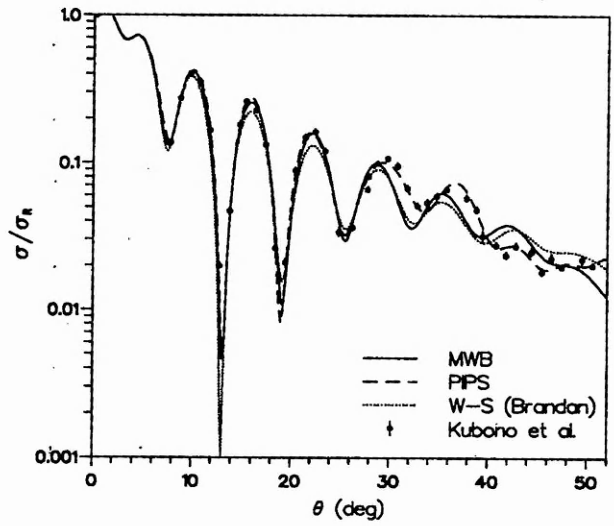

Figure 3.8: Elastic differential cross-sections for 158.8 MeV ^{12}C+^{12}C scattering ($\theta = 0°$–$50°$).

The same, however, cannot be said about the MWB S-matrix. As stated above, it predicts a nuclear rainbow angle which is anomalously large and occurs for too large an l-value, and which disagrees with the predictions of both the PIPS S-matrix and the best-fit Woods-Saxon. Furthermore, as Figs. 3.7 and 3.8 show, the MWB S-matrix completely fails to fit the Airy maximum at about 55°, and misses the exponential falloff. This is due to the large magnitude of Θ_R, as mentioned above. Even though the value of χ^2/N for the MWB fit is about equal to that of the Woods-Saxon fit (24.2 for the MWB against 24 for Brandan's fit), we feel that Brandan's Woods-Saxon fit is preferable to the MWB both because it is a better overall fit to the cross-section (as Fig. 3.7 shows clearly) and because it succeeds in approximately fitting the region of the rainbow angle and exponential falloff. The MWB S-matrix was useful, however, as a starting point for the PIPS fit, which itself is a much better fit to the data than the Woods-Saxon, especially over the 30°– 50° region.

161.1 MeV: The experimental data for this case presented particular difficulty when trying to fit it with an S-matrix. The experimental points do not follow any smooth curve, and I feel that many of the data points must be subject to a greater error than that quoted. I managed to obtain both MWB and PIPS S-matrix fits, however, with smooth cross-section curves but with high values of χ^2/N (8.2 for the MWB fit and 5.1 for the PIPS). As can be seen from Fig. 3.9, the PIPS S-matrix has remained very close to the MWB form, and as a consequence the deflection function has also remained very similar, the main difference being that the rainbow minimum has become sharper. As Fig. 3.10 shows, the Fraunhofer diffraction oscillations were fitted better by the PIPS

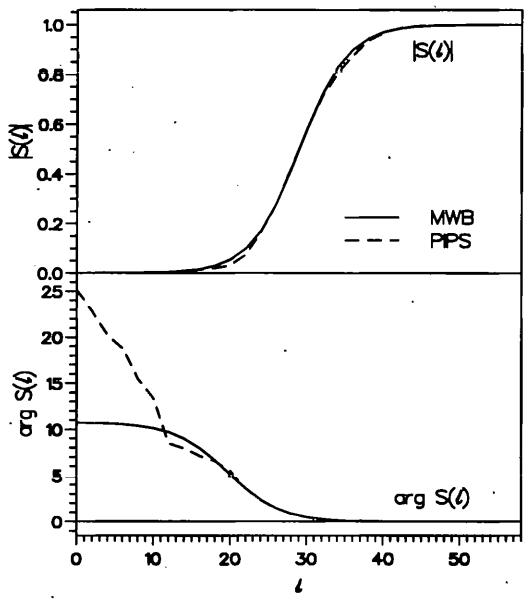

Figure 3.9: Fitted S-matrices for 161.1 MeV ^{12}C+^{12}C scattering.

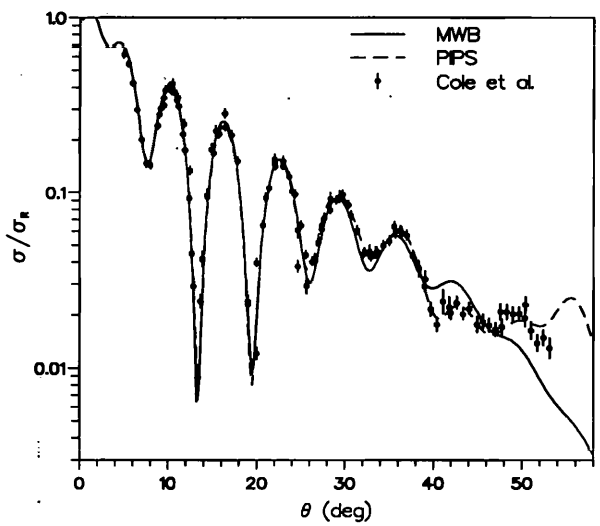

Figure 3.10: Elastic differential cross-sections for 161.1 MeV ^{12}C+^{12}C scattering.

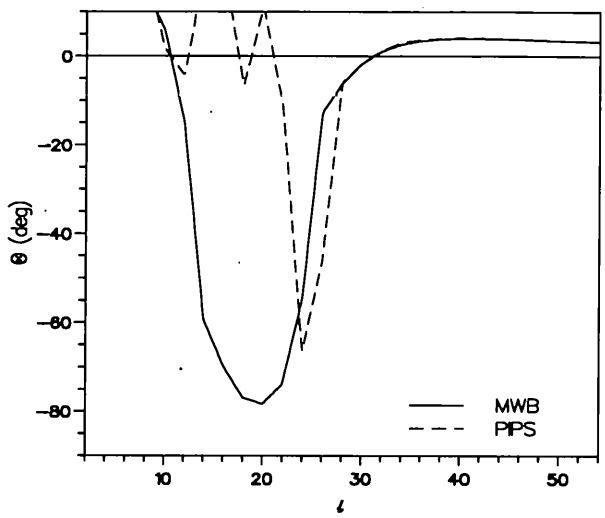

Figure 3.11: Semiclassical deflection functions for 161.1 MeV $^{12}C+^{12}C$ scattering.

$S(l)$, especially beyond 25°, although this led to only a slight decrease in χ^2/N. No Woods-Saxon parameters were available for this case.

288.6 MeV: The data for 288.6 MeV was relatively easy to fit with a smooth curve, and very good values of χ^2/N were obtained for both the MWB and the PIPS fit, as Figs. 3.12 and 3.13 show. As with the 158.8 MeV case, the MWB and PIPS S-matrices were very similar to each other and quite different from the Woods-Saxon S-matrix, being more diffuse than Brandan's Woods-Saxon $S(l)$. Another similarity with the 158.8 MeV case was that the grazing angular momentum for $|S(l)|$ was virtually identical for all three S-matrices.

The differences between the MWB and PIPS S-matrix fits and that of Brandan's Woods-Saxon are very striking when the deflection functions from all three S-matrices

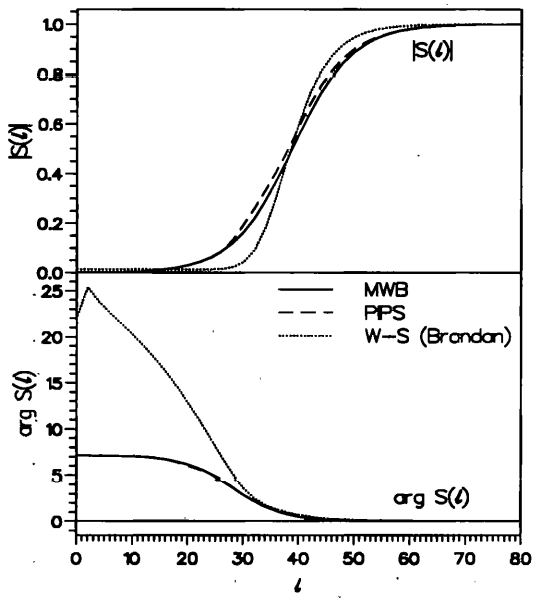

Figure 3.12: Fitted S-matrices for 288.6 MeV ^{12}C+^{12}C scattering.

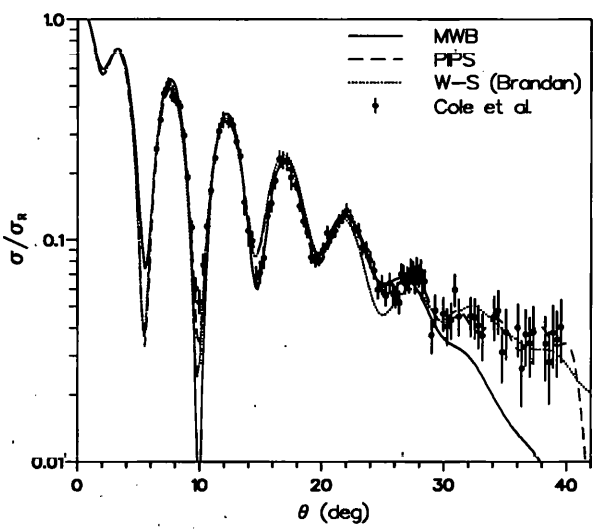

Figure 3.13: Elastic differential cross-sections for 288.6 MeV ^{12}C+^{12}C scattering.

are examined (Fig. 3.14). The Woods-Saxon S-matrix predicts an anomalously high

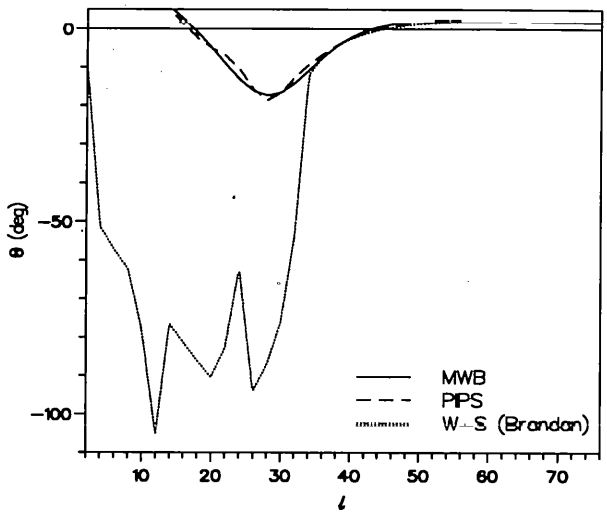

Figure 3.14: Semiclassical deflection functions for 288.6 MeV $^{12}C+^{12}C$ scattering.

nuclear rainbow angle of $\sim$ 100°, contrary to its expected energy dependence. This is not consistent with the 'unique' Woods-Saxon obtained by Brandan for 158.8 MeV, which predicts a shallower minimum in $\Theta(l)$ than the Woods-Saxon for 161.1 MeV, whereas it is firmly expected that the magnitude of Θ_R will decrease as the bombarding energy increases. This is indeed what both the MWB and PIPS S-matrix fits predict; the magnitude of the rainbow angle decreases from $\sim$ 75° to about 20° from 161.1 to 288.6 MeV.

A value of 3.65 for χ^2/N was achieved with the MWB fit, compared to 3.3 for Brandan's Woods-Saxon potential. This was improved to 1.2 with the 'target' PIPS S-matrix. The MWB fit is better than the Woods-Saxon up to about 25°, while the Woods-Saxon is a much closer fit beyond that angle, the MWB completely underes-

timating the cross-section at the larger angles. This behaviour is similar to that at 158.8 MeV, where the MWB fit to the data is better than the Woods-Saxon for angles up to 30°, but completely underestimates the cross-section at larger angles, while the Woods-Saxon approximately fits the data over the entire angular range.

360 MeV: As with the data for the 161.1 MeV case, this set of experimental data proved difficult to fit with physically reasonable S-matrix elements. The results are shown in Figs. 3.15, 3.16 and 3.17. The PIPS phase shifts have a very slight negative tail at large l-values, which gave rise to an equally slight positive tail in the real potential at large radii when the S-matrix was inverted using the code IMAGO. The MWB S-matrix, of course, was constrained by its form to be physically reasonable, but this constraint led to quite a high value of χ^2/N (~ 4 compared with ~ 8 for the Woods-Saxon fit). I believe that these problems arose from deficiencies in the data themselves, and are probably due to some uncertainty in the overall normalisation of the cross-section.

Fig. 3.15 compares the sets of S-matrix elements, the main difference being a decrease in absorption for l =30–40 and the disappearance of the non-zero reflection coefficient of the Woods-Saxon $S(l)$ at the lowest partial waves in the MWB and, especially, the PIPS S-matrix. The magnitude of the MWB and PIPS real phase shifts is lower than that of the Woods-Saxon, especially for the lowest partial waves. The three S-matrices differ widely in the value of the nuclear rainbow angle, ranging from $-20°$ for the PIPS fit, through $-105°$ for the MWB to $-85°$ for the Woods-

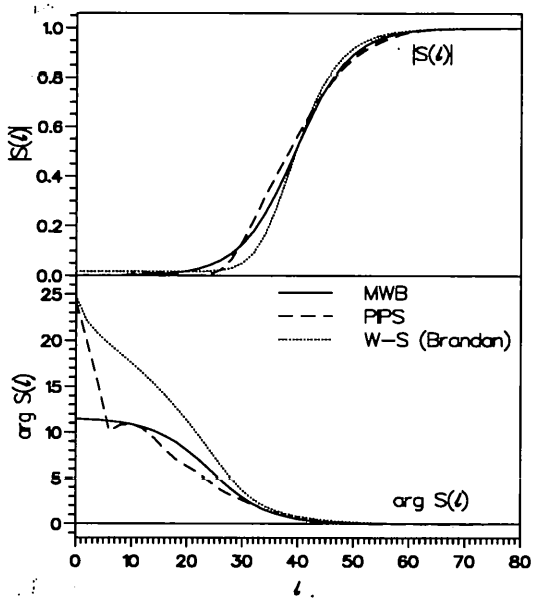

Figure 3.15: Fitted S-matrices for 360 MeV ^{12}C+^{12}Cscattering.

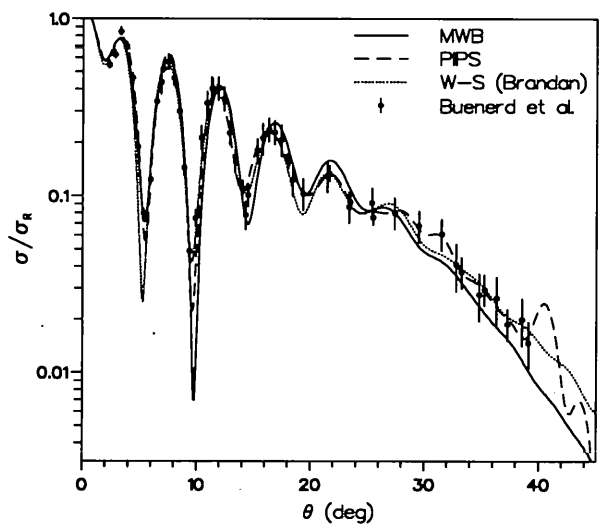

Figure 3.16: Elastic differential cross-sections for 360 MeV ^{12}C+^{12}C scattering.

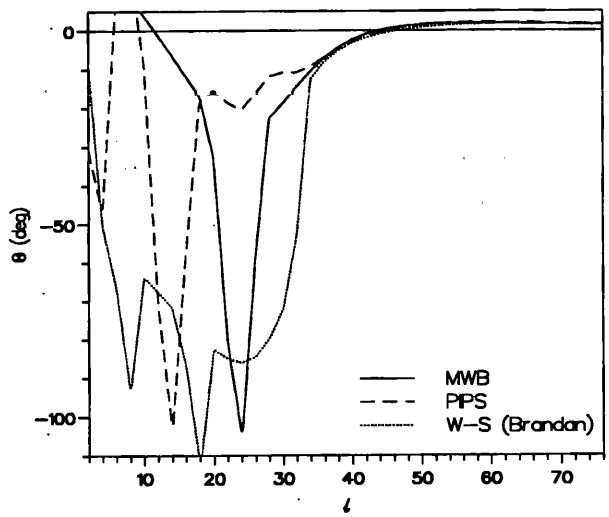

Figure 3.17: Semiclassical deflection functions for 360 MeV $^{12}C+^{12}C$ scattering.

Saxon, although all agree that the rainbow occurs at $l_R = 24$. The expected energy dependence of Θ_R is clearly being violated by the MWB fit, where the magnitude of Θ_R has jumped from $\sim 20°$ at 288.6 MeV to $\sim 105°$ for 360 MeV. The Woods-Saxon fit is therefore preferable to the MWB at this energy, despite the lower value of χ^2/N for the MWB fit. The PIPS fit, on the other hand, predicts a more physically acceptable value for Θ_R than the MWB, but which is very different from that of the Woods-Saxon. The spurious rainbow angle at $l = 14$ of the PIPS fit will be washed out by the strong absorption of those low partial waves.

1016 MeV: Both the MWB and the PIPS S-matrices, Fig. 3.18, are strikingly different from the Woods-Saxon S-matrix found by Brandan. The Woods-Saxon S-matrix has a more diffuse reflection coefficient together with incomplete absorption in the low-

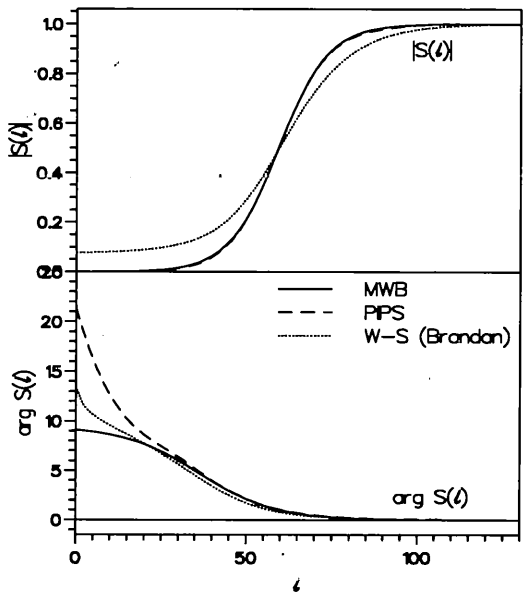

Figure 3.18: Fitted S-matrices for 1016 MeV ^{12}C+^{12}C scattering.

est partial waves, although the grazing angular momentum value for $|S(l)|$ is almost identical for all three S-matrices. The PIPS S-matrix is almost identical to the MWB $S(l)$, apart from a larger magnitude of real phase shifts at the lowest partial waves and a slightly longer tail in the phase shifts for large l values. The deflection functions for all three S-matrices, Fig. 3.20, are very similar to each other, and all predict a nuclear rainbow angle at $l_R = 36$ ranging from about 10.5° for the MWB $\Theta(l)$ through 11° for the PIPS $\Theta(l)$ to 12° for the Woods-Saxon $\Theta(l)$. Examining the cross-section in Fig. 3.19, we see that these rainbow angles are located just beyond the end of the Fraunhofer oscillations, so there may indeed be an observable nuclear rainbow in this cross-section, as some authors have asserted [38, 32].

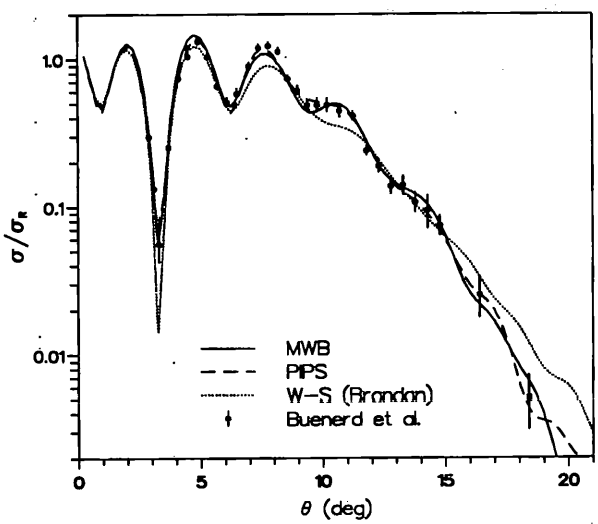

Figure 3.19: Elastic differential cross-sections for 1016 MeV $^{12}C+^{12}C$ scattering.

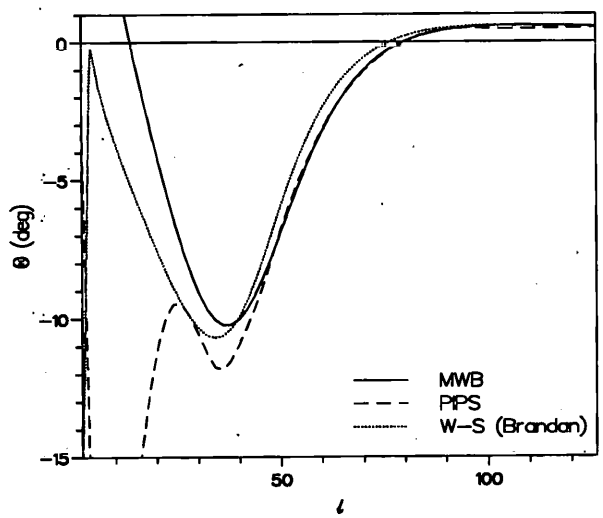

Figure 3.20: Semiclassical deflection functions for 1016 MeV $^{12}C+^{12}C$ scattering.

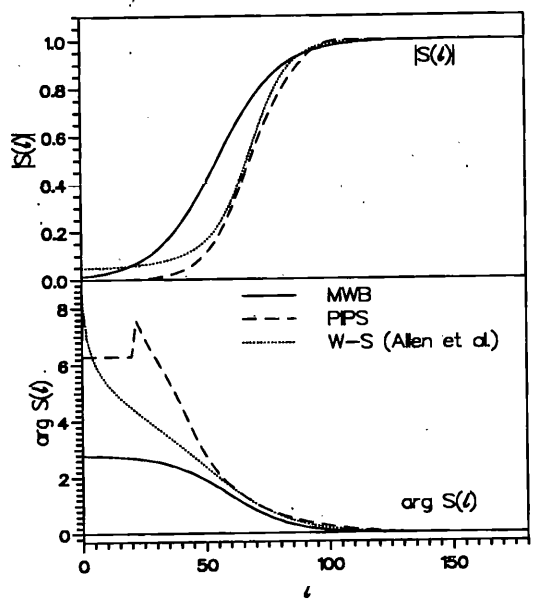

Figure 3.21: Fitted S-matrices for 1449 MeV $^{12}C+^{12}C$ scattering.

1449 MeV: The cross-section data for this energy was, like that for the 288.6 MeV case, relatively easy to fit with an S-matrix. In this case, the PIPS S-matrix fit to the data was very close to the Woods-Saxon $S(l)$, but differed significantly from the MWB fit (see Fig. 3.21). Both the PIPS and W-S fits have less absorption for l =20–99 than the MWB, and greater absorption for $l < 20$. The MWB $|S(l)|$ is also slightly less diffuse than the reflection coefficients of our PIPS and the W-S $S(l)$. The magnitude of the real phase shifts is less for the MWB than for the Woods-Saxon and PIPS, which are very close for l =60–120. An important feature of the PIPS phase shifts is the long tail for large l. While this may not seem to be a large feature in the displayed graph, since it occurs at an l-range which semi-classically can be related to the strong absorption radius, it has a significant effect on the inverse potential, giving an unusually long tail in the real part of the potential for large radii.

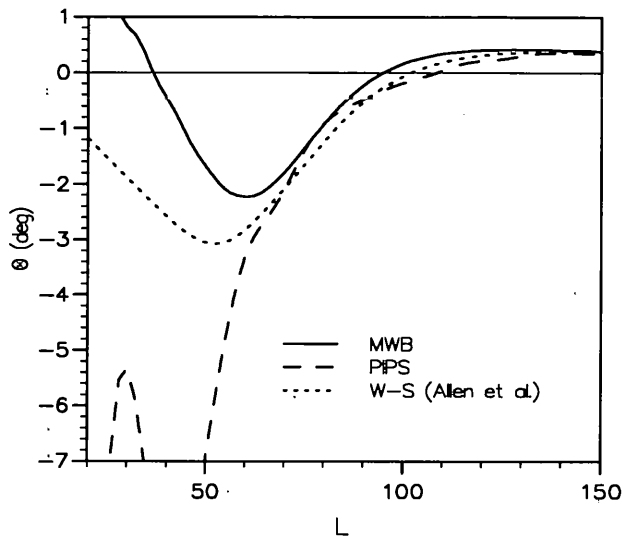

Figure 3.22: Semiclassical deflection functions for 1449 MeV $^{12}C+^{12}C$ scattering.

The Woods-Saxon semiclassical deflection function, Fig. 3.22, predicts a nuclear rainbow angle of about 3° at $l_R = 50$, while the MWB and PIPS $\Theta(l)$ predict rainbow angles of 2.2° and 2.5° respectively at $l_R = 60$. At this angle, it is of course entirely obscured by the Fraunhofer oscillations and no observable rainbow is expected in the cross-section.

The MWB S-matrix (and corresponding inversion potential) fit to the data has a very much lower value of χ^2 per data point than Allen *et al.*'s Woods-Saxon fit. The 'inverse' MWB fit had $\chi^2/N = 4.6$, while the Woods-Saxon had $\chi^2/N = 14.6$. I therefore consider the MWB (even without spline corrections) to be a far preferable fit to the data than Allen *et al.*'s Woods-Saxon fit, especially since (as Fig. 3.23 shows) the Woods-Saxon consistently overestimates the cross-section over almost the entire angular range. The PIPS fit is even more preferable, having $\chi^2/N = 1.5$ and fitting

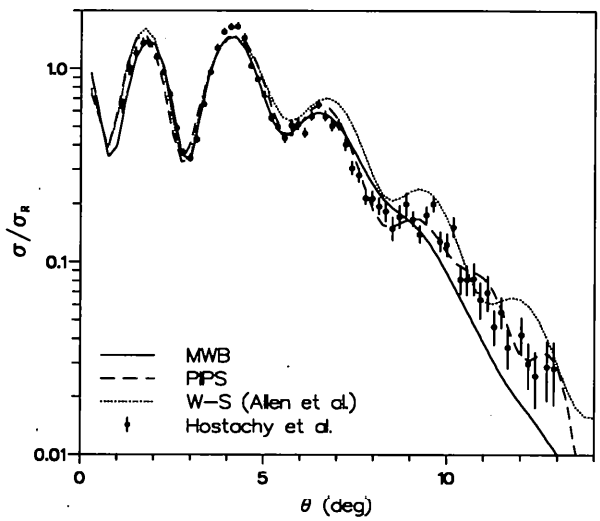

Figure 3.23: Elastic differential cross-sections for 1449 MeV $^{12}C+^{12}C$ scattering.

the data for $\theta > 9°$, where the MWB (as at other energies) underestimates the cross-section.

2400 MeV: In this case, the S-matrix is very close to that derived from the Woods-Saxon potential found by Allen *et al.*, as Fig. 3.24 shows. This is to be expected, since the greater surface transparency at the higher energies allows a deeper probing of the internuclear potential and a corresponding reduction in potential ambiguities, and hence in S-matrix ambiguities. The fact that there should be such agreement between S-matrices obtained by such different methods suggests that the potential has been determined relatively unambiguously. Indeed, the only differences between the S-matrix elements are a marginally greater grazing angular momentum value for the Woods-Saxon $|S(l)|$ and a greater magnitude for low partial waves of the real phase

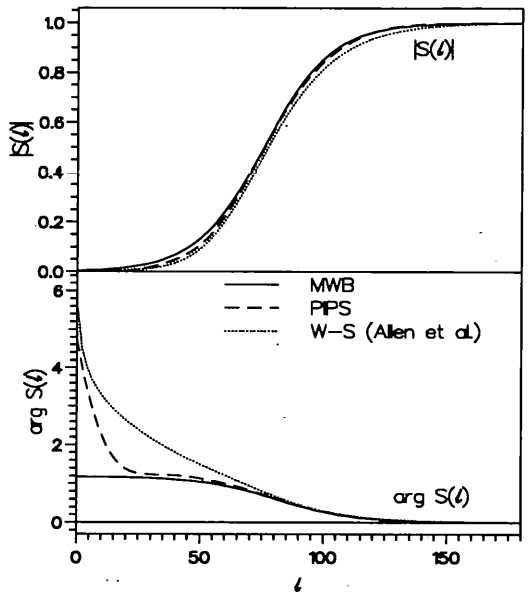

Figure 3.24: Fitted S-matrices for 2400 MeV $^{12}C+^{12}C$ scattering.

shifts of the Woods-Saxon S-matrix.

The deflection functions in Fig. 3.25 for all three S-matrices fit into the expected energy dependence, having very small rainbow angles for quite large values of l_R.

Fig. 3.26 shows that the Woods-Saxon fit tends consistently to overestimate the cross-section, just as it did at 1449 MeV, while the MWB provides a better fit at smaller angles but underestimates the cross-section at larger angles. The PIPS fit is far preferable to either the MWB or Woods-Saxon, as it approximately fits the data over the entire angular range and manages to fit the small oscillations at 5° and 6° which the other two S-matrices miss. Despite this, the actual value of χ^2/N for the PIPS fit is quite high ($\chi^2/N = 10.5$ for the 'inverse' PIPS S-matrix, compared to ~ 45 for the Woods-Saxon and 17.6 for the 'inverse' MWB). This is undoubtedly due to the unusually small error bars on the data points, and the single anomalously low

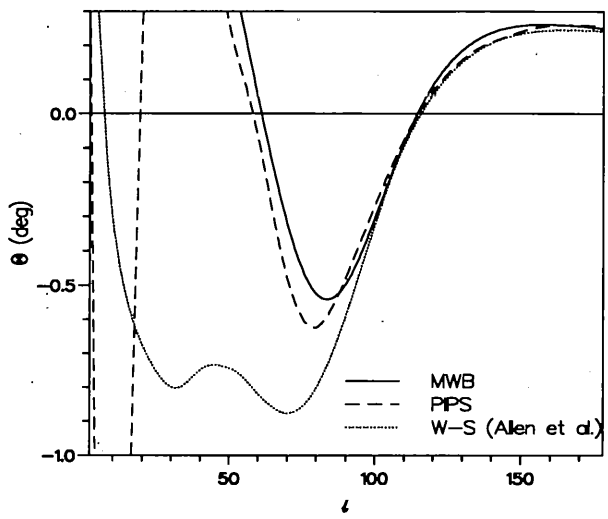

Figure 3.25: Semiclassical deflection functions for 2400 MeV $^{12}C+^{12}C$ scattering.

data point at about 8.8° which means that none of the S-matrices can fit both it and its surrounding data points simultaneously. The overall shape of the cross-section, however, is very closely followed by the PIPS fit, and the appearance of the fit to the eye is very much better than the large χ^2 value would lead one to expect.

Comparison of MWB S-matrices: Figs. 3.27 through 3.30 directly compare the fitted MWB S-matrices for the various energies, as well as the corresponding semiclassical deflection functions. It can be seen from these figures that the reflection coefficients $|S(l)|$ become more diffuse as the energy increases, while the real phase shifts only start to become more diffuse at the higher energies above 360 MeV. As expected, the grazing angular momenta of the modulus and argument of the S-matrices, l_g and l'_g, systematically increase with energy. It should be noted that a qualitative change in $|S(l)$

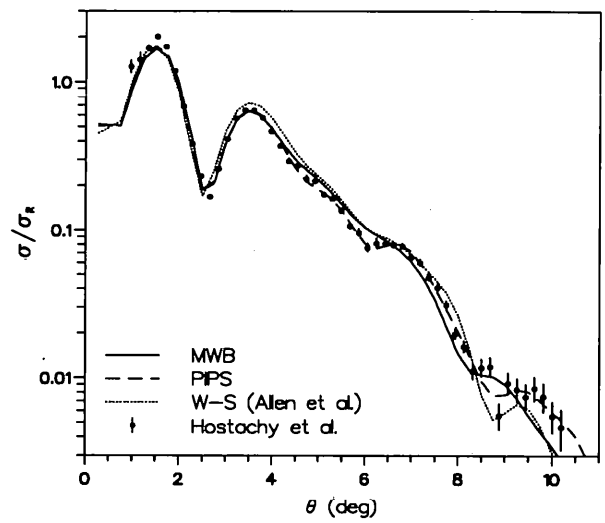

Figure 3.26: Elastic differential cross-sections for 2400 MeV $^{12}C+^{12}C$ scattering.

between 1016 MeV and 1449 MeV present in the MWB fits (see Fig. 3.28) is absent from the PIPS fits (Fig. 3.32). This is further evidence for the greater accuracy and flexibility of the PIPS fit.

The semiclassical deflection function associated with the real phase shifts are displayed in Figs. 3.29 and 3.30. They show the expected energy dependence of the nuclear rainbow minimum—it systematically becomes shallower and centred on a higher value of l_R as the bombarding energy increases. A strong exception to this is the $\Theta(l)$ for the 360 MeV case, which has an anomalously high magnitude for Θ_R ($|\Theta_R| \sim 100°$) and a value of l_R which is lower than that for 288.6 MeV. The real phase shifts of the 360 MeV MWB S-matrix do not therefore fit in with the systematic behaviour of those of the other S-matrices. I believe that this anomaly is due to an uncertainty in the overall normalization of the cross-section data, as mentioned before.

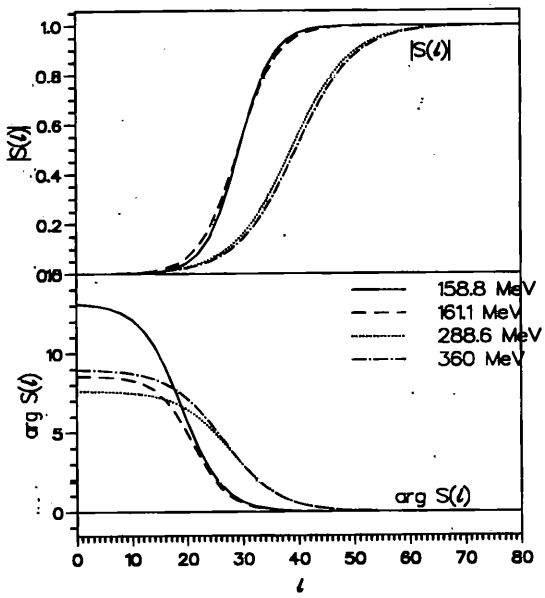

Figure 3.27: Fitted MWB S-matrices for $^{12}C+^{12}C$ scattering (158.8–360 MeV).

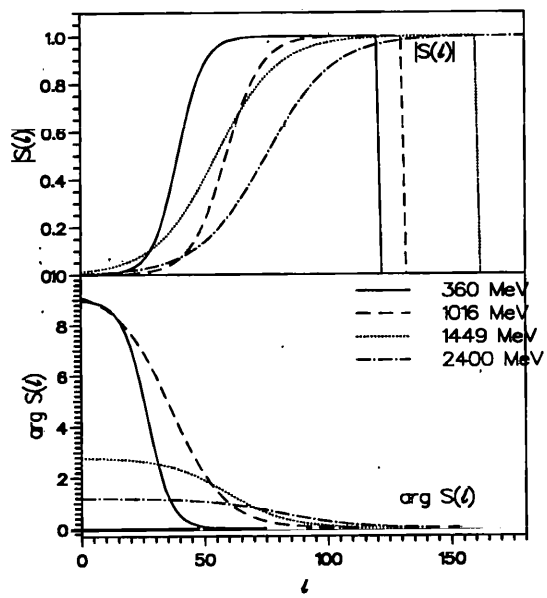

Figure 3.28: Fitted MWB S-matrices for $^{12}C+^{12}C$ scattering (360–2400 MeV).

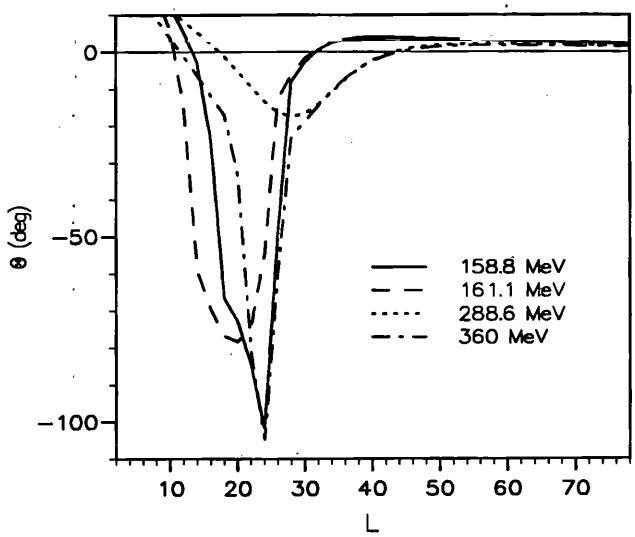

Figure 3.29: Fitted MWB deflection functions for $^{12}C+^{12}C$ scattering (158.8–360 MeV).

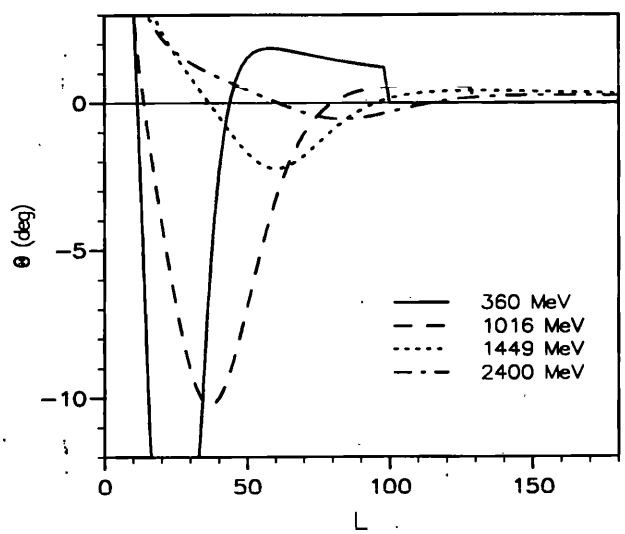

Figure 3.30: Fitted MWB deflection functions for $^{12}C+^{12}C$ scattering (360–2400 MeV).

The cutoff at high l is an artefact of data storage and has no physical significance.

Comparison of PIPS S-matrices: Figs. 3.31 through 3.34 display the PIPS S-matrices for the various energies, together with their semiclassical deflection functions. The reflection coefficients $|S(l)|$ of the PIPS S-matrices show the same systematic behaviour with energy as the MWB reflection coefficients—they become more diffuse as the bombarding energy is increased. The real phase shifts similarly display the same systematic energy dependence as those of the MWB $S(l)$ for the high partial waves, but tend to differ widely at the low partial waves ($l < 16$). The behaviour of the phase shifts at these very low l values is not well-determined by the experimental data, and the presence of strong absorption at these low partial waves deprives these low l phase shifts of any physical significance.

This is also true for the PIPS deflection functions shown in Figs. 3.33 and 3.34. The values of $\Theta(l)$ for $l < 16$ or so are not well-determined by the experimental data.

Again, the 360 MeV case does not follow the systematic behaviour of the other cases—its nuclear rainbow angle has a magnitude which is too large, and is centred at too low an l value. This reinforces the view that the anomaly found for the MWB 360 MeV S-matrix was not due to the restrictions of the MWB form, since it is also found for the PIPS S-matrix, but is due to a systematic error in the experimental cross-section. Apart from this one case, all other PIPS deflection functions have the expected systematic dependence on energy.

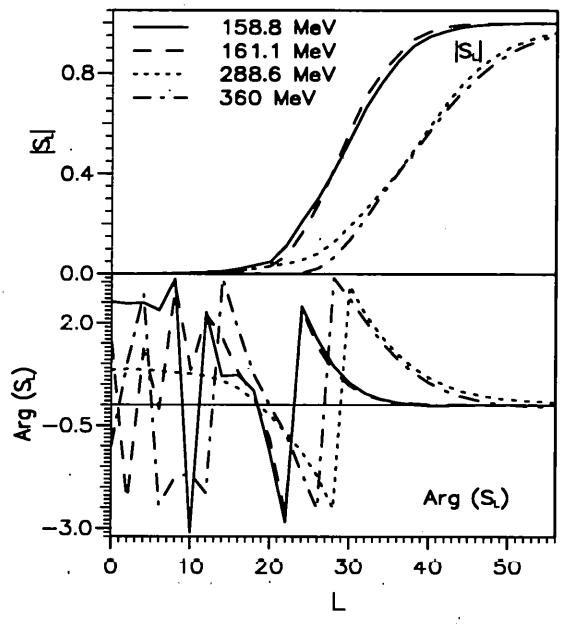

Figure 3.31: Fitted PIPS S-matrices for ^{12}C+^{12}C scattering (158.8–360 MeV). Arg(S_{L}) is plotted with the range $-\pi$ to π.

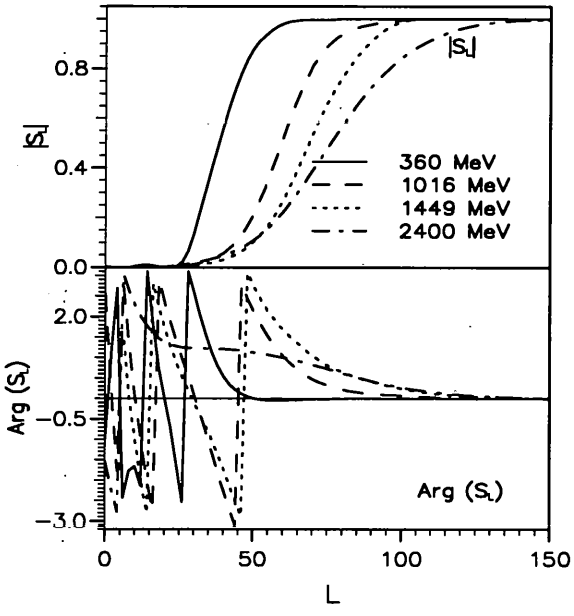

Figure 3.32: Fitted PIPS S-matrices for ^{12}C+^{12}C scattering (360–2400 MeV). Arg(S_{L}) is plotted with the range $-\pi$ to π.

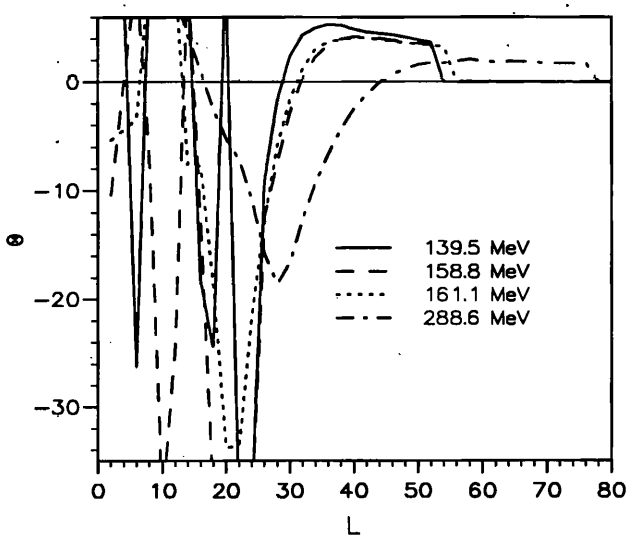

Figure 3.33: Fitted PIPS deflection functions for $^{12}C+^{12}C$ scattering (158.8–360 MeV). The cutoff at high l is an artefact of data storage and has no physical significance.

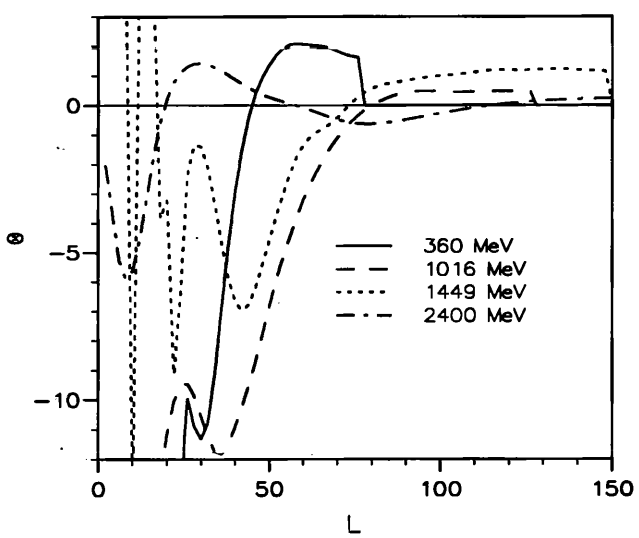

Figure 3.34: Fitted PIPS deflection functions for $^{12}C+^{12}C$ scattering (360–2400 MeV). The cutoff at high l is an artefact of data storage and has no physical significance.

3.3.3 Inversion potentials for $^{12}C+^{12}C$ elastic scattering

Figs. 3.35 through 3.48 display the inversion potentials (MWB and PIPS compared with a standard Woods-Saxon in all cases except 161.1 MeV) obtained by using the iterative-perturbative inversion method on the 'target' or 'fitted' S-matrices displayed earlier. In each case, I have also given the ratio of the imaginary to the real part of the potential, W/V, as a function of radius.

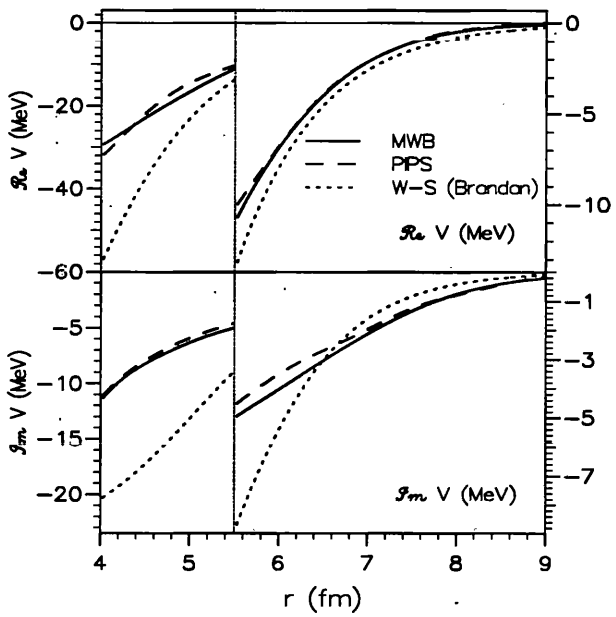

Figure 3.35: Inversion potentials for 158.8 MeV $^{12}C+^{12}C$ scattering.

158.8 MeV: As can be seen from Fig. 3.35, the PIPS potential has remained quite close to the MWB potential, apart from the region $r < 1.5$ fm which has no influence on the cross-section anyway due to the strong absorption of low partial waves. Both the MWB and PIPS potentials have consistently shallower real parts than Brandan's 'unique' Woods-Saxon potential, but follow the same shape as the Woods-Saxon over

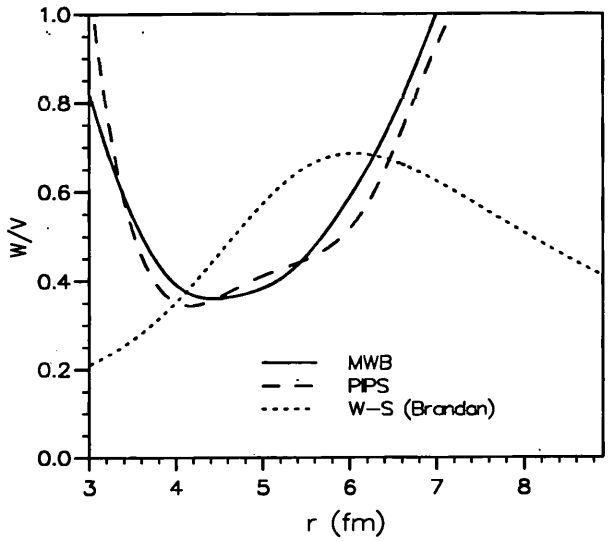

Figure 3.36: W/V for 158.8 MeV $^{12}C+^{12}C$ scattering.

the region of the strong absorption radius (SAR). The imaginary potential, however, is shallower in the Woods-Saxon case for $r > 6.5$ fm, and crosses over the MWB and PIPS absorptive potentials at about 6.5 fm, becoming deeper than either of them between about 3.5 and 6.5 fm. This difference between the behaviour of the real and imaginary parts of the potentials is reflected in the graph of W/V given in Fig. 3.36. There, it can be seen that both the MWB and PIPS potentials have very high values of W/V in the region of the SAR (which is about 7.35 fm at this energy), while the Woods-Saxon has $W/V \sim 0.5$–0.6 in this region, reaching a maximum of about 0.7 where the graphs cross. For intermediate regions (4–6 fm), the MWB and PIPS potentials have a lower W/V than the Woods-Saxon, falling to a minimum of 0.4 at about 4.5 fm. The potential for radial values less than about 3 fm has no physical effect on the observed cross-section, and so is not well-determined. The behaviour of W/V for $r < 3$ fm is

likewise of no physical significance.

161.1 MeV: Woods-Saxon parameters were not available for this case, and only the MWB and PIPS potentials are plotted in Figs. 3.37 and 3.38. As with the 158.8 MeV and all other cases, the MWB potential has a characteristic repulsive core. The PIPS potential has again remained very close to the MWB potential, especially in the sensitive surface region, only beginning to diverge widely for $r < 3.5$ fm. This is reflected in the graph of W/V, where the two potentials show the same overall behaviour in W/V, having a minimum at $r \sim 4.5$ fm and a maximum at $r \sim 8$ fm. The PIPS potential, however, shows greater transparency in the far surface, beyond about 8.5 fm.

288.6 MeV: The MWB and PIPS potentials at 288.6 MeV in Figs. 3.39 and 3.40 are both shallower in the real part than Brandan's Woods-Saxon, although the PIPS is closer to the Woods-Saxon than the MWB, especially in the far surface. The imaginary potentials show the same comparative characteristics as in the 158.8 MeV case—the Woods-Saxon is shallower than the other two in the far surface ($r > 6.5$ fm), but deeper in the intermediate radial region (3.5–6.5 fm). This seems to indicate a systematic deficiency in the imaginary part of the Woods-Saxon form of potential; the Woods-Saxon is simply too constrained in its imaginary part to properly fit the data for $^{12}C+^{12}C$ scattering in this energy range.

The graphs of W/V in Fig. 3.40 show that the PIPS potential is intermediate in that respect between the MWB and the Woods-Saxon, especially in the surface region

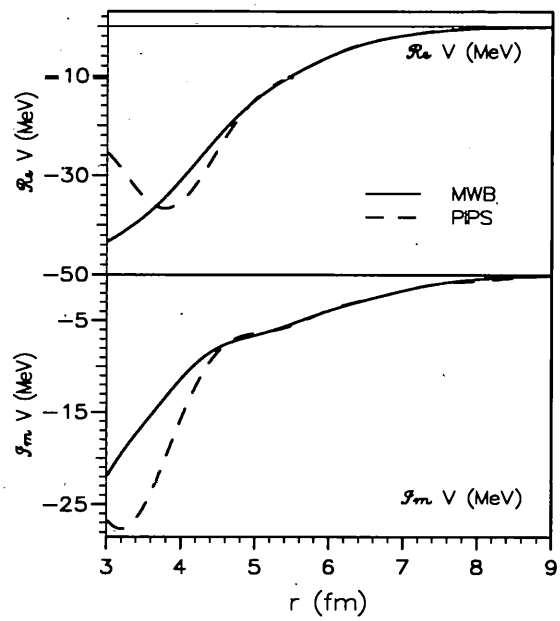

Figure 3.37: Inversion potentials for 161.1 MeV ^{12}C+^{12}C scattering.

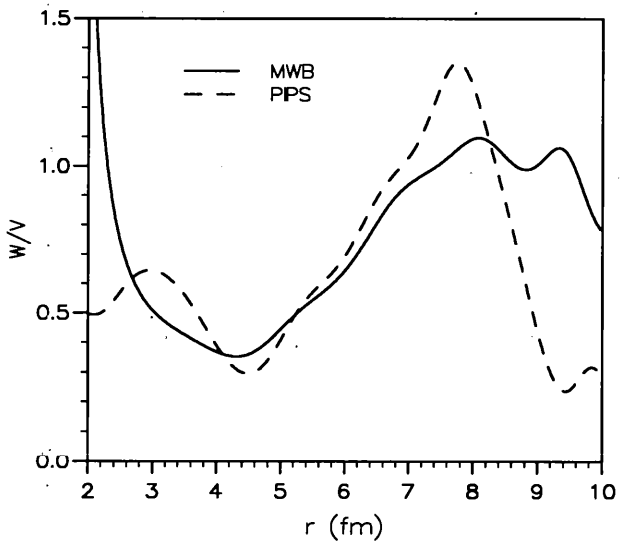

Figure 3.38: W/V for 161.1 MeV ^{12}C+^{12}C scattering.

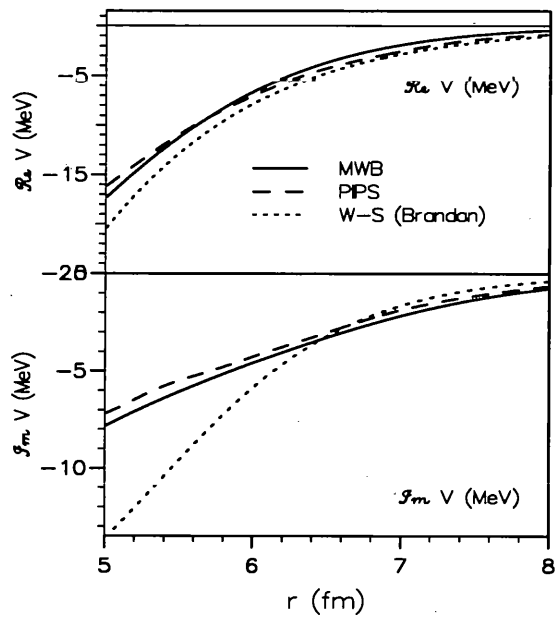

Figure 3.39: Inversion potentials for 288.6 MeV $^{12}C+^{12}C$ scattering.

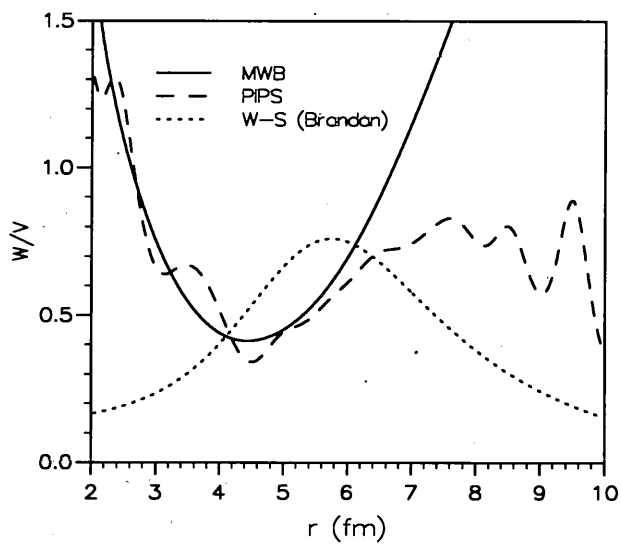

Figure 3.40: W/V for 288.6 MeV $^{12}C+^{12}C$ scattering.

beyond about 6.5 fm.

360 MeV: The real part of the potentials at 360 MeV in Fig. 3.41 shows the same comparative behaviour as at lower energies—namely, the Woods-Saxon real potential is consistently deeper than both the MWB and PIPS in the surface and intermediate region, while the MWB and PIPS real potentials are very similar to one another in the surface region. The imaginary part of the potentials also exhibits the same comparative behaviour as at lower energies, though it is not so marked in this case—the Woods-Saxon is shallower for $r > 6.5$ fm, and deeper between about 3.5 and 6.5 fm. This behaviour is mirrored in the graphs of W/V at this energy in Fig. 3.42, which show the MWB and PIPS potentials to be much more absorptive than the Woods-Saxon in the surface region around the SAR (which is about 6.3 fm in this case), and more transparent in an intermediate region (although not by very much in this case).

1016 MeV: The behaviour of the potentials relative to the Woods-Saxon fits now changes from what it was at the four lower energies. As Fig. 3.43 shows, at 1016 MeV the real part of the Woods-Saxon potential is now shallower than that of the MWB and PIPS over almost the entire radial range, while the imaginary part of the Woods-Saxon is very much deeper in the sensitive surface region beyond the SAR (about 5.5 fm at this energy), becoming shallower for $r < 5$ fm.

The MWB and PIPS potentials themselves are also significantly different from one another, but in the far surface region only (the radial region of $r < 3$ fm is not well-determined by the data), the PIPS real potential especially being deeper than

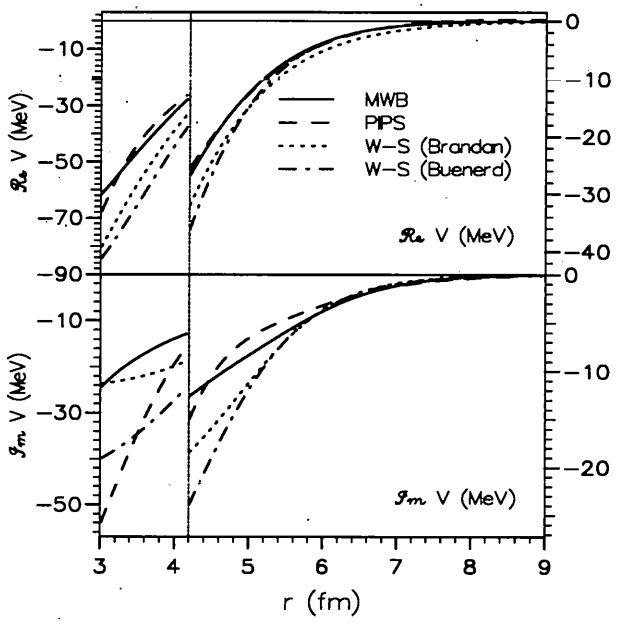

Figure 3.41: Inversion potentials for 360 MeV ^{12}C+^{12}C scattering.

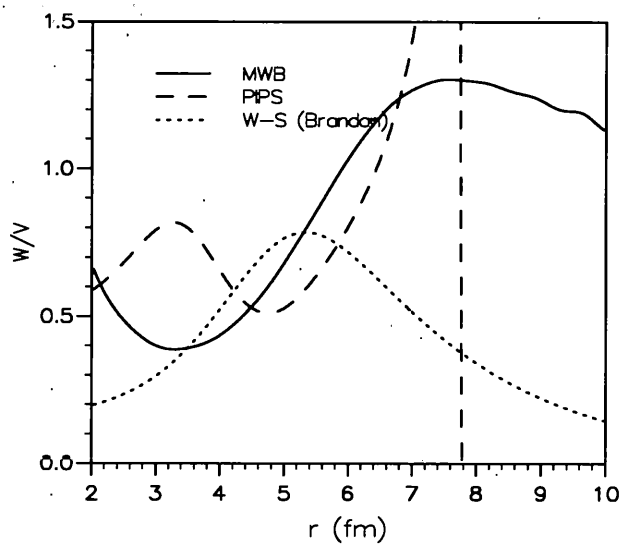

Figure 3.42: W/V for 360 MeV ^{12}C+^{12}C scattering.

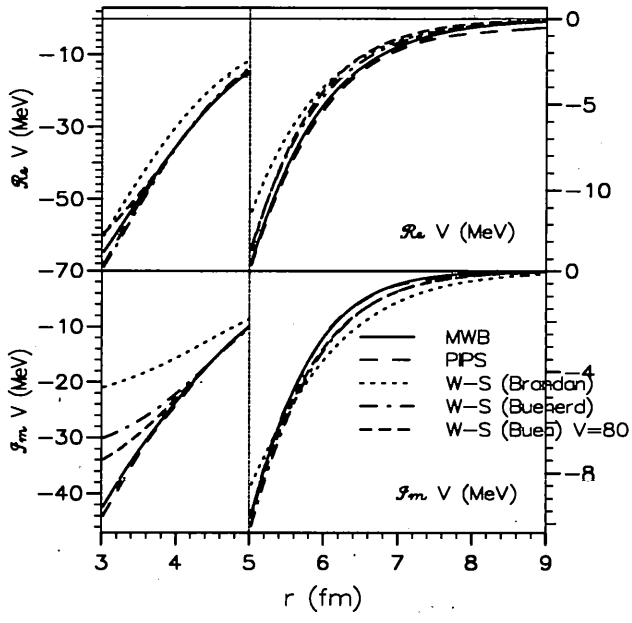

Figure 3.43: Inversion potentials for 1016 MeV $^{12}C+^{12}C$ scattering.

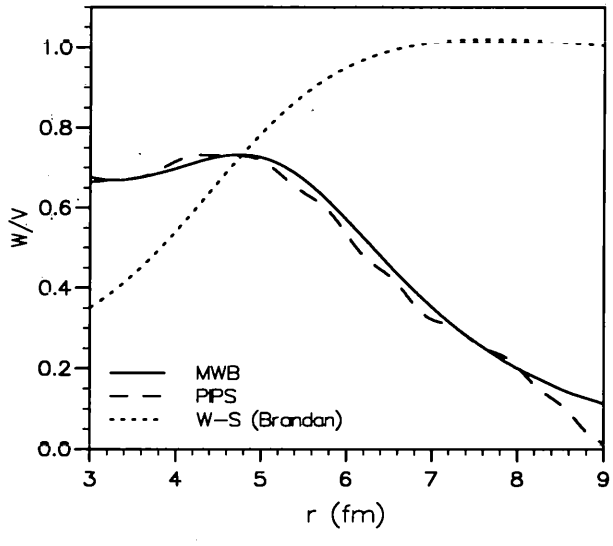

Figure 3.44: W/V for 1016 MeV $^{12}C+^{12}C$ scattering.

the MWB and having a longer surface tail. The imaginary part also exhibits this characteristic, though not to the same degree.

The differences between the Woods-Saxon and the other potentials are particularly striking when the graphs of W/V are examined in Fig. 3.44. We can clearly see the greater surface transparency of both the MWB and the PIPS potentials; the Woods-Saxon has $W/V \sim 1$ in the far surface, while the MWB and PIPS W/V is virtually zero in this radial region. At the SAR, however, the ratio W/V of all three potentials are almost exactly equal.

When the quality of fit of the MWB and PIPS potentials ($\chi^2/N = 3.57$ for the MWB and 1.57 for the PIPS fits, compared with $\chi^2/N \sim 7$ for the Woods-Saxon) is taken into account, it can be concluded that the greater surface transparency of the MWB and PIPS potentials is necessary in order to achieve a high quality of fit to the scattering data. This enhanced surface transparency at 1016 MeV is, I believe, further evidence in favour of the existence of an observable nuclear rainbow at about 10–12°, as claimed by some authors [38, 32].

1449 MeV: The real part of the Woods-Saxon potential is deeper than that of the MWB over the entire radial range (see Fig. 3.45), but is shallower than that of the PIPS in the very far surface ($r > 7$ fm), due to the fact that the real part of the PIPS potential has an unusually long surface tail extending out to about 13 fm.

The imaginary potentials have the same comparative behaviour they had at the lowest energies, with the Woods-Saxon being shallower than my potentials in the sur-

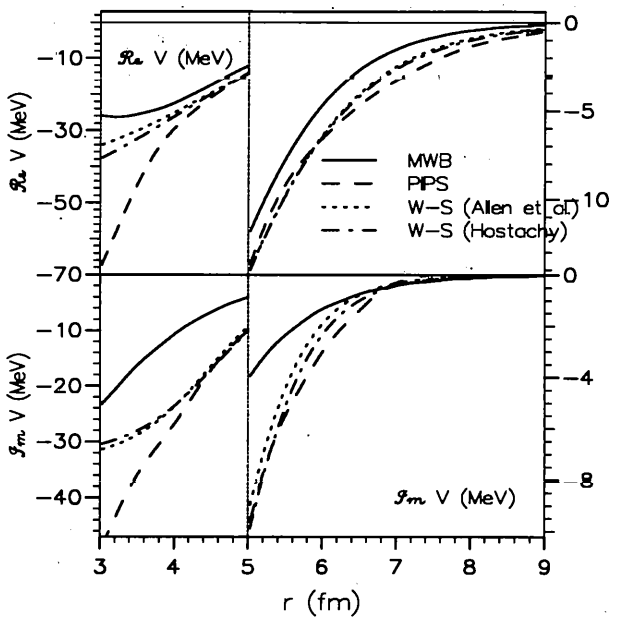

Figure 3.45: Inversion potentials for 1449 MeV ^{12}C+^{12}C scattering.

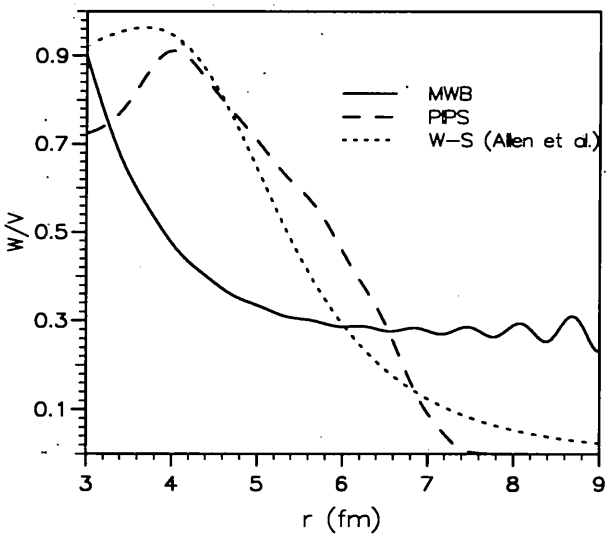

Figure 3.46: W/V for 1449 MeV ^{12}C+^{12}C scattering.

face region beyond about 6.5 fm, and deeper in an intermediate region between about 2.5 and 6.5 fm.

The PIPS and W-S potentials have approximately the same kind of radial behaviour of W/V—there is strong absorption for low radial values, falling to very small values (representing surface transparency) in the far surface. Only the MWB potential has W/V significantly different from zero beyond about 9 or 10 fm. Given the poor fit of the W-S to the cross-section data (see Fig. 3.23), the data points towards a strongly surface transparent potential at this energy. Indeed, the PIPS W/V for 1449 MeV is similar to W/V for 1016 MeV, which also shows surface transparency.

2400 MeV: In the 2400 MeV case, Figs. 3.47 and 3.48, both the real and imaginary parts of the Woods-Saxon potentials are slightly shallower than those of the MWB and PIPS. In the real part, the difference (especially between the Woods-Saxon and the PIPS potentials) are very slight indeed, and all three potentials have almost identical real parts in the radial region between about 4 and 6 fm (the SAR at this energy is about 4.8 fm), so we can say that the potential is completely well-determined in the sensitive radial region centred around the SAR. For the imaginary part, the potentials are almost exactly equal between about 4 and 5 fm.

An examination of the comparative radial behaviour of W/V at this energy, as displayed in Fig. 3.48, bears this out. All three potentials show strong absorption for $r < 4.5$ fm, with surface transparency for radial values greater than about 6 fm.

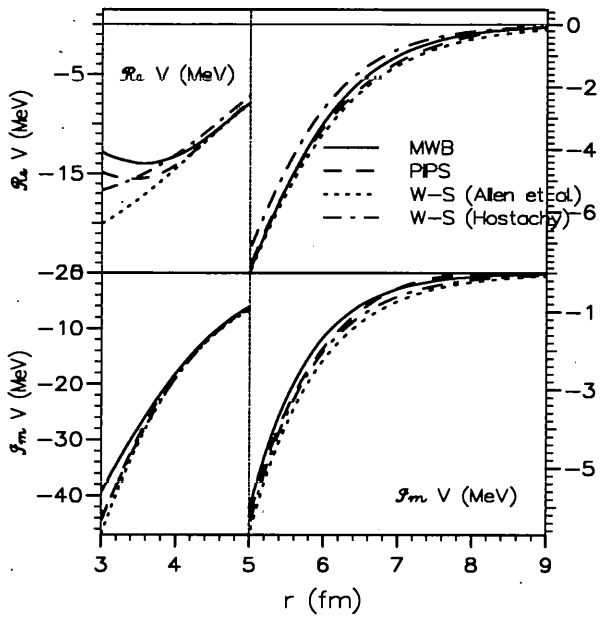

Figure 3.47: Inversion potentials for 2400 MeV ^{12}C+^{12}C scattering.

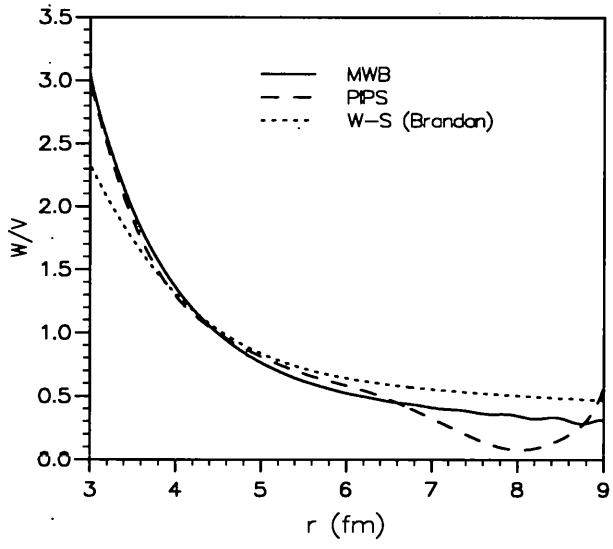

Figure 3.48: W/V for 2400 MeV ^{12}C+^{12}C scattering.

Comparison of 'MWB' potentials: The MWB potentials for the various energies are displayed in Figs. 3.49 to 3.52, together with the ratio of the imaginary to real potentials W/V as a function of radius.

A table of potential values at the strong absorption radius is given in Table 3.7.

$E_{\rm lab}$ (MeV)	158.8	161.1	288.6	360	1016	1449	2400
R_s (fm)	7.36	7.05	7.03	6.30	5.53	4.67	4.76
$-V(r=R_s)$ (MeV)	1.25	1.69	1.78	2.45	8.30	15.3	9.26
$-W(r=R_s)$ (MeV)	1.50	1.61	2.10	2.76	5.54	5.58	8.00
$W/V(r=R_s)$	1.20	0.95	1.17	1.12	0.67	0.36	0.86

Table 3.7: Potential strengths at the strong absorption radii, R_s, using MWB S-matrices.

An interesting feature (not shown in the plots) is the repulsive core, which appears at all the energies. This seems to be a characteristic of the MWB form of the S-matrix, and the same feature was reported by Allen *et al.* [18] in their inversion of MWB S-matrices both in the case of ^{12}C+^{12}C scattering and ^{16}O scattering at 1503 MeV, and the same repulsive core appeared in the MWB potential for ^{16}O+^{12}C at 608 MeV.

As can be seen from Figs. 3.49 to 3.52, the real part of the MWB potentials has a very slight tendency to become shallower in the surface region as the bombarding energy increases, with the notable exception of the 360 MeV case, which is actually shallower than the three higher energies in the very far surface. In fact, the 360 MeV and 2400 MeV potentials are both very much shallower in the surface region of the real

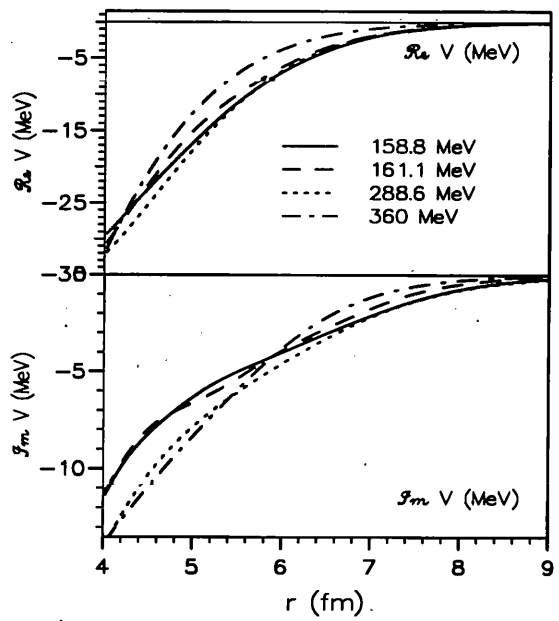

Figure 3.49: MWB inversion potentials for $^{12}C+^{12}C$ scattering (158.8–360 MeV).

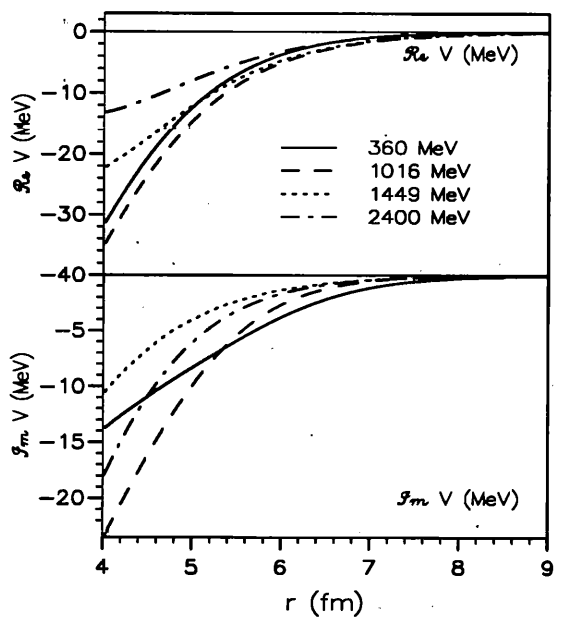

Figure 3.50: MWB inversion potentials for $^{12}C+^{12}C$ scattering (360–2400 MeV).

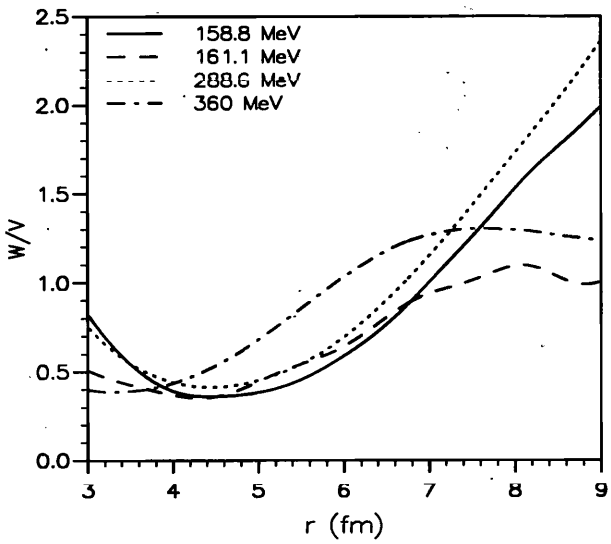

Figure 3.51: W/V for the MWB inversion potentials for $^{12}C+^{12}C$ scattering (158.8–360 MeV).

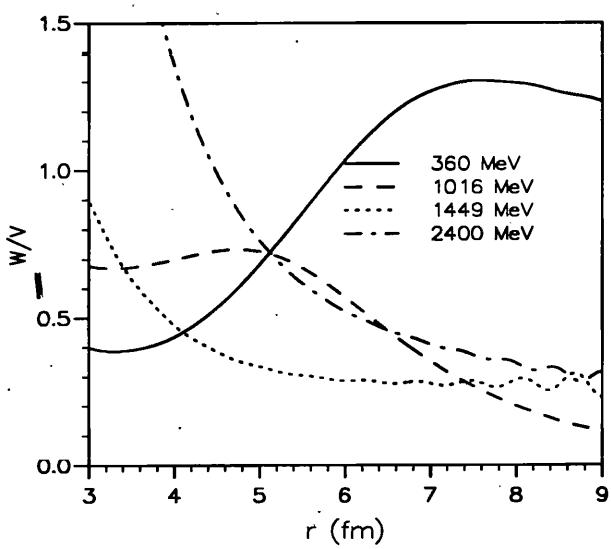

Figure 3.52: W/V for the MWB inversion potentials for $^{12}C+^{12}C$ scattering (360–2400 MeV).

part than any of the other energies, which tend to have very similar real potentials for $r > 6$ fm.

The imaginary part of the MWB potentials tends to become shallower as the energy increases. This is to be expected, since absorption in the surface region is reduced at the higher energies, which will tend to shift the imaginary part of the potential inwards to smaller radii. An exception to this systematic behaviour is the 288.6 MeV case, which has an imaginary part very close to that of 158.8 MeV in the surface region ($r > 7$ fm), indicating a surprisingly strong absorption at this energy. The graphs of W/V for the MWB potentials (Figs. 3.51 and 3.52) emphasise this point, showing the 288.6 MeV case to have a very high ratio of W/V in the far surface; in fact, the radial behaviour of the 288.6 MeV potential is broadly very similar to that of the 158.8 MeV case.

In general, of course, the graphs of W/V for the MWB potentials display the tendency towards greater surface transparency as the bombarding energy is increased, as expected.

Comparison of 'PIPS' potentials: A table of potential values at the strong absorption radius R_s and at four other (fixed) radii is given in Table 3.8. The four other radii are those at which the nuclear charge density has fallen to 1% (R_1), 5% (R_5), 10% (R_{10}) and 20% (R_{20}) of its central value at the point of overlap between the nuclei. I used a three-parameter Fermi fit given by C.W. de Jager *et al.* to elastic electron scattering data [39].

E_{lab} (MeV)	158.8	161.1	288.6	360	1016	1449	2400
R_s (fm)	7.33	7.12	6.91	6.28	5.53	4.86	4.80
$-V(r = R_s)$ (MeV)	1.31	1.44	2.73	2.62	8.59	14.8	8.86
$-W(r = R_s)$ (MeV)	1.43	1.55	2.01	2.45	5.46	5.48	7.74
$W/V(r = R_s)$	1.09	1.08	0.74	0.93	0.63	0.37	0.87
R_1 (fm)	8.75	8.75	8.75	8.75	8.75	8.75	8.75
$-V(r = R_1)$ (MeV)	0.06	0.21	0.42	-0.19	0.60	0.69	0.09
$-W(r = R_1)$ (MeV)	0.27	0.14	0.29	0.12	0.03	0.06	0.03
$W/V(r = R_1)$	4.47	0.66	0.69	-0.63	0.06	0.09	0.27
R_5 (fm)	7.30	7.30	7.30	7.30	7.30	7.30	7.30
$-V(r = R_5)$ (MeV)	1.38	1.10	1.72	0.38	1.35	1.75	0.85
$-W(r = R_5)$ (MeV)	1.48	1.29	1.37	0.85	0.40	0.29	0.19
$W/V(r = R_5)$	1.07	1.17	0.80	2.20	0.30	0.16	0.23
R_{10} (fm)	6.61	6.61	6.61	6.61	6.61	6.61	6.61
$-V(r = R_{10})$ (MeV)	3.39	2.88	3.79	1.63	2.72	3.16	1.78
$-W(r = R_{10})$ (MeV)	2.53	2.68	2.74	1.80	1.11	0.80	0.79
$W/V(r = R_{10})$	0.75	0.93	0.72	1.11	0.41	0.25	0.44
R_{20} (fm)	5.82	5.82	5.82	5.82	5.82	5.82	5.82
$-V(r = R_{20})$ (MeV)	7.79	7.24	8.07	4.83	6.30	6.46	3.81
$-W(r = R_{20})$ (MeV)	3.81	4.68	4.67	3.61	3.68	1.99	2.33
$W/V(r = R_{20})$	0.49	0.65	0.58	0.75	0.58	0.31	0.61

Table 3.8: PIPS potential at R_s, R_1, R_5, R_{10} and R_{20} for $^{12}C+^{12}C$ scattering.

Some problems were experienced with the 158.8 and 360 MeV PIPS potentials—they have small positive tails in the far surface (i.e., beyond the SAR) of the real potential, and any attempt to remove them by fitting an exponential tail in the surface of the potential destroys the fit to the cross-section data; for example χ^2/N increases from $\sim$5 to $\sim$12 in the 158.8 MeV case. This anomaly in the far surface shows itself in Table 3.8, in the high value of W/V at 8.75 fm for 158.8 MeV and the negative value of W/V at the same radius for 360 MeV. Since Arg(S_l) has a small negative tail at large l, this anomaly is probably due to non-physical features in the PIPS 'target' S-matrices rather than representing failures of the IP inversion method itself, which works perfectly well at 288.6 MeV.

The real part of the PIPS potentials behave in much the same way as the MWB potentials—they are approximately equal in the surface region, with a slight tendency to become shallower as the energy increases (though this is much less marked than it is with the MWB potentials), with the strong exceptions of the 360 and 2400 MeV cases, which are both very much shallower in the surface than are the other cases.

The absorptive potential tends, as expected (since the projectile spends less time in the absorptive region at the higher bombarding energies), to become shallower in the surface region as the bombarding energy is increased, with the exception of the 288.6 MeV potential, which is now quite close to the 161.1 MeV imaginary potential at intermediate radial values and to the 158.8 MeV in the far surface.

The graphs of W/V for the PIPS potentials again show the general trend towards greater surface transparency as the bombarding energy is increased. The graphs for

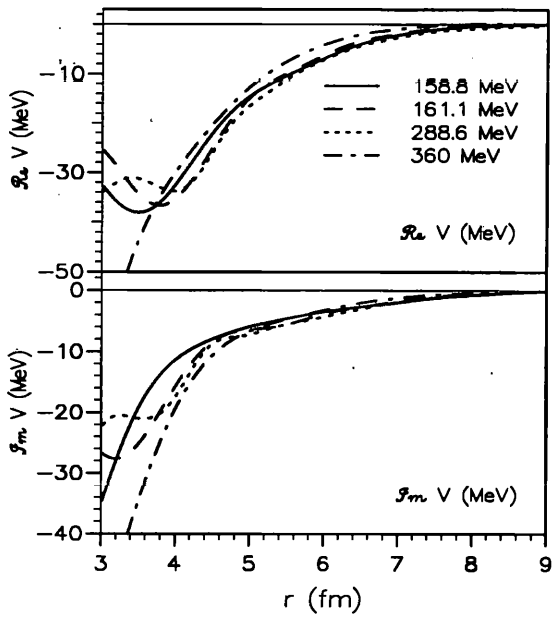

Figure 3.53: PIPS inversion potentials for $^{12}C+^{12}C$ scattering (158.8–360 MeV).

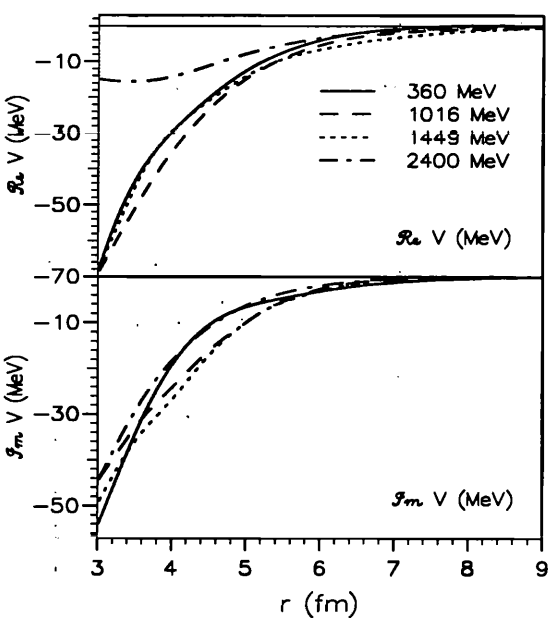

Figure 3.54: PIPS inversion potentials for $^{12}C+^{12}C$ scattering (360–2400 MeV).

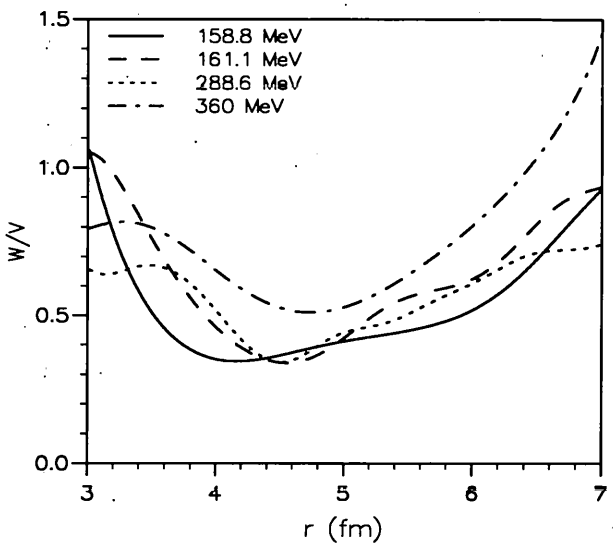

Figure 3.55: W/V for PIPS inversion potentials for $^{12}C+^{12}C$ scattering (158.8–360 MeV).

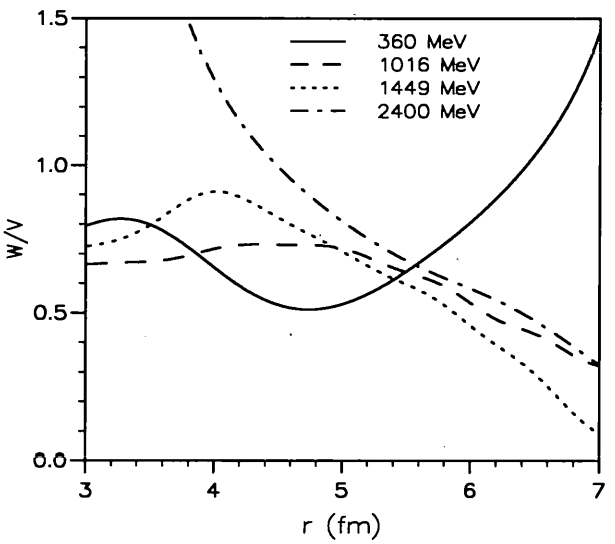

Figure 3.56: W/V for PIPS inversion potentials for $^{12}C+^{12}C$ scattering (360–2400 MeV).

158.8 MeV and 360 MeV have a singularity due to the existence of the small positive tails in the very far surface, as noted earlier. The sudden increase in W/V for $r > 8$ fm in the 2400 MeV case is not physically realistic and may be due to a slight positive tail in the very far surface of this potential also.

3.3.4 Conclusions

It was found that characteristically all the real parts of the MWB potentials are attractive wells modulated by a short range repulsion, as found by Steward *et al.* [40], Buenerd *et al.* [32] and in the present study of ^{16}O on ^{12}C at 608 MeV. The depth of the attractive wells tends to increase with energy up to 1016 MeV, whereupon the trend reverses and the wells become shallower as the energy increases. This indicates that simple functional forms, e.g. Woods-Saxon functions with smooth energy-dependent parameters, are unlikely to be able to fit these cases accurately over this range of energies. The well minima, however, are far inside the SAR for all cases, and the PIPS potentials do not have this characteristic attractive well with repulsive core. Clearly, then, the noticeable onset of the repulsion in the MWB inversion potentials is well inside the lower bound of the sensitive radial region for scattering, so that the cross-section data cannot discriminate between the presence or the absence of the repulsive core. Furthermore, at these small radii, the absorption is very strong so that the short range details of the inversion potentials will have a negligible effect on calculations of the differential cross-sections. It is one of the conclusions of the present analysis that the potentials obtained by inversion from the MWB parametrisation of the S-matrix

are inadequate when compared with those obtained from S-matrices which more accurately fit the cross-section data. This is true even when the inversion procedure is as accurate and model-independent as the IP method. However, it can be useful as a starting point for the PIPS method, where the smooth parametrised form of an MWB S-matrix can be modified with spline corrections to obtain a much more accurate fit, from which an inverse potential can be found using the IP inversion method.

It was concluded from the present analysis, using PIPS S-matrices and inverse potentials, that the sensitive region around the SAR moved to smaller radii as the bombarding energy increased and that, at certain fixed radii (R_1, R_5, R_{10} and R_{20}), the absorptive potential strength decreased with energy, contrary to some microscopic model predictions [41].

Fig. 3.57 shows the distribution of the transmission coefficients $T(l)$ (where $T(l) = 1-|S(l)|^2$) for the PIPS potentials as a function of the internuclear distance of minimum approach D associated with the partial wave angular momentum l, assuming a Coulomb trajectory. Since this assumption is not strictly true, especially for low values of D and the higher energies, Fig. 3.57 should be regarded only as a qualitative picture of the radial dependence of the absorption. Only the transmission coefficients for the four highest energies have been given. For the lower energies, the SAR (i.e., the value of D for which $T(D) = \frac{1}{2}$) monotonically decreases as the energy increases, as expected. It is the systematic behaviour of $T(D)$ for the very highest energies which is of interest; the graph clearly shows that the SAR has almost completely ceased to decrease with energy between 1016 MeV and 1449 MeV. This implies that the nuclear

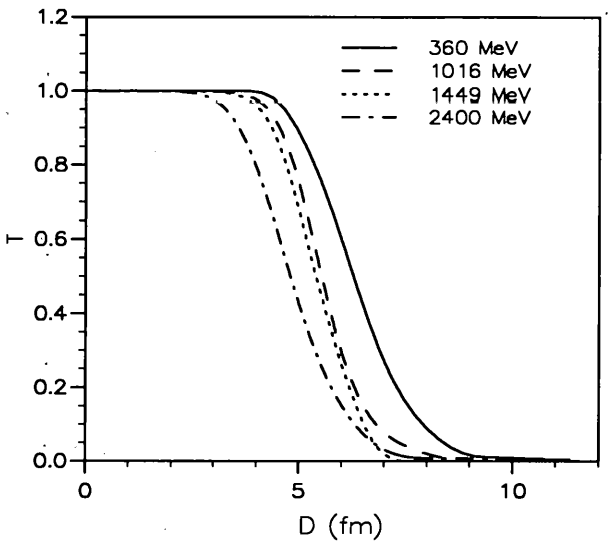

Figure 3.57: Transmission coefficients as a function of semiclassical radius for PIPS potentials for $^{12}C+^{12}C$ scattering (360–2400 MeV).

surface transparency has ceased to increase with energy over this energy range, contrary to what Buenerd *et al.* [32] claim, and in agreement with Brandan *et al.* [42]. Buenerd *et al.* base their claim upon the eikonal approximation, which directly relates the attenuation length of the projectile to the averaged nucleon-nucleon cross-section $\sigma_{\tilde{NN}}$. This decreases to a minimum at about $E/A \sim 300$ MeV, so that the nucleon mean free path during the scattering, which is taken to be inversely proportional to $\sigma_{\tilde{NN}}$ in the eikonal approximation, should increase over the energy range up to $E/A \sim 300$ MeV leading to increased nuclear surface transparency. Buenerd *et al.* themselves claim that the eikonal approximation begins to fail at the higher bombarding energies due to the deeper interpenetration of the nuclei leading to the enhanced importance of higher-order rescattering terms which can be neglected at lower energies. The simple

inverse proportionality between the nucleon mean free path and $\sigma_{\tilde{NN}}$ therefore begins to break down, so that the increase in surface transparency and the value of $\sigma_{\tilde{NN}}$ are no longer so directly related.

In conclusion, it seems that the energy dependence of both the MWB and the PIPS potentials across the sensitive radial regions is not of a sufficiently simple form to be representable by a Woods-Saxon form of potential with parameter values which vary smoothly with energy or mass. With the two-stage PIPS fit to the scattering data, I do not impose any biases either on the radial form of the internuclear potential or on the form of the S-matrix. This inversion method, as a means of finding the nuclear interaction, is a viable and preferable alternative to the conventional optical model analysis. It gives much better fits to the cross-section data than the Woods-Saxon model, and has quite different behaviour than the Woods-Saxon—it is closer to physical reality and has a more credible ratio W/V. Furthermore, it is free from prejudices about the shape of the potential and is a very fast inversion method.

However, it is clear that the functional form for $S(l)$ must be chosen very carefully prior to applying $S(l)$-to-$V(r)$ inversion to it. The iterative-perturbative method is so accurate that the MWB S-matrices are simply not sufficiently good fits to the data to do justice to the IP method; the PIPS S-matrices are required to obtain potentials which are significantly better than a standard Woods-Saxon fit, and which do not contain artefacts of the parametrization chosen for the S-matrix, such as a repulsive core. The two-stage $\frac{d\sigma_{el}}{d\Omega}(\theta)$-to-$S(l)$ plus $S(l)$-to-$V(r)$ inversion procedure requires high quality data. It requires the first stage, in which S-matrices are fitted to the data, to

be carried out to high precision. However, this can be an advantage of the IP method, as it means that it can exploit high quality data, which could motivate more accurate and extensive experimental measurements of scattering data. Furthermore, it can find weaknesses or inconsistencies in existing scattering data. The method developed here has later been applied to ^{11}Li scattering [43].

Part II

Investigating heavy-ion dynamic polarization potentials by coupled reaction channels calculations and inversion

Chapter 4

The method of 'CRC and inversion' as a means of obtaining the heavy-ion dynamic polarization potential (DPP)

In this chapter, we shall present the basic methodology used in the latter part of the thesis — 'CRC and inversion'.

We present first the coupled differential equations for inelastic scattering, then examine the rearrangement channels of the scattering, in which nucleons are exchanged between target and projectile. Such exchanges contribute to the elastic scattering channel. We then demonstrate how, for computational purposes, the full range of coupled channels must be truncated to those having the most important effect on

elastic scattering, in order to make the calculations tractable. This involves replacing the true interaction with an 'effective' interaction which affects only those reaction channels which have been selected for inclusion in the analysis.

We also examine the dynamic polarization potential (DPP), which models the effect on the interaction of the reaction channels.

Finally, in the latter part of the thesis we shall obtain, by inversion, a precise form for various contributions to the DPP associated with important reaction channels in the scattering of some heavy ions near the Coulomb threshold, and examine them to extract information concerning their radial form and relative importance.

4.1 The coupled reaction channels (CRC) method

The coupled channels method for a single partition. We wish to describe the scattering of two nuclei a and A. We will assume that both the projectile and the target are spinless, and we will neglect angular momentum transfer. It is convenient to expand the wavefunction of the scattering system, Ψ, in terms of some complete set of basis functions. We use the product of the wavefunctions of the internal states of the two nuclei:

$$\Psi = \sum_{a'A'} \chi_{a'A'}(\mathbf{r}_\alpha)\psi_{a'}\psi_{A'}, \tag{4.1}$$

which is an infinite sum over all the possible internal states of the nuclei a and A. The term $\chi_{a'A'}(\mathbf{r}_\alpha)\psi_{a'}\psi_{A'}$ would represent a state of the scattering system in which nucleus a is in the internal state $\psi_{a'}$, A is in the state $\psi_{A'}$ and the relative motion between

them is given by $\chi_{\alpha' A'}(\mathbf{r}_\alpha)$, where $\mathbf{r}_\alpha$ is the internuclear separation. The notation can be simplified by writing the expansion as $\Psi = \sum_{\alpha'} \chi_{\alpha'}(\mathbf{r}_\alpha)\psi_{\alpha'}$, where $\psi_{\alpha'} = \psi_{a'}\psi_{A'}$. It is necessary to impose the boundary conditions upon the functions $\chi_{\alpha'}(\mathbf{r}_\alpha)$ for large $\mathbf{r}_\alpha$, that they must have the form of an incoming wave plus an outgoing wave in the entrance channel and only an outgoing wave in all other open channels. Since the internal wavefunctions $\psi_{\alpha'}$ form a complete and orthogonal set, any physical state of the scattering system can be written as a linear superposition of such internal states.

When this expansion of Ψ is inserted into the Schrödinger equation, we get

$$\sum_{\alpha'} \left[(\varepsilon_{\alpha'} - E) - \frac{\hbar^2}{2\mu_\alpha}\nabla_\alpha^2 + V(\mathbf{r}_\alpha) \right] \chi_{\alpha'}(\mathbf{r}_\alpha)\psi_{\alpha'} = 0. \tag{4.2}$$

This can be simplified using the orthogonality property of the internal wavefunctions, $\int \psi_\alpha^*(\tau_\alpha)\psi_{\alpha'}(\tau_a)d\tau_\alpha = \delta_{\alpha\alpha'}$. This is done by multiplying from the left by ψ_α^* and integrating over all the internal co-ordinates (τ_α, say) of the two nuclei. We then obtain:

$$[\nabla_\alpha^2 - V_{\alpha,\alpha}(\mathbf{r}_\alpha) + k_\alpha^2]\chi_\alpha(\mathbf{r}_\alpha) = \sum_{\alpha' \neq \alpha} \chi_{\alpha'}(\mathbf{r}_\alpha)V_{\alpha,\alpha'}(\mathbf{r}_\alpha), \tag{4.3}$$

for arbitrary internal states of a and A, and where $k_\alpha^2 = 2\mu_\alpha(E - \varepsilon_\alpha)/\hbar^2$. The quantity $(E - \varepsilon_\alpha)$ is the kinetic energy of relative motion of the nuclei when they are well-separated and in the internal state ψ_α, and k_α is the wavenumber corresponding to that kinetic energy. To keep the notation within bounds the α subscript on V in Eq. 4.2 refers to the alpha partition, but the subscripts $V_{\alpha,\alpha'}$ refer to channels within the partition.

It is the non-diagonal terms on the right hand side of Eq. 4.3 which lead to transitions out of the ground state, and which describe both inelastic scattering and the effect of virtual excitations on the elastic scattering. In principle, higher-order processes may also make a significant contribution to the elastic scattering amplitude.

The dynamics of the scattering process depend upon the terms $V_{\alpha,\alpha'}(\mathbf{r}_\alpha)$, the matrix elements of the interaction potential V_α, defined as:

$$\begin{aligned} V_{\alpha,\alpha'}(\mathbf{r}_\alpha) &= \frac{2\mu_\alpha}{\hbar^2}\int\int \psi^*_\alpha(\tau_\alpha)V_\alpha\psi_{\alpha'}(\tau_\alpha)d\tau_\alpha \\ &\equiv \frac{2\mu_\alpha}{\hbar^2} < \alpha|V_\alpha|\alpha' > . \end{aligned} \tag{4.4}$$

Since the integrations are only over the internal co-ordinates τ_α, the potential matrix elements will be functions of the internuclear separation $\mathbf{r}_\alpha$.

If we know all the matrix elements $V_{\alpha,\alpha'}$ it would be possible to solve the coupled equations and thereby obtain a maximal description of the reaction. But this is not practical — there are an infinite number of matrix elements, so that obtaining a completely accurate solution would take an infinite amount of computation. The infinite set of equations must be restricted to a finite number, approximating the full wavefunction Ψ with a finite sum:

$$\sum_{\alpha'}^{N} \phi_{\alpha'}(\mathbf{r}_\alpha)\psi_{\alpha'}, \tag{4.5}$$

where N is the number of states included in the finite sum. It is important to note that the functions $\phi_{\alpha'}(\mathbf{r}_\alpha)$ are in general not the same as the $\chi_{\alpha'}(\mathbf{r}_\alpha)$ that appeared in

Eq. 4.1. The justification for this truncation is that there may be only a few channels which are strongly coupled to each other, so that we retain only certain specific channels and represent the effect of the rest by means of a complex effective potential which varies smoothly with energy.

The CRC method with rearrangement channels. So far we have concentrated on the coupled channels method for a single partition, α. There will in general be rearrangement reactions leading to new partitions of the nucleons between the outgoing nuclei, b and B. The formalism of the coupled channels method as described so far is difficult to apply to these rearrangement collisions. The problem is that, although the equations we have presented so far include these events as well as inelastic excitations, in practice a huge number of terms in the expansion of the wavefunction is needed to represent a different partition of the nuclei, β. These terms would include highly excited states of a and A, including unbound states. The original expansion of the scattering wavefunction Ψ must be modified from the outset to include the new partition created by the rearrangement collision [44]:

$$\Psi = \sum_{\alpha}^{N} u_\alpha(\mathbf{r}_\alpha)\psi_\alpha + \sum_{\beta}^{N} u_\beta(\mathbf{r}_\beta)\psi_\beta, \tag{4.6}$$

where the finite sums include only those terms which it is believed will contribute significantly to the coupled reaction channels calculation. More than two partitions may be included in the expansion of Ψ.

The internal wavefunctions from different partitions are not orthogonal. This

means that the 'overlap' function is non-zero:

$$O_{\alpha\beta}(\mathbf{r}_\alpha) = \int \psi^*_\alpha(\tau_\alpha)\psi_\beta(\tau_\beta)d\tau_\alpha \neq 0. \tag{4.7}$$

In general $O_{\beta\alpha} \neq O_{\alpha\beta}$. The formalism for CRC with rearrangement is therefore the same as for coupled channels, with the addition of non-orthogonality terms. The non-orthogonality implies, in particular, that terms like $< \psi_\alpha|u_\beta\psi_\beta >$ are not only non-zero but in general awkward to calculate. However, these terms may be negligible in particular cases.

To make the consequences of this modification to the expansion of the wavefunction clearer, we will examine the simplest case where there are only two states involved, one in each partition. In other words, $\Psi = u_\alpha(\mathbf{r}_\alpha)\psi_\alpha + u_\beta(\mathbf{r}_\beta)\psi_\beta$. Since the Hamiltonian can be written in two equivalent forms, $H = H_\alpha + T_\alpha + V_\alpha$ and $H = H_\beta + T_\beta + V_\beta$, we can write two simultaneous equations for u_α and u_β by projecting the scattering wavefunction onto the two channels:

$$\begin{aligned} < \psi_\alpha|(E - H_\alpha - T_\alpha - V_\alpha)|(u_\alpha\psi_\alpha + u_\beta\psi_\beta) > &= 0 \\ < \psi_\beta|(E - H_\beta - T_\beta - V_\beta)|(u_\alpha\psi_\alpha + u_\beta\psi_\beta) > &= 0 \end{aligned} \tag{4.8}$$

which gives

$$\begin{aligned} [(E - \varepsilon_\alpha) - T_\alpha - < \psi_\alpha|V_\alpha|\psi_\alpha >]u_\alpha(\mathbf{r}_\alpha) &= < \psi_\alpha|(H - E)|u_\beta\psi_\beta > \\ [(E - \varepsilon_\beta) - T_\beta - < \psi_\beta|V_\beta|\psi_\beta >]u_\beta(\mathbf{r}_\beta) &= < \psi_\beta|(H - E)|u_\alpha\psi_\alpha > \end{aligned} \tag{4.9}$$

These coupled equations are in fact the CRC equations for the simplest case of rearrangement collision, where only two channels are involved. The generalisation to more than two rearrangement channels is straightforward.

4.2 The Feshbach formalism; truncation of the wavefunction and the effective interaction

The above results, and their application in this work, can be made clearer if we rewrite them in terms of the Feshbach formalism [3, 4, 5], which uses a concise operator notation.

We define two projection operators P and Q such that $P + Q = 1$. When operating on the total wavefunction of the scattering system $\overline{\Psi}$, P has the effect of projecting out a specified subset of the basis states of $\overline{\Psi}$ which contains only those states which are explicitly included in our analysis of the scattering. The operator Q projects out all the excluded states contained in $\overline{\Psi}$, so that $P\overline{\Psi} + Q\overline{\Psi} = \overline{\Psi}$. In what follows, $\Psi = P\overline{\Psi}$, so thatΨ consists of a finite set of basis functions which includes all the states of importance in the scattering process: $\Psi = \sum_\alpha \phi_\alpha \psi_\alpha(\hat{\mathbf{r}})$. This technique is sometimes referred to as the truncation of the wavefunction.

Those parts of the basis states which represent the internal states of the two nuclei can be either bound states of those nuclei (in which case we are using a 'bound state approximation') or they can include discrete representations of continuum levels (in which case we are using a 'coupled discrete continuum channels' (CDCC) approxi-

mation).

Schrödinger's equation for a complete Hamiltonian $\overline{\mathcal{H}}$ and a total energy E can be written as $(\overline{\mathcal{H}}-E)\overline{\Psi}=0$. Within the model space $P\overline{\Psi}$ we have chosen, this becomes $(\mathcal{H}-E)\Psi=0$. The model Hamiltonian associated with the model wavefunction is defined as:

$$\mathcal{H}=P\overline{\mathcal{H}}P-P\overline{\mathcal{H}}Q\frac{1}{Q\overline{\mathcal{H}}Q-E-i\varepsilon}Q\overline{\mathcal{H}}P. \tag{4.10}$$

The presence of the $-i\varepsilon$ term (in which ϵ is an infinitesimal positive quantity) ensures that flux is removed rather than added to the model space during scattering, and reflects the time irreversibility of the scattering process (since in the P space $\mathcal{H}$ is non-unitary).

It is the second term on the right hand side of Eq. 4.10 which represents the effect on the model space $P\overline{\Psi}$ of the excluded channels — for example, there may be virtual excitations into the subspace $Q\overline{\Psi}$ which return to the subspace $P\overline{\Psi}$ before detection, or a compound nucleus may form during the interaction. Because we have chosen not to examine these channels in any detail, we must create a model Hamiltonian $\mathcal{H}$ (as defined in Eq. 4.10, and sometimes called the effective interaction) with interaction potentials which will approximate the processes represented by Eq. 4.10. This means that such effective potentials will have an imaginary component representing absorption out of the model subspace $P\overline{\Psi}$ (e.g., by compound nucleus formation), and there will be contributions to the real part from virtual excitations into the excluded subspace $Q\overline{\Psi}$. These are known as dynamic polarization potentials.

4.3 The steps in a CRC calculation

The steps which must be taken to actually carry out a CRC calculation can be relatively easily enumerated. The code FRESCO [45] was used for all calculations described here.

The steps are:

1. Input the masses, charges, lab energy, relevant levels, matching radius.

2. Enumerate the channels. The channel depends upon the angular momentum of the scattered particle as well as the nuclear state. Thus if the total angular momentum and parity of the complete system are $I\pi$ then for each nuclear state of spin and parity $J\pi_\alpha$ there will be scattered particles of all angular momenta lj satisfying the condition $\mathbf{I} = \mathbf{j} + \mathbf{J}$ and $\pi = (-1)^l \pi_\alpha$, of which there are in general $2J+1$ when $J < I$ (true for almost all partial waves). Thus for each angular momentum and parity $I\pi$ of the complete system there are

$$N = \sum_{\text{states}} (2J+1) \tag{4.11}$$

channels, where the sum is over the states of the nucleus.

3. Calculate the Coulomb parameters for each level and the centre of mass energies for each level:

$$E = \frac{\mu}{m_p} E_{\text{lab}} \tag{4.12}$$

$$E_c = E - E_{\alpha J} \tag{4.13}$$

$$k_c^2 = \frac{2\mu}{\hbar^2} E_c \tag{4.14}$$

$$\eta_c = \frac{\mu Z_p Z_t e^2}{\hbar^2 k_c}, \tag{4.15}$$

where $E_{\alpha J}$ is the energy of the excited level (J is the spin of the nuclear state and α represents all further quantum numbers needed to specify that state).

4. Calculate the potential matrix elements between channels,

$$V^I_{c'c''}(r) = <\phi_{c'\pi I}(\mathbf{r}, \mathbf{A})|V(\mathbf{r}, \mathbf{A})|\phi_{c''\pi I}(\mathbf{r}, \mathbf{A})>, \tag{4.16}$$

where $\phi_{c'\pi I}(\mathbf{r}, \mathbf{A})$ is the wavefunction of the complete system in channel c' with angular momentum I and parity π.

5. Set up the system of coupled equations:

$$(T_{c'} + V^I_{c'c'}(r) - E_{c'})u_{c'}(r) = -\sum_{c'' \neq c'} V^I_{c'c''}(r)u_{c''}(r), \tag{4.17}$$

where $T_c = -\hbar^2/2\mu\nabla_c^2$ and E is the centre of mass bombarding energy.

6. Solve the coupled equations using, e.g., the Numerov method, with boundary conditions at the origin and the matching radius (i.e., the solutions match onto the asymptotic Coulomb wavefunctions at the matching radius).

7. Apply boundary conditions and calculate the S-matrix elements from the equation

$$u_{c'} \rightarrow I_c(k_c r)\delta_{c'c} - \frac{k_c}{k_{c'}} S^I_{c'c} O_{c'}(k_{c'} r), \tag{4.18}$$

where

$$I_l^* = O_l = \exp[i(kr - \eta \ln(2kr) - l\pi/2 + \sigma_l)], \tag{4.19}$$

where σ_l is the Coulomb phase shift. The delta function is needed because in the channel c (the elastic channel) there are both incoming and outgoing spherical waves at infinity, since there is an incident wave in the elastic channel. In all other channels there are only outgoing waves. The boundary conditions lead to a linearly independent set of solutions for each channel, from which the S-matrix elements can be extracted.

8. Calculate the cross-sections for exciting each of the nuclear states from the S-matrix elements.

4.4 Obtaining the DPP by inversion from a CRC S-matrix

From the S-matrices representing elastic scattering, the program IMAGO [13] yields accurate local potentials corresponding to these S-matrices by a process of inversion. The method is the same as that used in the earlier chapters of this thesis to obtain inverted potentials from elastic S-matrices.

Chapter 5

Investigating $^{16}O+^{62}Ni$ at the Coulomb threshold using 'CRC and inversion'

5.1 Introduction

In this chapter, we investigate the behaviour of the local l-independent potential for $^{16}O+^{62}Ni$ near the Coulomb threshold, using the complementary techniques of coupled reaction channels analysis and model-independent inversion. The experimental elastic scattering cross-section of ^{16}O on even mass nickel isotopes was measured by West *et al.* [46]. The CRC calculations were carried out using the code FRESCO [45], and for the most part we included the same channels as those in Keeley *et al.*'s analysis [47], with the exception of the α-particle transfer channel.

The channels included in the CRC calculations are:

- the inelastic excitation of the 2^+ and 3^- states of ^{62}Ni and the 3^- state of ^{16}O
- the ^{62}Ni(^{16}O,^{17}O)^{61}Ni and ^{62}Ni(^{16}O,^{15}N)^{63}Cu transfer channels
  - for ^{62}Ni(^{16}O,^{17}O)^{61}Ni: the $5/2^+$ and $1/2^+$ states of ^{17}O, and the $3/2^-$, $5/2^-$, $1/2^-$ and $7/2^-$ states of ^{61}Ni
  - for ^{62}Ni(^{16}O,^{15}N)^{63}Cu: the $1/2^-$ state of ^{15}Ni, and the $3/2^-$, $1/2^-$ and $5/2^-$ states of ^{63}Cu.

Two-way couplings between the entrance channel only to each of the relevant transfer channels were included. The residual optical model in the entrance channel is the bare double-folded real potential and a Woods-Saxon-squared imaginary potential, of depth 40 MeV, radius parameter 1.0 fm and diffuseness parameter 0.4 fm. For further details concerning the optical model potentials for propagation in the transfer partitions, spectroscopic factors, etc., see Keeley *et al.*'s paper [47].

The first section of Part II of this thesis, following the introduction, is a preliminary investigation whose purpose is to clarify the significance of an anomalous peak in the energy dependence of the imaginary potential, $W(E,r)$, for ^{16}O+^{62}Ni at the Coulomb threshold. This feature of the optical model potentials was first presented by Keeley *et al.* [47], and is extremely unusual. It is quite distinct from the usual 'threshold anomaly', which can be explained in terms of causality, and can be calculated using a dispersion relation connecting the real and imaginary potentials. Before analysing it in terms of a DPP it is necessary first to establish whether this anomalous feature in

the energy dependence of the optical potential $W(E,r)$ is due to some coupled reaction channels which have not been explicitly included in the CRC analysis (e.g., a channel which has a small cross-section yet makes a large contribution to the local potential), or whether the anomaly is actually an example of 'spurious' energy dependence (i.e., is due to the fact that the analysis uses only local l-independent potentials, whereas the 'true' potentials are almost certainly non-local and l-dependent).

Section 5.3 is an investigation of the accuracy of two analytic forms for the quadrupole Coulomb excitation imaginary DPP, and a comparison of these forms with the coupled-channel quadrupole DPP (calculated using only the excitation to the 2^+ state of the target nucleus to obtain an elastic S-matrix and then inverting this S-matrix to obtain a local potential).

Section 5.4 applies the 'CRC+inversion' method to investigate the fusion of ^{16}O+^{62}Ni at the Coulomb threshold. This method of analysis is particularly useful when applied to heavy-ion fusion at the Coulomb threshold, since there is strong coupling of the fusion process to direct reaction channels such as nucleon transfer, which cannot be adequately modelled by the usual barrier penetration model (BPM) for fusion. The 'extended optical model' (EOM) for fusion is further extended using 'CRC+inversion', and the behaviour of the partial wave fusion cross-sections are also investigated, as they supply useful physical constraints on the fusion potentials.

Section 5.5 investigates the difference between the one-nucleon transfer DPP for ^{16}O+^{62}Ni at 42 MeV when the excited states in the transfer partitions are either included or excluded. Section 5.6 investigates the additivity of the one-nucleon transfer

DPPs (excluding the excitation states in the transfer partition).

Finally, the investigations presented in this entire thesis are summarised and reviewed in Section 6.

5.2 Preliminary investigations: dispersion relation analysis of the anomalous peak in $W(E)$

Imposing the requirement of causality upon the scattering wavefunction (i.e., that no scattered wave can be emitted from the target before the incident wave reaches it) leads to the following dispersion relation between the energy dependencies of the real and imaginary potentials at a given radial value:

$$\Delta V(E) = \frac{P}{\pi} \int_{-\infty}^{+\infty} \frac{W(E')}{E' - E} dE' \tag{5.1}$$

where P refers to the Cauchy principal value of the improper integral.

The opening of the non-elastic channels at the Coulomb energy threshold leads to a sudden increase in the strength of the absorptive imaginary potential. The imaginary part $W(E)$ shows a sudden increase to a maximum value, followed by a plateau for higher values of energy due to saturation. This, via the dispersion relation, gives rise to a bell-shaped peak in the energy-dependent addition $\Delta V(E)$ to the real part centred approximately around the Coulomb barrier energy. This peak is often still referred to as the 'threshold anomaly', although it is now fully understood on the basis of the

dispersion relation. It can be interpreted as an attractive addition to the real potential due to virtual excitations.

Keeley *et al.* [47] present an unusual anomalous behaviour in $W(E)$ which has nothing directly to do with the dispersion relation. During their optical model fitting of ^{16}O+^{A}Ni scattering over a range of energies covering the Coulomb threshold, they obtain a shape for $W(E)$ (defined at the strong absorption radius, $r = 10$ fm) which is peaked at the Coulomb threshold, dips to a minimum value and then has a linear increase for large E. This shape for $W(E)$ was consistently obtained for all values of A examined ($A = 58, 60, 62$, and 64). We examined the case when $A = 62$ because it exhibits the effect most clearly [48]. Keeley *et al.* claimed in their original paper [47] that such a peak in $W(E)$ had not been observed before in these type of systems; however, Keeley and Rusek [50] later presented another example with ^{7}Li+^{208}Pb elastic scattering, and there appears to be another with ^{16}O+^{63}Cu in a paper by Pereira *et al.* [51]

In their original paper, Keeley *et al.* did not perform a dispersion relation analysis to try to relate their normalisation parameter $N_R(E)$ to $W(E)$, but attempted to discover which channels might be responsible for the anomalous peak in the absorption by doing coupled-channels calculations at three energies covering the Coulomb threshold for each A value. They concluded that they could not unambiguously identify the channel responsible for the peak, and suggested that it could be a compound nucleus effect.

If the peak in $W(E)$ really were part of its intrinsic energy dependence, it should

have an effect on their normalisation parameter $N_R(E)$ via the dispersion relation. It follows that a curve which fits the $W(E)$ 'data' points as closely as possible (i.e., fits the anomalous shape of W as a function of energy) should provide a very close fit to the $N_R(E)$ 'data' points. Specifically, the anomalous shape of $W(E)$ should give rise to a corresponding anomaly in the bell-shape of $N_R(E)$. Conversely, if a close fit to $W(E)$ gives an $N_R(E)$ which does not fit the 'data' points, then it may be concluded that the anomalous energy-dependence of the absorptive potential is an artefact of the optical model fitting procedure, or is a consequence of assuming locality, rather than being a physically meaningful feature of the potential.

In the following analysis, we apply the dispersion relation to the 'data points' of $N_R(E)$ and $W(E)$ given by Keeley *et al.* [47] to see how good a fit can be obtained, and whether the features in $W(E)$ can be directly related to features in $N_R(E)$ via the dispersion relation.

Since the anomaly in $W(E)$ cannot be fitted by the simple and widely used 'linear schematic model' (which consists of two straight lines), more complex curves had to be used and the corresponding $N_R(E)$ calculated by numerical integration. Two such curves were used, and a third was used to give a smooth approximate fit to $W(E)$ while eliminating the anomaly. These curves were:

1. A modified form of the model of Wang *et al.*

2. A 'gaussian+linear' model

3. A Fermi form factor (in which the anomaly is not present)

The results of our analysis of the relationship between $W(E)$ and $N_R(E)$, using these models for $W(E)$, are as follows:

The modified Wang model. The original Wang model is a non-linear schematic model for $W(E)$ at a given radial value. It is called 'schematic' as it can be analytically integrated. Wang *et al.* parameterise $W(E)$ as

$$W(E) = \frac{\alpha(E - E_F)^4}{(E - E_F)^4 + \beta^4}. \tag{5.2}$$

This functional form (and all other functional forms for $W(E)$ at a given radius presented here) applies at one particular radial value; in this case, the SAR, $r = 10$ fm. This gives a curve for $W(E)$ which is symmetric about $E = E_F$, and for $E > E_F$ has approximately the shape of a Fermi form factor, while having the advantage of an analytic solution when inserted into the dispersion relation. This analytic solution is given by the expression

$$\Delta V(E) = \frac{\alpha\beta(E - E_F)[(E - E_F)^2 + \beta^2]}{\sqrt{2}[(E - E_F)^4 + \beta^4]}. \tag{5.3}$$

However, as it stands this model cannot fit the anomaly in $W(E)$ found by Keeley *et al.*, so the model of Wang *et al.* was modified by adding a peak to it at the Coulomb threshold. This peak is created by subtracting from a Wang *et al.* curve another such curve which possesses a greater diffuseness parameter β. Collecting terms, this gives

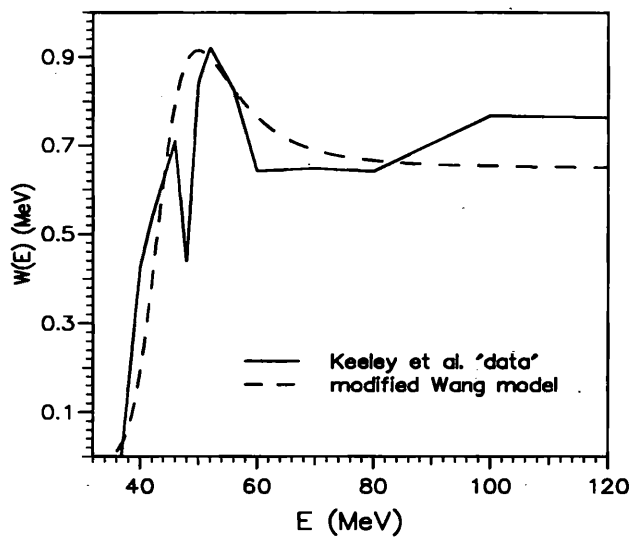

Figure 5.1: The fit of the modified Wang model to Keeley *et al.*'s $W(E)$

the following modification of the Wang model:

$$W(E) = \frac{(1+\gamma)\alpha(E-E_F)^4}{(E-E_F)^4+\beta_1^4} - \frac{\gamma\alpha(E-E_F)^4}{(E-E_F)^4+\beta_2^4}. \tag{5.4}$$

The advantage of this modified formula is that it captures the peak in $W(E)$ at the Coulomb barrier, but it misses the linear increase in absorption for large E. Fig. 5.1 shows the best fit to the $W(E)$ 'data' obtainable using the modified Wang model for $E > E_F$. The values of the parameters of the model are given in Table 5.1.

The corresponding 'threshold anomaly' in the real potential is given (up to an

Parameter	α	β_1	β_2	γ	E_F
Value	0.65	13.5	17.5	2.8	32

Table 5.1: Optimal values for the parameters of the modified model of Wang *et al.*. α is in units of MeV; all other parameters are dimensionless.

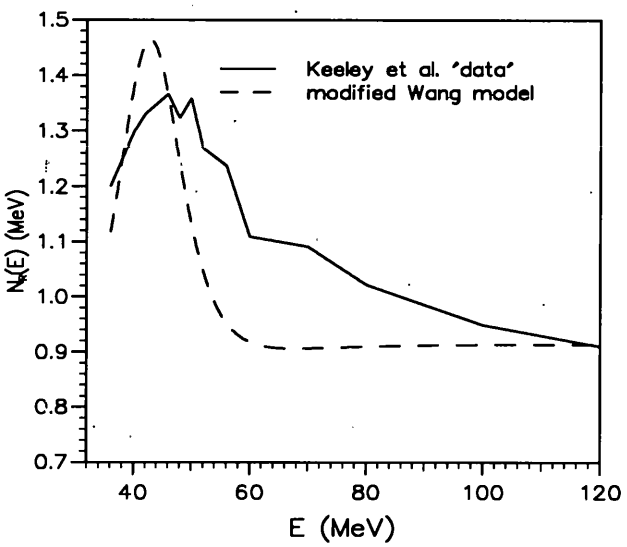

Figure 5.2: The fit of the modified Wang model to Keeley *et al.*'s $N_R(E)$

additive constant) by the analytic formula

$$\Delta V(E) = \frac{(1+\gamma)\alpha\beta_1(E-E_F)[(E-E_F)^2+\beta_1^2]}{\sqrt{2}[(E-E_F)^4+\beta_1^4]} - \frac{\gamma\alpha\beta_2(E-E_F)[(E-E_F)^2+\beta_2^2]}{\sqrt{2}[(E-E_F)^4+\beta_2^4]}. \tag{5.5}$$

This is the value of $\Delta V(E)$ at $r = 10$ fm, and the result must be suitably modified to correspond to the normalisation parameter $N_R(E)$. Fig. 5.2 shows the fit to $N_R(E)$ corresponding to the modified Wang *et al.* curve shown in Fig. 5.1.

It is clear that the shape of the curve for $N_R(E)$ is unsatisfactory; specifically, there is a rapid falloff in the curve for $E > 45$ so that it underestimates the 'data' points for large E. This problem could not be solved by altering the additive constant, since this does not broaden the peak in the curve, which is far too narrow to fit the 'data'.

The Wang model with cutoff. Applying the Wang model to a heavy-ion case, even in its modified form, is problematical; the reason for this is that, while it has a conveniently analytic form for ΔV, it is actually symmetric about $E = E_F$. If, as in this case, E_F is significantly larger than zero, it follows that the $W(E)$ calculated by this model will also be significantly larger than zero at energies well below the Coulomb barrier. This will tend to distort the shape of ΔV, since the integration in the dispersion relation is (in principle) over all energies from zero to infinity. The Wang model was initially proposed for the case of light ions, and may not be appropriate when applied in cases where $Z_p Z_t$ is large. To investigate whether the modified Wang model can be meaningfully applied to heavy ion scattering, the model would have to be modified still further by cutting off $W(E)$ at $E = E_F$, so that $W(E) = 0$ for $E < E_F$. This means of course that there is no longer an analytic form for ΔV, so that the curve for $N_R(E)$ was calculated by numerical integration. [1]

[1]The code written for the purpose by the present author was also applied in published work [49] which is not reported in this thesis.

The 'gaussian+linear' model. In order to obtain a more satisfactory fit to the anomaly in the energy-dependent absorption, a new model for $W(E)$ was devised. I wished to investigate the effect on $N_R(E)$ of including the linear increase in the absorption for large E as well as the peak at the Coulomb threshold; there seems to be no other model which can simultaneously fit both features. The energy domain was divided into two regions, one for energies less than the peak at the Coulomb barrier, the other for greater energies. The curve for the lower energies is a gaussian whose centre is close to the energy dividing the two regions, E_F. The curve for large energies consists of another (in general different) gaussian whose centre is at $E = E_F$, plus a straight line. The formula for this model is

$$W(E) = \begin{cases} \alpha \exp\{-(E - E'_F)^2/\beta_1^2\} & E < E_F \\ \gamma \exp\{-(E - E_F)^2/\beta_2^2\} + \lambda(E - E_F) + \mu & E \geq E_F. \end{cases} \tag{5.6}$$

There are six free parameters in this model: E_F, γ, β_1, β_2, λ and μ. The values of E'_F and α are calculated from the equations:

$$E'_F = E_F + \frac{\lambda\beta_1^2}{2(\gamma + \mu)} \tag{5.7}$$

$$\alpha = (\gamma + \mu) \exp\{-(E - E'_F)^2/\beta_1^2\}. \tag{5.8}$$

These values for E'_F and α ensure that the functions and their derivatives match at $E = E_F$. This avoids the unphysical characteristics of the linear schematic models, such as the infinite slope of ΔV at the end-points of the line segments, and thereby

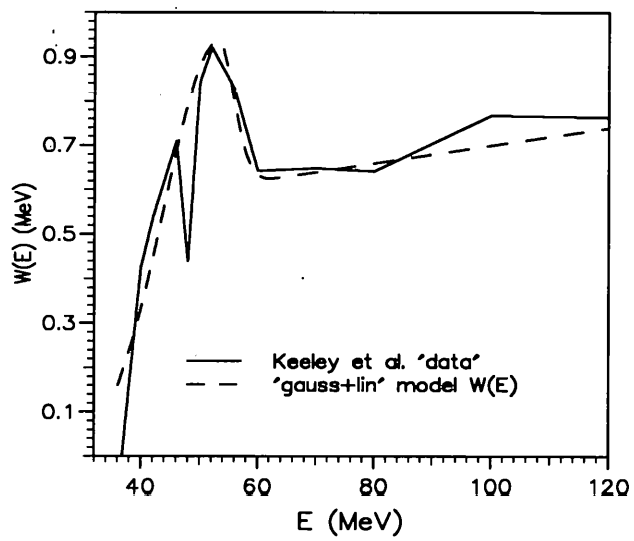

Figure 5.3: The fit of the 'gaussian+linear' model to Keeley *et al.*'s $W(E)$

ensures a more accurate determination of the shape of $N_R(E)$ implied by the shape of $W(E)$. Fig. 5.3 shows the best-fit 'gaussian+linear' model with a positive-slope linear term. To investigate the precise effect which the linear increase in absorption at large energy has upon $N_R(E)$, the model was used first with a positive-slope linear term to obtain the best possible fit to $W(E)$, and then with a zero-slope linear term to eliminate the increased absorption.

Parameter	E_F	β_1	β_2	γ	λ	μ	E'_F	α
Value	53	13.0	3.873	0.33	0.002	0.606	53.1806	0.936

Table 5.2: Optimal values for the parameters of the 'gaussian+linear' model for $W(E)$. α and γ are in units of MeV; all other parameters are dimensionless.

Fig. 5.4 displays the curve for $N_R(E)$ corresponding to the case where the linear

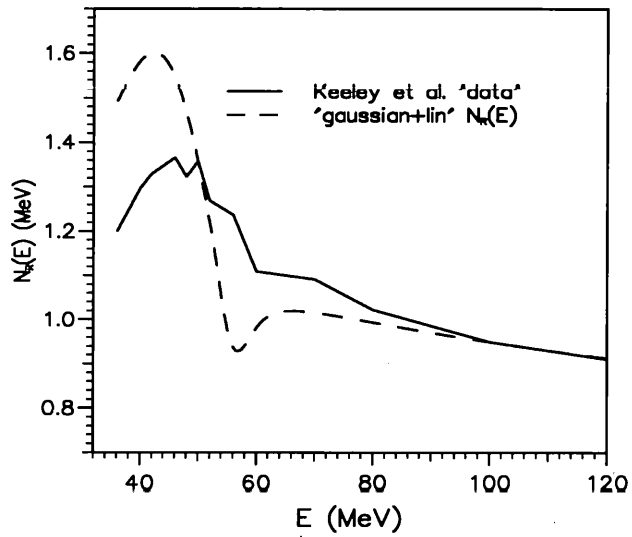

Figure 5.4: The fit of the 'gaussian+linear' model to Keeley *et al.*'s $N_R(E)$

term in our model has a positive slope; the values of the parameters are given in Table 5.2. As can be seen from Fig. 5.3, our model fits the $W(E)$ 'data' points supplied by Keeley *et al.* better than any of the other models employed in this analysis. The fit to $N_R(E)$ derived from the dispersion relation, however, is probably the worst. The shape of the curve for $N_R(E)$ is very unusual, and is worth commenting on. The peak between 30 and 55 MeV is followed by a dip in the curve between about 55 and 65 MeV and by a very broad peak of small magnitude which extends into the higher energy range.

Fig. 5.5 shows the fit of the 'gaussian+linear' model with a zero-slope linear term (i.e., $\lambda = 0$) to $N_R(E)$. The effect of omitting the linear increase is negligible as far as the shape of the fit to $N_R(E)$ is concerned. It is clear, furthermore, that the $N_R(E)$ 'data' points do not support the existence of a local minimum at any energy. It can

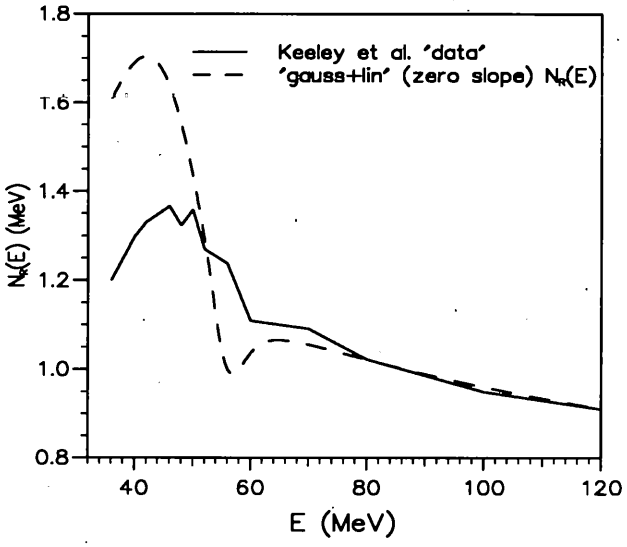

Figure 5.5: The fit of the 'gaussian+linear' model with zero slope to Keeley *et al.*'s $N_R(E)$

therefore be concluded that the local minimum in $W(E)$ between 55 and 65 MeV in both of the 'gaussian+linear' fits has no counterpart in the $N_R(E)$ 'data', contrary to what is required by the dispersion relation between the real and imaginary potentials.

Using a Fermi form factor. The Fermi form factor $W(E) = W_0/(1+\exp\{(E_w - E)/\Delta\})$ was given the parametric values shown in Table 5.3.

Parameter	W_0	E_w	Δ
Value	0.65	44	5

Table 5.3: Optimal values for the parameters of the Fermi form factor for $W(E)$. All the parameters are in units of MeV.

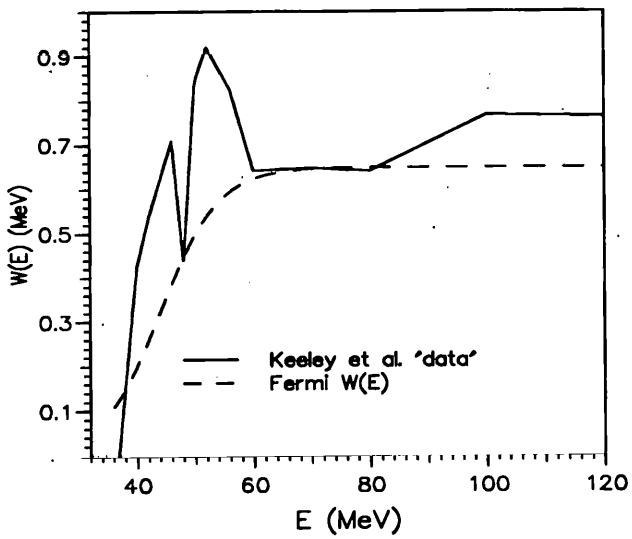

Figure 5.6: The fit of the Fermi form factor to Keeley *et al.*'s $W(E)$

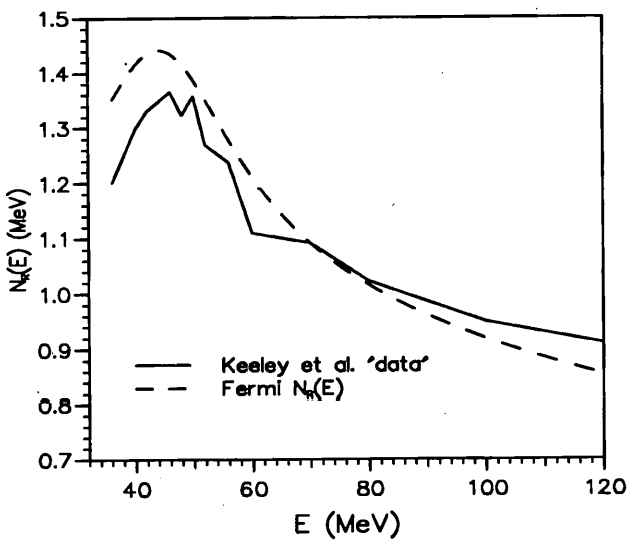

Figure 5.7: The fit of the Fermi form factor to Keeley *et al.*'s $N_R(E)$

As can be seen from Fig. 5.6, the Fermi form factor completely misses the anomalous peak in $W(E)$; however, the fit to the $N_R(E)$ 'data', shown in Fig. 5.7, is generally very good, apart from one datum. Given the bad fit to $N_R(E)$ obtained from any accurate model of the Keeley *et al.* 'data' $W(E)$, and the good fit of this Fermi model for $W(E)$, a model which completely omits both the anomalous peak and the linear increase for large E, it is clear that for this given 'data' there is no evidence from a dispersion relation analysis for any intrinsic anomalous energy dependence.

Keeley *et al.*'s later analysis. A later paper was published by Keeley *at al.* [52] which subjected the anomaly in $W(E)$ for the cases ^{16}O+^{58}Ni and ^{16}O+^{62}Ni to further analysis. A set of CRC calculations were performed, from which effective local polarization potentials were derived as an l-independent weighted mean of the trivially equivalent l-dependent polarization potentials. It was claimed that the anomalous peak in $W(E)$ at the surface was reproduced by their analysis, although with a much reduced magnitude, and was related to the coupling to the first 3^- state of ^{16}O. Insufficient time was available for us to investigate this claim using the IP inversion method.

However, the magnitude of the peak in $W(E)$ is less than half that of the empirical optical model potential in the case of ^{62}Ni, is narrower and is generally less pronounced as a feature. For all energies, the CRC-derived potential is outside the error bars of the optical model potential $W(E)$. Clearly, as Keeley *et al.* state, the calculations still lack a significant ingredient to be able to generate the observed behaviour and strength of the effective interaction. Their conclusion was that the discrepancy between

the empirical and CRC potentials is due to the direct or indirect effect of couplings to other channels not included in their calculations, particularly multi-step couplings. However, the magnitude, form, isotopic and energy dependence of these extra terms are largely unknown quantities, so it is not clear how they could be included in any rigorous way in an expanded CRC calculation.

The discrepancy could not be corrected by including other direct couplings to two-phonon states, two-nucleon transfer or the giant quadrupole resonance, so Keeley *et al.* attempted to simulate multi-step processes by adding a term to the potential describing the nuclear interaction in the non-elastic channels. They found that adding a purely real term improved the fit of the CRC-derived potentials to the empirical potentials, but the peak in $W(E)$ was still too narrow and unpronounced, especially in the case of ^{62}Ni, and the parameters of the extra potential term seem to be rather arbitrary, there being no indication of which particular multi-step processes are significant.

An interesting point made by Keeley *et al.* is that even though the large negative Q-value for ^{16}O(3^-) suppresses the population of that state near the Coulomb threshold to an almost unobservable level, they found that its contribution to the polarization potential is important even at this low energy.

Other observed anomalies in $W(E)$ at threshold. There are two such cases of which we are aware: one involving ^{7}Li+^{208}Pb [50], and one involving ^{16}O+^{63}Cu [51].

In the latter case, Pereira *et al.* obtained a data point in $W(E)$ at just above threshold in their optical model fitting which was about twice the magnitude of the

saturation plateau, and which could be interpreted as an anomalous peak in $W(E)$ similar to that found by Keeley *et al.* for $^{16}O+^{62}Ni$. However, it is almost certainly not useful to subject this case to further analysis, as only one data point is anomalous, and that has a χ^2 value of nearly 30, and no reliance can therefore be placed on it. In the former case, the anomalous peak is much better established, by the optical model analysis of Martel *et al.* [53, 54]. Keeley and Rusek [50] carried out CRC calculations and found that the $^{208}Pb(^7Li,^6Li)^{209}Pb$ transfer channel had an effective polarization potential which had the same peak in $W(E)$ at about the right energy.

Conclusions. A dispersion relation analysis is limited to an examination of the consistency of the potentials with causality. In any optical model analysis, especially of heavy ions, there may be ambiguity in both the real and imaginary potentials, due to such factors as model-dependence or fixed-geometry fitting, or other factors which may introduce spurious energy dependence into the fitted potentials. Therefore, any physical conclusions drawn from a dispersion relation analysis must be treated with caution as sharing the ambiguities of the potentials themselves.

While Keeley *et al.*'s later analysis [52] has demonstrated that a peak in $W(E)$ at about the right energy can be produced by the coupling to an inelastic channel, it cannot be said that the CRC-calculated peak corresponds to the peak obtained in their earlier optical model analysis [47] either in magnitude or shape. Furthermore, given the results of our dispersion relation analysis, the optical model peak cannot be causally consistent with the shape of the corresponding $N_R(E)$, and must therefore

either be an artefact of the fixed geometry of the double-folding real potential or some other factor causing spurious energy-dependence of the imaginary potential.

In conclusion, it has been shown by using the consistency tests of dispersion relation analysis that dynamic polarization potentials determined by optical model fitting are unreliable, and therefore investigations of DPPs using 'CRC+inversion' should not set too high a store on matching potentials obtained by optical model fitting.

5.3 An investigation of the accuracy of the LTS and BGKP analytic forms for the quadrupole Coulomb excitation imaginary DPP

Since the long-range part of the imaginary potential for the case of $^{16}O+^{62}Ni$ at 42 MeV was difficult to obtain by inversion (see Section 5.4), and this part of the DPP is due mainly to Coulomb excitation, I decided to use an analytic form for the quadrupole Coulomb excitation imaginary DPP as part of the Starting Reference Potential (SRP) for the IMAGO inversions from the CRC S-matrix. I examined and compared two analytic forms for this purpose — the Love, Terasawa and Satchler (LTS) [55] form, and the Baltz, Glendenning, Kauffmann and Pruess (BGKP) [56] form.

The Love, Terasawa and Satchler (LTS) analytic form. The LTS analytic form for a purely imaginary Coulomb excitation DPP is given by the equations:

$$W_{\rm DPP}^{\rm LTS}(r) = \begin{cases} -\left[1 - \frac{1}{7}\left(\frac{R_{\rm C}}{r}\right)^2 - \frac{1}{21}\left(\frac{R_{\rm C}}{r}\right)^4\right] K_{\rm C}(r)\frac{W_{\rm P}}{r^5}, & r \geq R_{\rm C} \\ -\frac{2}{3}K_{\rm C}\frac{W_{\rm P}r^4}{R_C^9}, & r < R_{\rm C} \end{cases} \tag{5.9}$$

where $R_{\rm C}$ is the Coulomb radius ($R_{\rm C} = 1.3\{A_1^{1/3} + A_2^{1/3}\}$ fm), the local energy approximation, LEA, correction factor $K_{\rm C}(r) = [1 - (Z_1 Z_2 e^2/rE_{\rm cm})]^{-1/2}$, and the strength

$$W_{\rm P} = 0.01676\frac{\mu Z_{\rm p}^2}{k}B(E2, 0^+ \rightarrow 2^+)g_2(\xi), \tag{5.10}$$

where $Z_{\rm p}$ is the charge on the projectile, and $g_2(\xi)$ is an adiabaticity correction factor ($\xi = \frac{1}{2}\eta E_\lambda/E_{\rm cm}$). The LEA correction factor $K_{\rm C}(r)$ accounts for the fact that the projectile moves more slowly near the target than the plane-wave estimate predicts because the repulsive Coulomb potential dominates at the radii where $W_{\rm DPP}^{\rm LTS}$ is significant. Since $K_{\rm C}(r)$ diverges at $r = R_d = Z_1 Z_2 e^2/E_{\rm cm}$, a cutoff is chosen such that $K_{\rm C}(r)$ is given by the expression above for $r \geq R_d/0.9$ and is replaced by $K_{\rm C}(R_d/0.9) = 3.16$ for $r < R_d/0.9$. The use of such a cutoff has little effect on the magnitude and shape of $W_{\rm DPP}^{\rm LTS}$, as LTS point out in their paper. The adiabaticity correction factor $g_2(\xi)$ embodies the dependence of the Coulomb excitation on the excitation energy E_λ, since $\xi = \frac{1}{2}\eta E_\lambda/E_{\rm cm}$.

The radial form of this analytic DPP is shown in Fig. 5.8. Note the non-physical cusp at $r = R_{\rm C}$; this turned out not to be serious, since it occurs in a radial region

where the LTS DPP is of the same magnitude as the rest of the imaginary potential; this has the effect of 'smoothing out' the cusp in the total potential.

The LTS DPP was compared with that obtained by inversion from a CC S-matrix involving only the Coulomb excitation to the 2^+ state of ^{62}Ni with the same B(E2) (0.0890 in units of $(eb)^2$). The inverted DPP will be referred to as $W_{\rm DPP}^{\rm inv}$, and the LTS DPP as $W_{\rm DPP}^{\rm LTS}$. The inversion from the CC S-matrix was very easy, and only five basis functions were needed to obtain a phase shift distance of $\sigma^2 = 0.00285$ in six iterations, starting from a zero SRP. Fig. 5.9 directly compares $W_{\rm DPP}^{\rm LTS}$ and $W_{\rm DPP}^{\rm inv}$ (here labelled 'LTS' and 'CC' for clarity). Fig. 5.10 shows the results of a notch test carried out between $W_{\rm DPP}^{\rm inv}$ and the CC $S(l)$ from which it was inverted. This shows very clearly the radial range at which the S-matrix is sensitive to the values of the potential; this range extends from about $r = 9.5$ fm to $r = 18$ fm. The maximum sensitivity is to the potential at 11 fm, with a sudden fall between 11 and 12 fm, followed by a long tail extending to 18 fm. The almost complete insensitivity of the S-matrix to the potential at $r < 9$ fm means that the apparent inconsistency between $W_{\rm DPP}^{\rm LTS}$ and $W_{\rm DPP}^{\rm inv}$ for $r < 10$ fm is not physically meaningful.

The Baltz, Glendenning, Kauffmann and Pruess (BGKP) analytic form. The fundamental approximation used by Love, Terasawa and Satchler [55] was to use plane waves for the intermediate state and ground state, with a classical correction being made for the Coulomb braking. Baltz *et al.* [56] have derived a more exact expression for the long-range Coulomb excitation DPP by using Coulomb-distorted

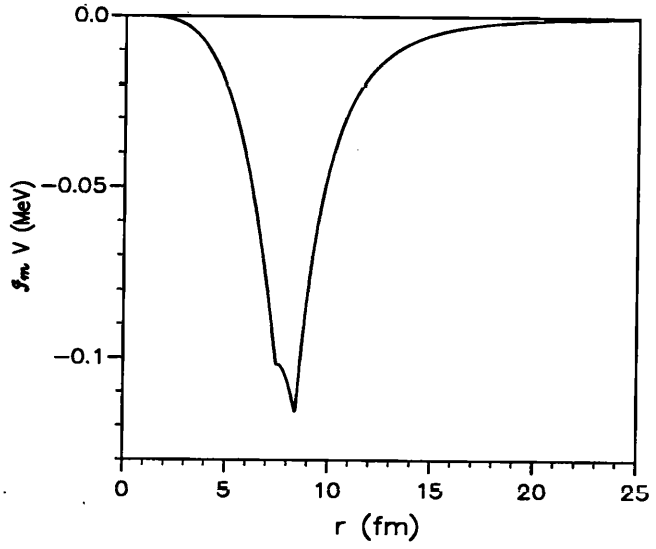

Figure 5.8: The Love-Terasawa-Satchler (LTS) quadrupole Coulomb excitation imaginary DPP for ^{16}O+^{62}Ni at $E_{\rm lab} = 42$ MeV.

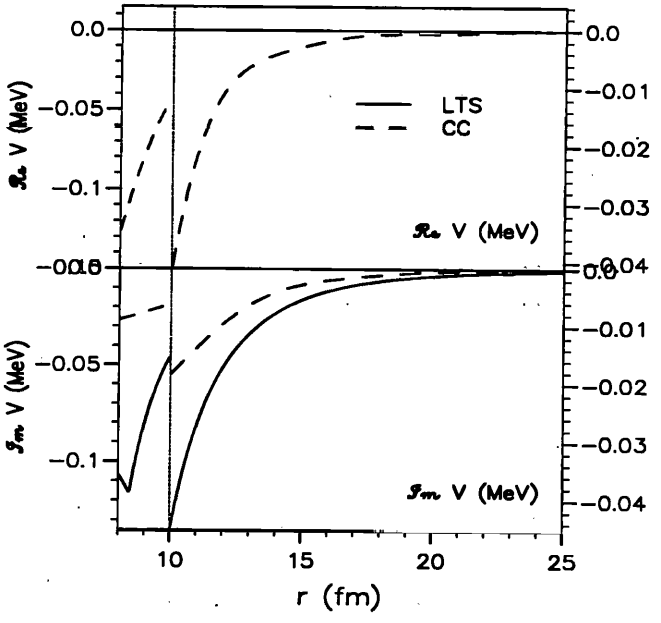

Figure 5.9: Comparison between the LTS DPP and the DPP obtained by inversion from a CC $S(l)$ including only quadrupole Coulomb excitation.

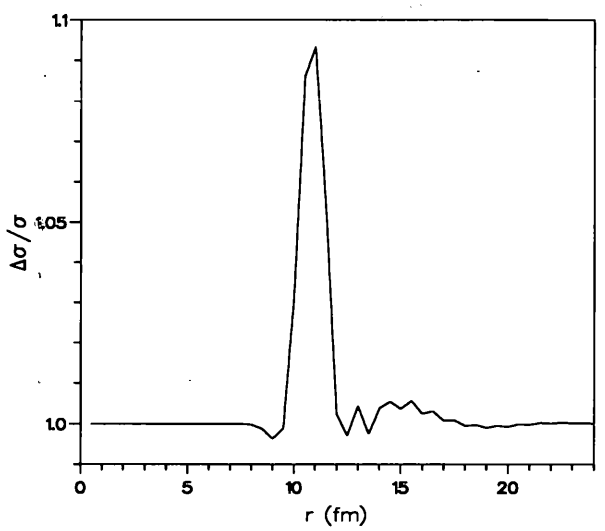

Figure 5.10: Results of a notch test between $W_{\rm DPP}^{\rm inv}$ and the corresponding CC $S(l)$.

scattering states and a Coulomb-distorted Green function; the result shows some interesting differences from the LTS potential.

The BGKP l-dependent quadrupole Coulomb excitation imaginary DPP is given by the expression:

$$W_{DPP}^{BGKP}(r,\hat{l}) = -\frac{i2\mu}{k\hbar^2}\frac{\pi}{50}Z_{\rm P}^2e^2B(E2,0^+\rightarrow 2^+)g_2(\xi) \qquad (5.11)$$
$$\times \left[\left(\frac{\eta^2k^2(3\hat{l}^2+\eta^2)}{\hat{l}^2(\hat{l}^2+\eta^2)^2}-\frac{\eta k^2}{\hat{l}^3}\arctan\frac{\hat{l}}{\eta}\right)\frac{1}{r^3}+\frac{4\eta k\hat{l}^2}{(\hat{l}^2+\eta^2)^2}\frac{1}{r^4}+\frac{2\hat{l}^4}{(\hat{l}^2+\eta^2)^2}\frac{1}{r^5}\right]$$

where μ is the reduced mass of the system, $Z_{\rm P}$ is the projectile charge, k is the wave number, $\hat{l}$ is the semiclassical $l+\frac{1}{2}$, and η is the usual Sommerfeld parameter.

This potential at first sight seems quite different from the LTS potential. It is explicitly l-dependent with $1/r^5$, $1/r^4$, and $1/r^3$ radially dependent terms in contrast to

the l-independent dominantly $1/r^5$ LTS behaviour. As $l \to \infty$, the $1/r^5$ term dominates in the BGKP potential, and the ratio of the LTS to the BGKP approaches 4/3.

It is not very convenient to use an l-dependent potential. We can obtain an l-independent equivalent to the l-dependent BGKP potential by first calculating the phase shifts associated with the BGKP potential, and then inverting those phase shifts using the code IMAGO in order to obtain a local, l-independent potential which has the same associated S-matrix as the BGKP potential. We shall refer to this inverted l-independent equivalent to the BGKP potential as $U_{\rm inv}^{BGKP}$. The l-independent S-matrix-equivalent potential of an l-dependent purely imaginary potential will in general have a (small) real component, and in the present case we allow for this by writing $U_{\rm inv}^{BGKP}(r) = V_{\rm inv}^{BGKP}(r) + iW_{\rm inv}^{BGKP}(r)$.

The BGKP phase shifts can be calculated by means of a perturbative JWKB integral which is evaluated along the Coulomb trajectory:

$$\delta_{DPP}^{BGKP}(\hat{l}) \sim -\frac{1}{2E_{\rm cm}} \int_0^\infty W_{DPP}^{BGKP}(\frac{1}{k}(\eta + (\hat{l}^2 + \eta^2 + \rho^2)^{1/2}), \hat{l}) \left(1 + \frac{\eta}{(\hat{l}^2 + \eta^2 + \rho^2)^{1/2}}\right) \mathrm{d}\rho, \tag{5.12}$$

where k is the wavenumber, η is the Sommerfeld parameter and ρ is the radial parameter for the Coulomb trajectory along which the integral is calculated. This is related to the usual internuclear radial parameter by the equation $r = \frac{1}{k}(\eta + (\hat{l}^2 + \eta^2 + \rho^2)^{1/2})$. When $\rho = 0$, r is the classical turning point. The integral is really only meaningful for values of $\hat{l}$ greater than the critical angular momentum for strong absorption (i.e., those $\hat{l}$ for which $|S(\hat{l})|^2 > \frac{1}{2}$).

Since the BGKP l-dependent potential is purely imaginary, the phase shifts (as calculated using Eq. 5.12) will likewise be purely imaginary. As the S-matrix is $S(\hat{l}) \equiv \exp[2i\delta(\hat{l})]$, its argument will be zero for all $\hat{l}$. Because the real part of the potential influences only the argument of the S-matrix, and the imaginary part only the modulus (to first order in the Born approximation), the real part of the l-independent $U_{\rm inv}^{BGKP}$ is expected to be negligible (although not zero, due to higher-order terms). This reinforces the point that only the imaginary part $W_{\rm inv}^{BGKP}$ is important for investigating the long-range behaviour of the DPP due to quadrupole Coulomb excitation.

The l-dependent BGKP Coulomb excitation tail and its associated S-matrix were calculated for the case of ^{16}O+^{62}Ni at 42 MeV, and the l-independent potential which gives the same S-matrix elements was obtained by inversion using IMAGO. The inverted potential is shown in Fig. 5.11, together with the LTS Coulomb excitation DPP and the potential inverted from the CC quadrupole Coulomb excitation S-matrix. The BGKP S-matrix is shown in the subsequent figure, also compared with the LTS and CC S-matrix elements. An inversion from the BGKP S-matrix was also carried out with the constraint that the real part of the potential be zero. The quality of the fit to the S-matrix was only marginally improved, and it can be seen from Fig. 5.11 that the real part of the unconstrained BGKP inverted potential is negligible when compared both to its imaginary part and the real part of the inverted CC potential.

The l-independent $W_{\rm inv}^{BGKP}(r)$, as Fig. 5.13 shows, is deeper than the $l = 0$ BGKP for $r < 9$fm, falls within the limits of the $l = 0$ and $l \to \infty$ BGKP potentials $W_{\rm DPP}^{BGKP}(r, \hat{l})$ between about $r = 9$ fm and 15 fm, and converges onto the $l \to \infty$ BGKP

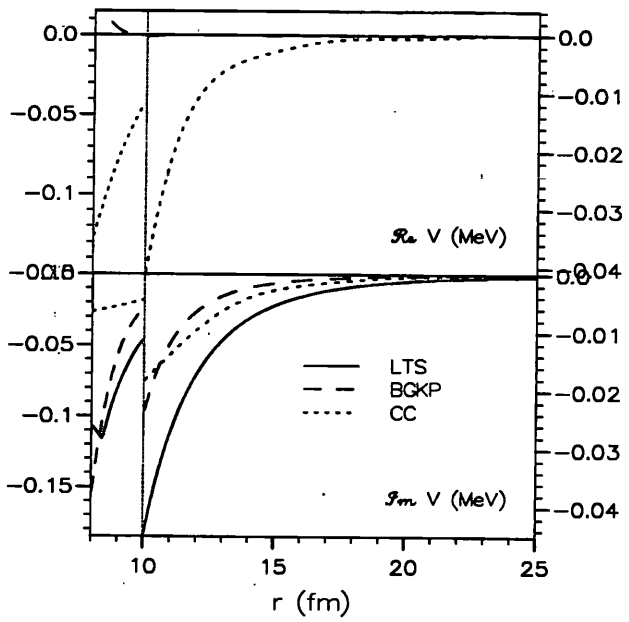

Figure 5.11: Comparison between the LTS, BGKP and CC quadrupole Coulomb excitation DPPs for $^{16}O+^{62}Ni$ at $E_{lab} = 42$ MeV. The real part of the LTS and BGKP DPPs are almost indistinguishable from zero.

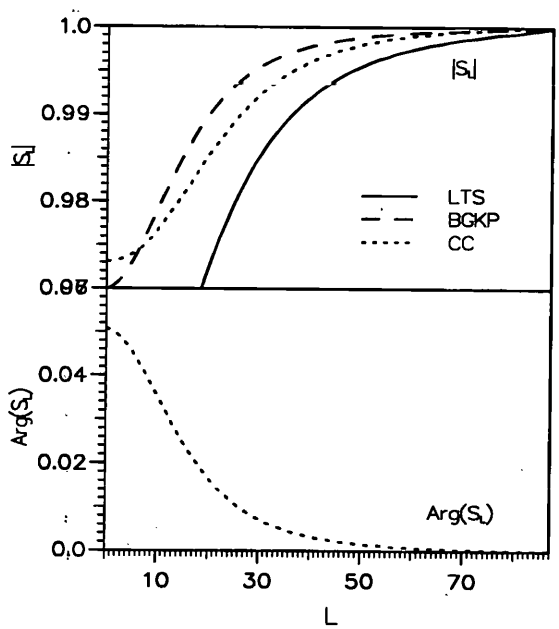

Figure 5.12: Comparison between the S-matrices for the LTS, BGKP and CC quadrupole Coulomb excitation DPPs.

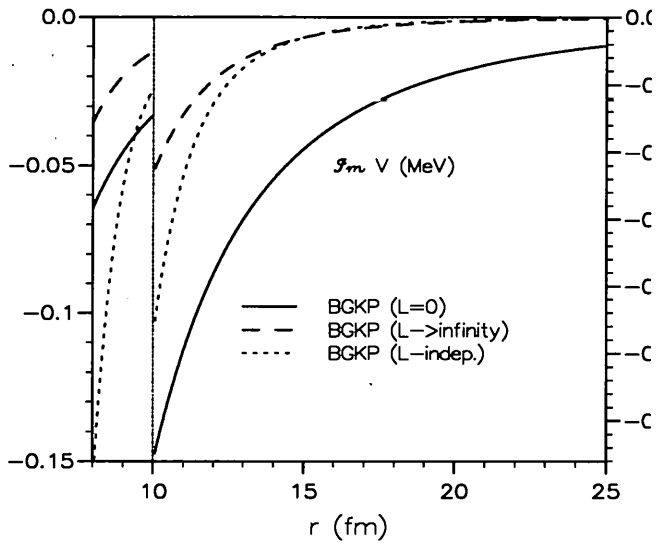

Figure 5.13: Comparison between the BGKP l-dependent potential at $l = 0$ and $l \to \infty$, and the inverted BGKP l-independent potential.

in the far surface. It therefore cannot be thought of as being in any simple sense an 'average' over l of the BGKP l-dependent potential.

Fig. 5.12 shows the S-matrix of the BGKP Coulomb excitation DPP, as calculated for the case of $^{16}O+^{62}Ni$ at 42 MeV, compared with a coupled channel (CC) calculation using the code FRESCO in which only the Coulomb excitation channel to the 2^+ target state was included, and with the LTS S-matrix. It is clear that the LTS model for the Coulomb excitation has greater absorption than either of the others, even in the far surface. The BGKP and CC DPPs have similar absorption in the far surface, but between $l = 10$ and $l = 60$ the CC shows greater absorption than the BGKP. The CC S-matrix differs from the other two by having a non-zero argument.

Conclusions. Since the main purpose of this part of the investigation is to provide an appropriate starting reference potential (SRP) for $S(l) \rightarrow V(r)$ inversions where the high l-range of the S-matrix is difficult to fit with a smooth potential in the far surface, the pragmatic criterion of ease of use as well as closeness to the CC Coulomb excitation DPP will apply. It is clear that the LTS DPP would be the simplest to apply, since it does not itself require inversion to obtain an l-independent potential. The BGKP DPP requires inversion to produce an l-independent form appropriate for my purposes, and the CC DPP requires both coupled-channels calculations and $S(l) \rightarrow V(r)$ inversion. However, it is also clear that the BGKP model agrees much more closely with the CC quadrupole Coulomb excitation DPP than does the LTS model. This is especially important when the inversion is from an S-matrix obtained by coupled channels calculations.

These results are also interesting in their own right, since the BGKP has been shown here to agree more closely with the Coulomb excitation DPP obtained by 'CC and inversion' than does the LTS DPP. This is to be expected, since the LTS model uses plane waves for the intermediate and ground states with a classical correction for the Coulomb braking. If what is desired is a Coulomb excitation DPP consistent with what can be obtained (by accurate inversion) from the S-matrix elements for a coupled-channels calculation, then this simplification is not appropriate, at least for heavy-ion scattering. The BGKP model's use of Coulomb-distorted scattering states and a Coulomb-distorted Green function seems to be more consistent with CC results.

5.4 Application of the 'CRC+inversion' method to the extended optical model calculation of partial fusion cross-sections

Introduction. The fusion of two heavy ions at bombarding energies near the classical Coulomb barrier has usually been modelled using the one-channel barrier penetration model (BPM), in which fusion is assumed to take place only if the two ions go over or tunnel through the real potential barrier formed from the sum of the Coulomb and nuclear potentials. The purpose of this investigation is to test the applicability of an alternative method, the extended optical model (EOM), using local l-independent potentials obtained by inversion from the elastic scattering cross-section. This will be a test both of the EOM method and of the local inverse potentials themselves (which exclude non-elastic channels) for their usefulness in an investigation into heavy ion fusion cross-sections and spin distributions.

In the BPM, for a given partial wave l, the nucleus-nucleus potential can be written as

$$V_l(r) = V_{\mathrm{Cou}}(r) + V_{\mathrm{nuc}}(r) + V_{\mathrm{cfg}}(r) \tag{5.13}$$

where $V_{\mathrm{Cou}}(r)$ is the standard Coulomb potential for nuclei (see Chapter 2.1 of this thesis), $V_{\mathrm{nuc}}(r)$ is the specifically nuclear part of the interaction and $V_{\mathrm{cfg}}(r) = \hbar^2 l(l+1)/2\mu r^2$ is the so-called 'centrifugal' potential. The total potential $V_l(r)$ has an outer maximum at a radial region where the long-range Coulomb and the short-range nuclear

parts of the potential are of comparable magnitude. At slightly smaller radial separations, there is an attractive well which traps the nuclei sufficiently long enough for fusion to occur. The centrifugal potential increases the barrier height and slightly shifts the radial position of the barrier. It can eliminate the attractive well, and generally supresses fusion at larger impact parameters.

The transmission coefficients for passage over or through the barrier near the Coulomb threshold can be calculated using the WKB method, so that [57]:

$$T_l(E) = [1 + \exp(2K_l(E))]^{-1} \tag{5.14}$$

where

$$K_l(E) = \mp \int_{r_a}^{r_b} (\frac{2\mu}{\hbar^2}|V_l(E) - E|)^{1/2} dr, \tag{5.15}$$

in which r_a and r_b are the inner and outer turning points of the fusion barrier, and the minus/plus signs before the integral refer to above-/below-barrier energies.

The partial wave fusion cross-sections can then be written in terms of the transmission coefficients as:

$$\sigma_l(E) = \pi\lambda\!\!\!^{-2}(2l + 1)T_l(E) \tag{5.16}$$

where $\lambda\!\!\!^{-}$ is $1/k$. The cross-section for complete fusion is the sum over all partial waves, $\sigma_{\rm F}(E) = \sum_l \sigma_l(E)$. The spin distribution, $\sigma_l(E)$, is the contribution of that partial wave to the total fusion cross-section.

The moments of the spin distribution are of great importance: the zeroth moment

is the total fusion cross-section at a given energy, $\sigma_{\rm F}(E) = \sum_l l^0 \sigma_l(E)$, while the first and second moments give the mean l-value and the mean square l-value of the spin distribution: $< l >_{\rm F} = \sum_l l\sigma_l(E) / \sum_l \sigma_l(E)$, and likewise for $< l^2 >_{\rm F}$. These higher moments of $\sigma_l(E)$ provide additional constraints on theoretical models for sub-barrier fusion.

The shape of $\sigma_l(E)$ is also significant. Classically, in the barrier penetration model near the Coulomb barrier, all partial waves up to some maximum l-value $l_{\rm cr}$ contribute only to fusion, while the grazing partial waves contribute only to direct reactions. This would mean that $T_l = 1$ for all $l \leq l_{\rm cr}$ and $T_l = 0$ for all $l > l_{\rm cr}$, so that $\sigma_l(E) = \pi\lambda\!\!\!^{-2}(2l+1)$ up to $l = l_{\rm cr}$ and $\sigma_l(E) = 0$ for all higher l-values. It would follow that $\sigma_{\rm F}(E) = \pi\lambda\!\!\!^{-2} \sum_0^{l_{\rm cr}} (2l+1) = \pi\lambda\!\!\!^{-2}(l_{\rm cr}+1)^2$. In fact, the transmission coefficients undergo a smooth transition from unity to zero, due to the effect of quantum tunnelling through the barrier. Consequently, the sharp cut-off at $l_{\rm cr}$ in the spin distribution will be replaced by a smooth cut-off near $l_{\rm cr}$.

At lower energies, this simple modification to the classical shape for $\sigma_l(E)$ is not sufficient. As the bombarding energy decreases towards the barrier, the centrifugal potential is less effective in suppressing fusion for higher partial waves, and the effect of the coupling of other channels to the fusion is to broaden the spin distribution [58, 59]. It is a consequence of such a broadening of $\sigma_l(E)$ due to channel coupling effects that the spin distribution can provide information about the dynamics of the fusion itself. This can provide additional constraints on the modelling of the fusion process.

The heavy-ion sub-barrier fusion anomaly. In the first measurements of the sub-barrier fusion of two heavy ions [60, 61], it was found that, at energies at or below the classical Coulomb barrier, the cross-sections for fusion were several orders of magnitude greater than what was predicted by the barrier penetration model, in which one-channel quantum tunnelling is solely responsible for the fusion. It was also discovered [60] that the cross-sections for sub-barrier fusion depended sensitively on the atomic number of the nuclei involved, especially for nuclei near a closed shell.

There are several possible explanations for the enhanced fusion cross-section at and below the Coulomb barrier. The shortcomings of the one-dimensional BPM suggest that sub-barrier fusion is strongly coupled to other degrees of freedom. The possibilities which have been investigated include: (i) shape effects of the colliding nuclei. For example, nuclei with static quadrupole deformations have an important degree of freedom in the orientation angle between the nuclear axis of symmetry and the line of centres of the two nuclei [61, 62]. (ii) zero point vibrational motions of the nuclear surfaces may be an important degree of freedom coupled to fusion [63, 64]. (iii) other collective modes of the nuclei, such as neck formation, may also be significant in enhancing sub-barrier fusion [65, 66]. (iv) transfer reaction involving one or more particles may be coupled strongly to the fusion channel, and this can enhance the fusion cross-section [67, 68].

The existence of strong coupling of the fusion process to direct reaction channels implies that the heavy ions involved are too complex in structure to be adequately modelled as rigid spheres, as in the BPM. For heavy ion fusion, it is necessary to

consider how the nuclei can vibrate, or engage in other collective or inelastic excitations, and exchange particles as they undergo the fusion process.

Methods of analysis. Several methods of analysis have been used to investigate the effect of such channel coupling on the fusion cross-section:

- The extended optical model, employing a phenomenological potential whose real part represents the Coulomb barrier and part of whose imaginary potential is used to represent the flux that goes into the fusion channel. Usually, the phenomenological potential which fits the elastic scattering data is used [69].

- Coupled reaction channels calculations (CRC) are used to explicitly include the effects of the strongly coupled channels. In this CRC procedure, a short-ranged imaginary potential is used, which will not suppress the coupling during the barrier penetration phase of the fusion process [70].

- Feynman path integrals have been employed to model the multi-dimensional quantum tunnelling which is involved [71, 72, 73].

- Static deformation or zero-point motion has been investigated using the one-dimensional BPM, but averaging over the intersurface orientations or distances respectively.

- Model the collective phenomena such as neutron flow or neck formation [74, 75].

- The time-dependent wave packet method [76], in which the wave packet is in many degrees of freedom of the fusing system.

Here, I shall use the extended optical model (EOM), together with coupled reaction channels (CRC) calculations.

The extended optical model analysis. The simplest expression for the fusion cross-section within the one-channel optical model is that employed by Udagawa *et al.* [69], involving the inner part of the absorptive potential:

$$\sigma_{\rm F} = \frac{2}{\hbar v}\int_0^{R_{\rm F}} W(r)|\chi(r)|^2 dr, \tag{5.17}$$

where $W(r)$ is the imaginary part of the optical potential obtained by fitting the elastic differential cross-section, $\chi(r)$ is the wavefunction calculated from that potential, and $R_{\rm F}$ is the cut off radius which separates the inner part of the absorptive potential (assumed to be associated with fusion) from the peripheral part (assumed to be associated with flux into the direct reaction channels). In Udagawa *et al.*'s analyses [69, 77], $R_{\rm F} \sim 1.4(A_1^{1/3} + A_2^{1/3})$.

The major problem with this model is that the value of the cut-off radius $R_{\rm F}$ is rather arbitrary (although Udagawa *et al.* found it not to change much over a wide range of isotopes and energies), and is an artifact of the model rather than representing a physical feature. The value of $R_{\rm F}$ is anomalously high, and seems to imply that fusion is taking place on or even beyond the Coulomb barrier rather than solely inside it.

A somewhat more physically meaningful expression can be obtained by writing the absorptive potential as a sum of two terms, one of which represents flux lost to

fusion and the other the flux lost to direct reactions which do not lead to fusion:

$$W(r) = W_{\rm F}(r) + W_{\rm D}(r) \tag{5.18}$$

The fusion cross-section is:

$$\sigma_{\rm F} = \frac{2}{\hbar v} \int W_{\rm F}(r) |\chi(\mathbf{r})|^2 \mathrm{d}\mathbf{r}, \tag{5.19}$$

where the integration is now over all $\mathbf{r}$, and $\chi(\mathbf{r})$ is the total scattering wavefunction. There is no sharp radial cut-off between $W_{\rm F}(r)$ and $W_{\rm D}(r)$; they may overlap to some extent. This separation of the imaginary potential into two terms, one responsible for fusion and the other for direct reactions not leading to fusion, is called the 'extended optical model' (EOM).

Eq. 5.19 can be used, at least in principle, to determine the magnitude and form of $W_{\rm F}(r)$; that is, what proportion of the phenomenological imaginary potential is actually responsible for fusion. Since $\sigma_{\rm F}$ can be measured experimentally and $\chi(r)$ is determined by the phenomenological elastic scattering potential, the 'fusion potential' $W_{\rm F}(r)$ can be parametrized and the values of those parameters found by fitting $\sigma_{\rm F}$, if it has been measured. However, the problem with this is that $W_{\rm F}(r)$ has at least three parameters, so that a unique fit to $\sigma_{\rm F}$ is not possible [77]. Additional experimental constraints are needed, one of which is given by the spin distribution of the fusion cross-section, $\sigma_{\rm F}(l)$, which can be measured [78].

For spin-zero nuclei, the spin of the compound nucleus is the orbital angular

momentum in the entrance channel and a partial wave decomposition of $\chi(r)$ can be used in Eq. 5.19, so that $\sigma_{\rm F}$ may be decomposed into partial fusion cross-sections $\sigma_{\rm F}(l)$:

$$\sigma_{\rm F}(l) = \frac{8}{\hbar v k^2}(2l+1)\int_0^\infty W_{\rm F}(r)|\chi_l(r)|^2 {\rm d}r. \tag{5.20}$$

The extended optical model has been used to study sub-barrier fusion for heavy ions by Satchler *et al.* [79, 80] among others. Satchler *et al.* [80] improved upon the Udagawa sharp cut-off model by making a further decomposition of the imaginary potential by dividing the fusion potential itself into two parts — a volume component with a small radius, and a surface-peaked component having the same radial shape as $W_{\rm D}(r)$, differing only in its absolute magnitude:

$$W_{\rm F}(r) = W_{\rm OF}(r) + W_{\rm PF}(r), \tag{5.21}$$

so that the total surface-peaked potential is $W_{\rm S} = W_{\rm PF} + W_{\rm D}$ and the total imaginary potential is $W = W_{\rm OF} + W_{\rm PF} + W_{\rm D}$. Since $W_{\rm PF}$ is directly proportional to $W_{\rm D}$, then $W_{\rm PF}$ is some proportion of $W_{\rm S}$, so that

$$W_{\rm PF}(r) = \xi W_{\rm S}(r) \tag{5.22}$$

$$W_{\rm D}(r) = (1-\xi) W_{\rm S}(r) \tag{5.23}$$

where ξ is a constant to be determined by fitting the experimental $\sigma_{\rm F}$.

The main difference between Satchler *et al.*'s analysis and that of Udagawa *et al.*

is that the latter had effectively assumed that the addition of the surface-peaked term to the fusion potential, due to the effects of coupling to the direct reaction channels, could be accommodated into the Woods-Saxon shape of their $W_{\rm F}$ by simply increasing the radial cut-off parameter, while Satchler *et al.* had further decomposed $W_{\rm F}$ into a volume term and a surface term having the same shape as $W_{\rm D}$. This allowed them to obtain fits to $\sigma_{\rm F}$ which are equally as good as those of Udagawa *et al.*.

However, the main disadvantage of the analysis of Satchler *et al.* is that their potentials (both 'A1', which does not take long-range Coulomb absorption into account, and 'A2', which does) fail to fit the shape of the experimental partial fusion cross-sections, $\sigma_{\rm F}(l)$. The volume term and the surface-peaked term give separate peaks in $\sigma_{\rm F}(l)$, which are not observed experimentally, and the calculated tails at large l-values are too long. Satchler *et al.* speculate that these discrepancies may be due to the fact that the surface-peaked part of the fusion potential is assumed to have the same shape as $W_{\rm D}$, in order to reduce the number of parameters used in the analysis, whereas $W_{\rm PF}$ may be expected to have a radial shape intermediate between $W_{\rm OF}$ and $W_{\rm D}$.

These problems may be avoided by Kubo *et al.* [81], in their extended optical model analysis. They divide the imaginary part of the phenomenological optical potential into four terms:

$$W(r) = W_{\rm OF}(r) + W^{\rm inel}_{\rm DPP}(r) + W^{\rm 1NT}_{\rm DPP}(r) + W^{\rm 4NT}_{\rm DPP}(r), \qquad (5.24)$$

where $W_{\rm OF}$ is the bare potential (as used in a coupled channels calculation), and

the three further terms are the corrections to that bare potential due to coupling to inelastic, one-nucleon transfer and four-nucleon transfer respectively. These dynamic polarization potentials (DPPs) were calculated using the method outlined in Kubo *et al.*'s paper [81]. The absolute magnitudes of the three DPPs were chosen by requiring that the total potential give the measured value of the total absorption cross-section, it being assumed that all three DPP terms require the same normalizing factor. Since the three DPPs are surface-peaked and represent the effect of couplings to inelastic and direct reactions, they are equivalent to the term $W_{\rm S}$ in Eq. 5.22 (where $W_{\rm S} = W_{\rm D} + W_{\rm PF}$). The bare potential is the volume term of the fusion potential. The total fusion potential is therefore given by $W_{\rm OF}$ together with the fraction ξ of the three DPPs that leads to fusion:

$$W_{\rm F}(r) = W_{\rm OF}(r) + \xi\{W^{\rm inel}_{\rm DPP}(r) + W^{\rm 1NT}_{\rm DPP}(r) + W^{\rm 4NT}_{\rm DPP}(r)\}, \qquad (5.25)$$

where the constant ξ is fixed by ensuring that the calculated value of $\sigma_{\rm F}$ is the same as the experimental value. The fusion cross-section can be written as $\sigma_{\rm F} = \sigma_{\rm OF} + \sigma^{\rm inel}_{\rm F} + \sigma^{\rm 1NT}_{\rm F} + \sigma^{\rm 4NT}_{\rm F}$, where $\sigma_{\rm OF}$ is calculated from $W_{\rm OF}$ alone.

Applying the 'CRC+inversion' method to the extended optical model. My analysis will involve dividing up the fusion potential following Kubo *et al.* [81], but using IP inversion on the CRC-calculated S-matrices to obtain the radial forms and magnitudes of the DPP terms in $W_{\rm F}$.

A major limitation of the extended optical model analyses so far described is that

they require *a priori* assumptions concerning the radial shape of the fusion potential and its components, in order to limit the number of free parameters. Furthermore, Kubo *et al.*, for example, assume that each DPP term in the potential makes the same proportional contribution to the fusion potential (parametrized as the constant ξ). This assumption is probably not accurate, as I found in my own analysis.

The DPPs which contribute to fusion are expected to be peripheral, and to fall within the sensitive radial range for elastic scattering. This is precisely the radial range within which an inverted potential can be expected to be well-defined; hence, the iterative-perturbative inversion method can be applied to this problem to investigate the actual radial shape and magnitude of the DPPs which contribute significantly to the sub-barrier fusion.

The case I investigated was $^{16}O+^{62}Ni$ at 42 MeV, which is near the top of the Coulomb barrier [47]. I performed coupled reaction channel calculations using FRESCO [45] to produce elastic S-matrices for the inelastic channels only and for the one-nucleon transfer channels. The four-nucleon transfer channels were found by Keeley *et al.* [47, 52] to have negligible cross-section, so it was decided not to include those channels. The channels included in the CRC calculations are:

- the inelastic excitation of the 2^+ and 3^- states of ^{62}Ni and the 3^- state of ^{16}O
- the $^{62}Ni(^{16}O,^{17}O)^{61}Ni$ and $^{62}Ni(^{16}O,^{15}N)^{63}Cu$ transfer channels.

Two-way couplings between the entrance channel only to each of the relevant transfer channels were included. The residual optical model in the entrance channel is the bare

double-folded real potential and a Woods-Saxon-squared imaginary potential, of depth 40 MeV, radius parameter 1.0 fm and diffuseness parameter 0.4 fm. For further details concerning the optical model potentials for propagation in the transfer partitions, spectroscopic factors, etc., see Keeley *et al.*'s paper [47].

The extended optical model fusion potential for this case is therefore $W_{\rm F}(r) = W_{\rm OF}(r) + \xi\{W^{\rm inel}_{\rm DPP}(r) + W^{\rm 1NT}_{\rm DPP}(r)\}$. This does not alter the basic nature of the analysis, since the extended optical model includes only the channels with non-negligible cross-section. It is not possible to determine the actual value of ξ in this case, since the total fusion cross-section $\sigma_{\rm F}$ has not been experimentally measured yet. However, if necessary, it is possible to obtain reasonable approximations to the value of ξ by making the assumption that the relative contributions of the DPPs to the total spin distribution are the same for the EOM as for the BPM.

When carrying out the inversions, I found particular difficulty with the S-matrix which incorporates only the inelastic couplings. This was caused by the difficulty of fitting the 'shoulder' in $|S(l)|$ at $l \sim 15$ (a feature which is probably due to interference effects between the nuclear and Coulomb scattering). This 'shoulder' is too small to be visible in Fig. 5.16, but has a significant effect on the scattering and the inversion calculations, because of its location in the sensitive l-range and the fact that its magnitude is comparable to $1 - |S(l)|$. It was the difficulty in fitting this feature which prompted me to investigate the use of a long-range Coulomb-excitation tail such as the LTS or BGKP forms as part of the starting reference potential for the inversion (see Section 5.3).

It is important to note that the 'one-nucleon transfer' DPP presented in this section is not the same as that presented in Section 5.6. In this section, the inelastic couplings between the excited states of the other partitions have been included in the CRC calculations, since these couplings will probably modify the fusion DPP, whereas in Section 5.6 the additivity of the component parts of the one-nucleon transfer DPP is investigated, and the coupling between the exited states of the transfer partitions would have falsified the assumption that the underlying DPPs must be additive.

Fig. 5.16 shows the CRC-calculated elastic S-matrices for the bare potential used (the un-normalised double-folding real potential and a Woods-Saxon squared imaginary potential with $WS = 40$ MeV, $r_w = 1.0$ fm and $a_w = 0.4$ fm used by Keeley *et al.* [47, 52, 50]). One of the effects of coupling to only the inelastic channels is to change the shape of the S-matrix modulus. There is increased absorption in the high l-range, including a long tail extending to $l \sim 80$ that was shown in Section 5.3 to be due to Coulomb excitation to the 2^+ state of the target nucleus. This increased absorption relative to the S-matrix of the bare potential extends down to $l \sim 8$, and for $0 < l < 8$ there is actually *less absorption* than from the bare potential. The S-matrix argument has a longer tail than that of the bare potential, remains slightly larger down to $l \sim 14$, and is then significantly smaller for $l < 14$.

The one-nucleon transfer channels have a different effect on the S-matrix. The radial shape of the S-matrix broadly matches that of the bare potential, with greater absorption over the whole l-range of the modulus. The argument of the one-nucleon transfer S-matrix is close to that of the bare potential, but has a longer tail and is

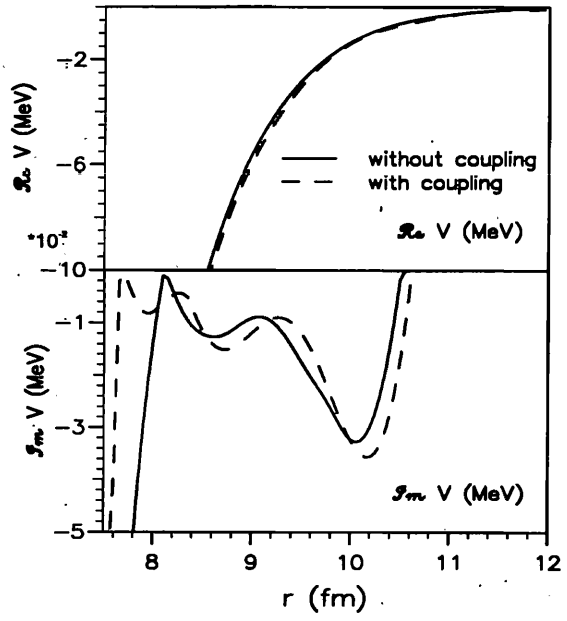

Figure 5.14: Comparison of the inverse one-nucleon transfer DPP, $W_{\rm DPP}^{\rm 1NT}$ with and without coupling between the inelastic channels in the one-nucleon transfer partition for ^{16}O+^{62}Ni at $E_{\rm lab} = 42$ MeV.

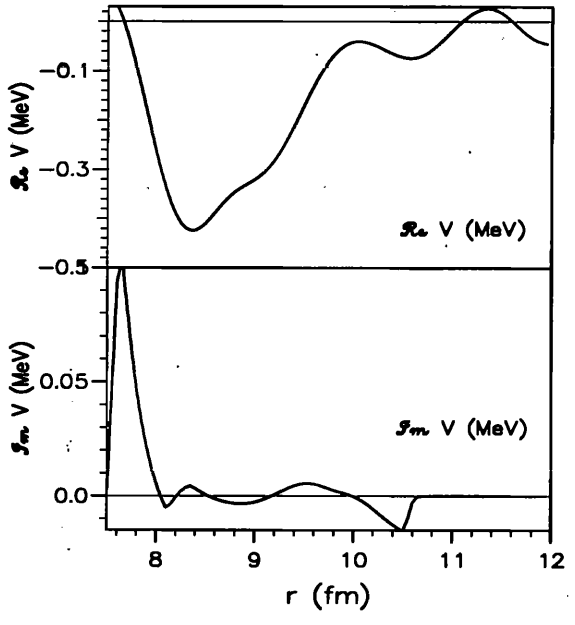

Figure 5.15: As in the previous figure, but the DPP without coupling has been subtracted from the DPP with coupling.

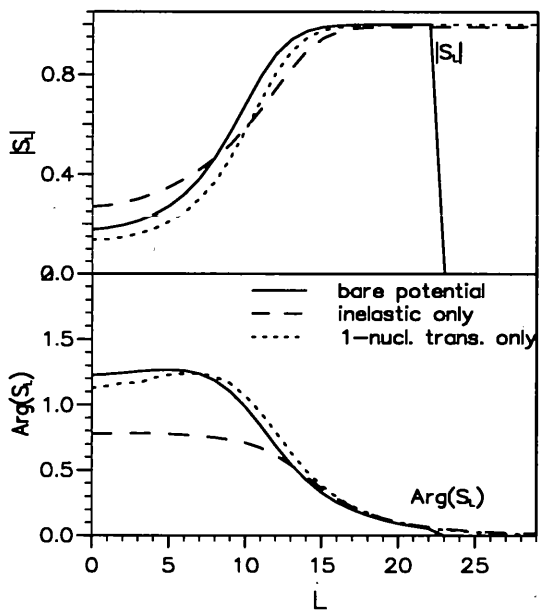

Figure 5.16: The CRC-calculated S-matrices for the bare potential, the inelastic channels only, and the one-nucleon transfer channels for $^{16}O+^{62}Ni$ at $E_{lab} = 42$ MeV. The sharp cutoff at high l for the bare $|S(l)|$ is an artefact of the data storage and has no physical significance.

broadly similar to the inelastic Arg($S(l)$) for $l > 15$. For lower l-values, it is slightly greater than the bare potential Arg($S(l)$) until $l \sim 7$, while for $0 < l < 7$ it dips slightly below the bare potential Arg($S(l)$).

The semi-classical correspondence between the values of angular momentum and radius means that the features of the S-matrix are expected to be reflected in the radial shape of the corresponding potentials. It is clear from Fig. 5.16 that the shape of the S-matrices for inelastic channel coupling and for one-nucleon transfer coupling are quite different, and even prior to inversion it is apparent that the radial shapes of the corresponding DPPs will be quite different. This is in fact borne out by the inverse DPPs, which are presented below.

Figs. 5.17 and 5.18 show the inverse potential and the DPP (obtained by subtracting the bare potential from the inverse potential) derived from the CRC S-matrix for the coupling to the inelastic channels only. While only the imaginary parts of the DPPs are important for the calculation of the fusion cross-sections, the real parts are included for completeness. The imaginary inverse potential has a small emissive peak at $r \sim 11$ fm, and a deep absorptive well of about 2 MeV at $r \sim 9$ fm. The absorption then decreases to form a 'hump' at $r \sim 8$ fm, following which the absorption increases again until, for radii less than about 4 fm, the inverse potential is approximately the same as the bare potential. The imaginary DPP due to coupling to the inelastic channels only (obtained by subtracting the bare potential from the inverse potential), $W_{\mathrm{DPP}}^{\mathrm{inel}}$, is shown in Fig. 5.18. It is interesting to note that the real part is strongly repulsive over the range $6 < r < 9$ fm, but has a shallow attractive well at about 10fm, which is

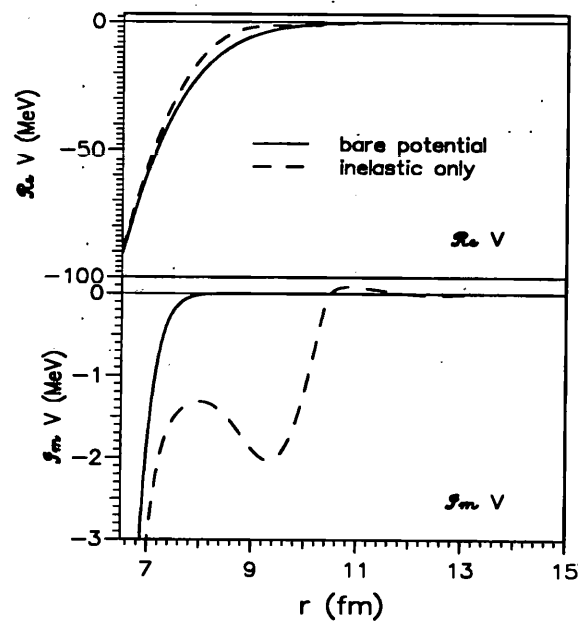

Figure 5.17: The CRC bare potential, W_{OF}, and the inverse potential for the inelastic channels for ^{16}O+^{62}Ni at $E_{\mathrm{lab}} = 42$ MeV.

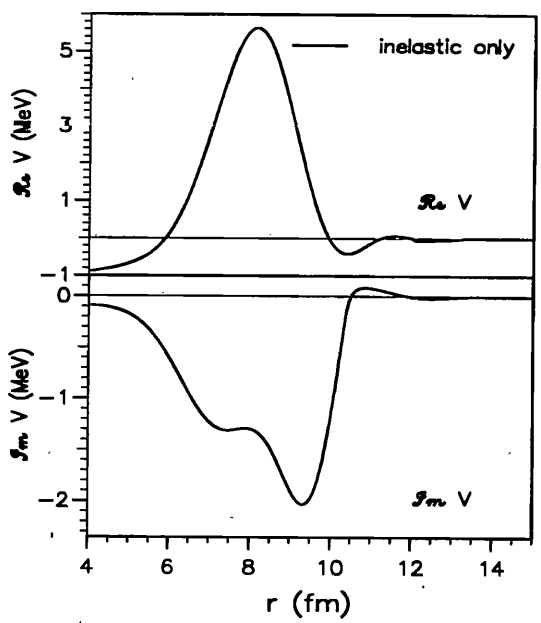

Figure 5.18: The inverse DPP, $W^{\mathrm{inel}}_{\mathrm{DPP}}$, for the inelastic channels for ^{16}O+^{62}Ni at $E_{\mathrm{lab}} =$ 42 MeV.

the SAR for this case. This contrasts with the real DPP for one-nucleon transfer, to be presented shortly. The imaginary part, $W_{\rm DPP}^{\rm inel}$ has a small emissive peak at the SAR, but becomes absorptive at lower radii, reaching a depth of about 2 MeV at about 9 fm. For radii less than about 4 fm, the imaginary DPP becomes negligible. The 'saddle point' at $r \sim 7$ fm corresponds to the 'hump' of decreased absorption in Fig. 5.17.

Figs. 5.19 and 5.20 display the inverse potential and the DPP for the one-nucleon transfer channels, compared with and then subtracted from the bare potential respectively. The shape of the imaginary part of the inverse potential has an absorptive well at $r \sim 10$ fm, the SAR, reaching a depth of about 0.04 MeV. There is decreased absorption for lower radii, leading to a 'hump' at $r \sim 9$ fm, followed by a shallower absorptive well at $r \sim 8.5$ fm, which has a depth of only about 0.015 MeV. There is another 'hump' of decreased absorption at $r \sim 8$ fm, another shallower well at $r \sim 7$ fm (~ 0.01 fm), another 'hump' at $r \sim 7.7$ fm, followed by decreased absorption for lower radii. For $r < 6.5$ fm, the inverse potential matches onto the bare potential. The imaginary part of the DPP due to the coupling to the one-nucleon transfer channels only (which is the difference between the inverse and bare potentials), $W_{\rm DPP}^{\rm 1NT}$, is shown in Fig. 5.20. It has an absorptive well at $r \sim 10$ fm and a somewhat shallower well at $r \sim 8.5$ fm, separated by a 'hump' of decreased absorption. Between about 7.5 and 8 fm, there is a large emissive peak, which reaches a maximum of about 0.1 MeV. This is followed by a deep absorptive well at about 7.3 fm (~ 0.075 MeV), another, smaller emissive peak at $r \sim 6.9$ fm (~ 0.03 MeV), and a shallow (~ 0.01 MeV) absorptive well at $r \sim 6.6$ fm. These alternating bands of emission and absorption between 6.5 and 8

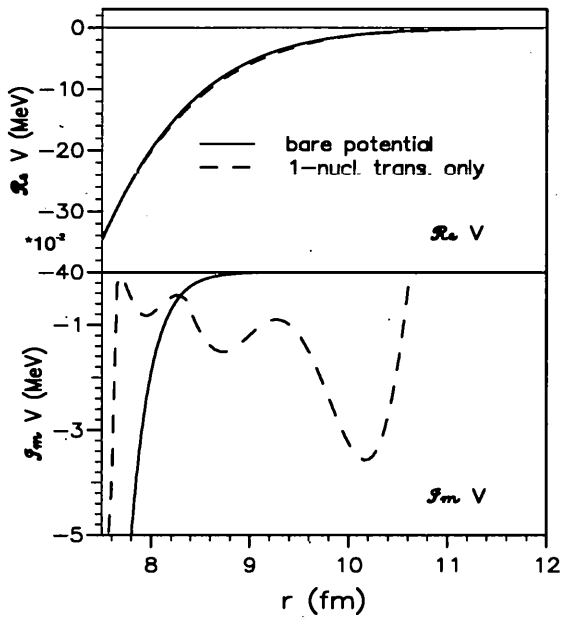

Figure 5.19: The CRC bare potential, $W_{\rm OF}$, and the inverse potential for the one-nucleon transfer channels for ^{16}O+^{62}Ni at $E_{\rm lab} = 42$ MeV. The scale for the imaginary part is 10^{-2}.

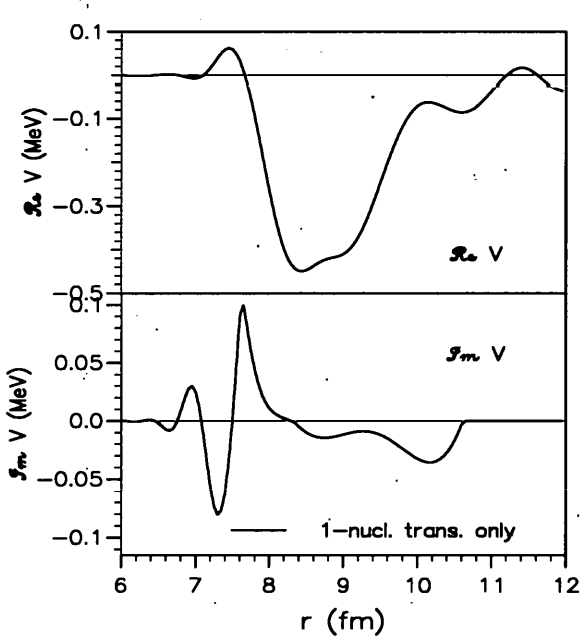

Figure 5.20: The inverse DPP, $W^{\rm 1NT}_{\rm DPP}$, for the one-nucleon transfer channels for ^{16}O+^{62}Ni at $E_{\rm lab} = 42$ MeV.

fm are usually characteristic of significant l-dependence in the underlying DPP. I found similar evidence for l-dependence in the one-nucleon transfer DPP which excludes the coupling between the excited states of the transfer partitions, which is presented in Section 5.6; this indicates that in this case such l-dependence is not due to couplings between those excitation states.

It is clear from a comparison of Figs. 5.18 and 5.20 that the radial shapes and magnitudes of the imaginary DPPs for inelastic coupling and for one-nucleon transfer coupling are very different, and neither of them conform to a standard optical model form. In particular, the radial behaviour of $W_{\rm DPP}^{\rm 1NT}$, with its alternating bands of emission and absorption, is highly non-standard.

It may seem remarkable that the apparently small $W_{\rm DPP}^{\rm 1NT}$ potential in Fig. 5.20 have the same magnitude effect on the S-matrix in Fig. 5.16 as the $W_{\rm DPP}^{\rm inel}$ in Fig. 5.18; however, it must be remembered that in heavy-ion scattering, the potential in the region of the strong absorption radius (SAR) has an overwhelming influence on the scattering, compared to the potential at other radii. In this case, the SAR is centred around $r \sim 11$ fm, and in this radial region the two potentials $W_{\rm DPP}^{\rm inel}$ and $W_{\rm DPP}^{\rm 1NT}$ have comparable magnitudes, and therefore the same magnitude effect on the scattering matrix.

It is useful to present the predictions of the BPM for this case, for later comparison with the extended optical model (EOM) results. Fig. 5.21 shows the partial fusion cross-sections for the bare potential and the two DPPs (*not* IP inversion DPPs), as calculated by the coupled-channels code FRESCO. It uses the BPM method, with

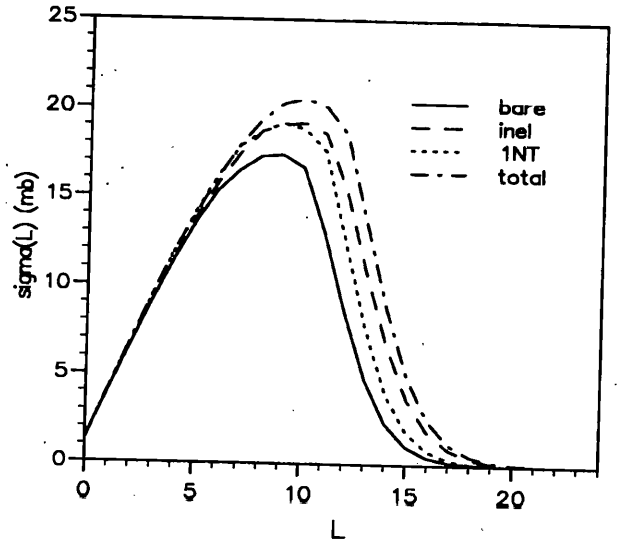

Figure 5.21: The BPM partial wave fusion cross-sections, $\sigma_{\mathrm{F,BPM}}(l)$s, for ^{16}O+^{62}Ni at $E_{\mathrm{lab}} = 42$ MeV.

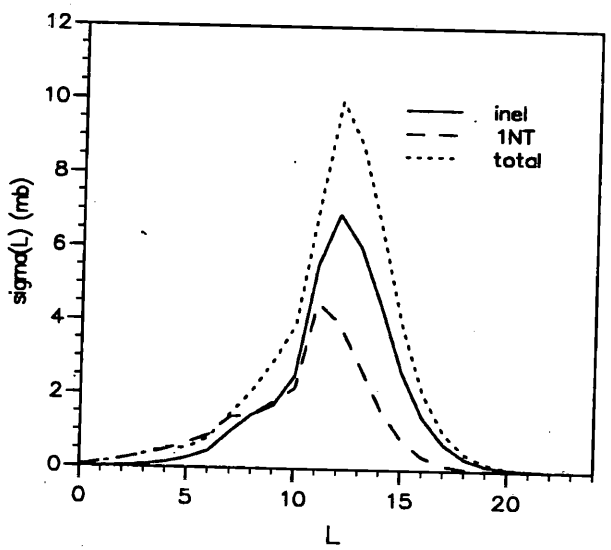

Figure 5.22: The contributions to $\sigma_{\mathrm{F,BPM}}(l)$ by $V^{\mathrm{inel}}_{\mathrm{TELP}}$ and by $V^{\mathrm{1NT}}_{\mathrm{TELP}}$ for ^{16}O+^{62}Ni at $E_{\mathrm{lab}} = 42$ MeV, obtained by subtracting $\sigma^{\mathrm{bare}}_{\mathrm{F,BPM}}(l)$ from the curves in the previous figure.

the trivially-equivalent local potentials (TELPs) representing the effects of channel coupling. The TELPs are averaged over all partial waves with a weighting factor of $(2l+1)(1-|S(l)|^2)$, to emphasise the effect of the peripheral partial waves. The shapes of the $\sigma_{\mathrm{F,BPM}}(l)$ seem physically reasonable, with a single peak in the high l-range. The channel coupling has the most significant effect on the fusion cross-section in the grazing partial waves. The partial fusion cross-sections are short-range; even with the effects of channel coupling included, there is no long-range tail in $\sigma_{\mathrm{F,BPM}}(l)$. The mean values of l and l^2 are given in Tables 5.4 and 5.5. The total fusion cross-sections are predicted to be 159.4 mb for the bare potential, with the additional cross-section when the TELP DPPs are added to the potential being 35.9 mb when $V^{\mathrm{inel}}_{\mathrm{TELP}}$ is added, 24.1 mb when $V^{\mathrm{1NT}}_{\mathrm{TELP}}$ is added and 212.5 mb for the bare potential plus both the TELP potentials. Unfortunately, there are no measured values for the fusion cross-sections for this case.

Fig. 5.22 shows the contribution to $\sigma_{\mathrm{F,BPM}}(l)$ for the TELPs, compared with the contribution from the bare potential alone. $\sigma^{\mathrm{inel}}_{\mathrm{F,BPM}}(l)$ is peaked at $l = 13$ while $\sigma^{\mathrm{1NT}}_{\mathrm{F,BPM}}(l)$ peaks at $l = 12$. Their sum has about half the maximum magnitude of $\sigma^{\mathrm{bare}}_{\mathrm{F,BPM}}(l)$. Neither $\sigma^{\mathrm{inel}}_{\mathrm{F,BPM}}(l)$ nor $\sigma^{\mathrm{1NT}}_{\mathrm{F,BPM}}(l)$ have a long-range tail.

Fig. 5.23 directly compares the predictions for $\sigma^{\mathrm{bare}}_{\mathrm{F}}(l)$ of the BPM and the EOM. $\sigma^{\mathrm{bare}}_{\mathrm{F,EOM}}(l)$ was calculated using the bare imaginary potential and the scattering wavefunction due to the bare potential only (in all other cases in this analysis, the total scattering wavefunction is used). There is extremely good agreement between the two models, the two curves having the same shape and magnitude, and both peaking at the

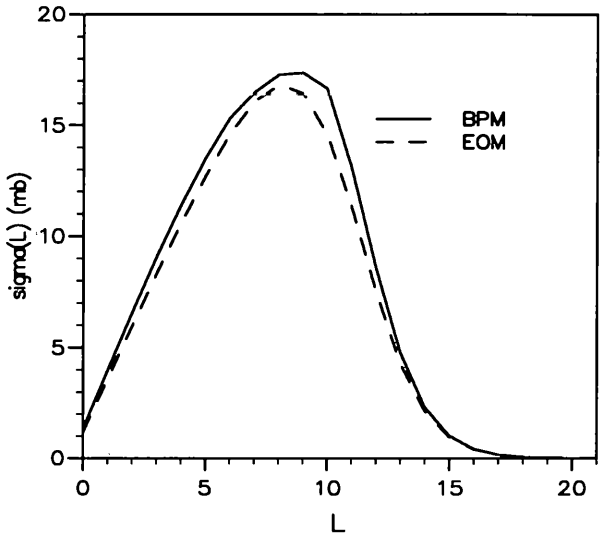

Figure 5.23: The values of $\sigma_{\rm F}^{\rm bare}(l)$, for ^{16}O+^{62}Ni at $E_{\rm lab}$ = 42 MeV, predicted by the BPM and the EOM using the bare potential scattering wavefunction.

same l-value. The predicted values for the total fusion cross-section ($\sigma_{\rm F,BPM}^{\rm bare}$ = 159.4 mb, $\sigma_{\rm F,EOM}^{\rm bare}$ = 147.9 mb), the mean l-value ($< l >_{\rm F,BPM}^{\rm bare}$= 7.49, $< l >_{\rm F,EOM}^{\rm bare}$= 7.45), and the mean l^2-value ($< l^2 >_{\rm F,BPM}^{\rm bare}$= 66.9, $< l^2 >_{\rm F,EOM}^{\rm bare}$= 73.58) also agree with reasonable accuracy.

Figs. 5.24 to 5.26 show the trivially-equivalent local potentials (TELP) for the inelastic and one-nucleon transfer DPPs, calculated using FRESCO, for comparison with the inverse DPPs calculated using the 'CRC+inversion' method (Figs. 5.18 and 5.20). The TELPs have been averaged by FRESCO over all partial waves with a weighting factor of $(2l+1)(1-|S(l)|^2)$, to emphasise the effect of the peripheral partial waves. These TELP DPPs will be referred to as $V_{\rm DPP,TELP}^{\rm inel}$ and $V_{\rm DPP,TELP}^{\rm 1NT}$ respectively.

The TELP DPPs are much more oscillatory than the inverse DPPs, and are

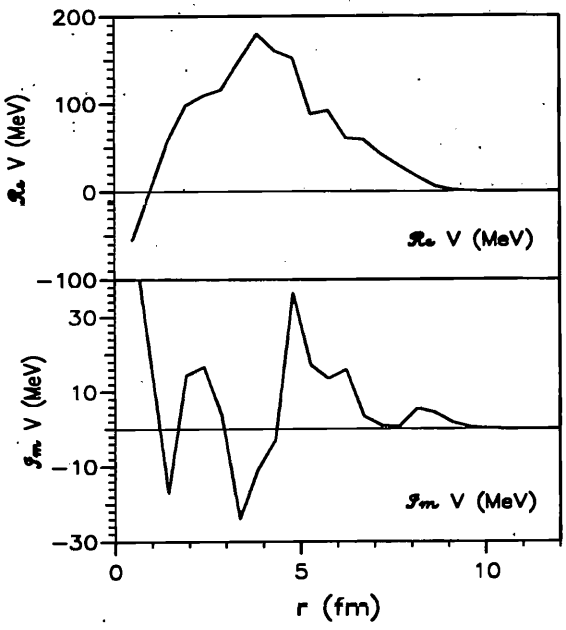

Figure 5.24: The trivially-equivalent local potential (TELP) DPP, $V^{\rm inel}_{\rm DPP,TELP}$, for the inelastic channels for ^{16}O+^{62}Ni at $E_{\rm lab} = 42$ MeV.

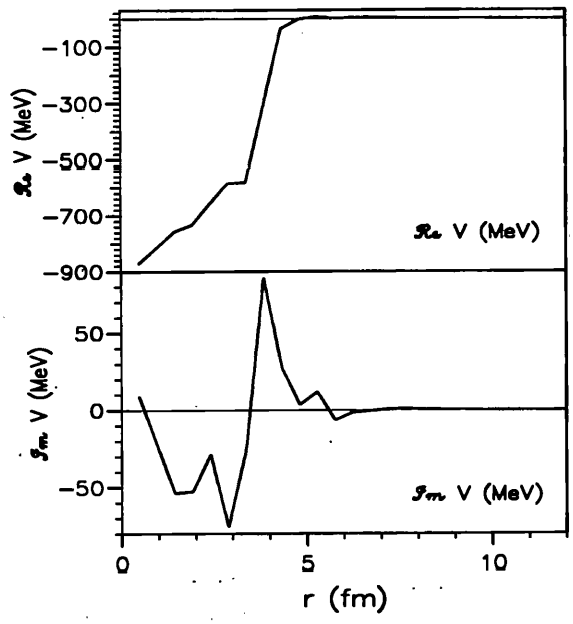

Figure 5.25: The trivially-equivalent local potential (TELP) DPP, $V^{\rm 1NT}_{\rm DPP,TELP}$, for the one-nucleon transfer channels for ^{16}O+^{62}Ni at $E_{\rm lab} = 42$ MeV, over the range $0 < r < 12$ fm.

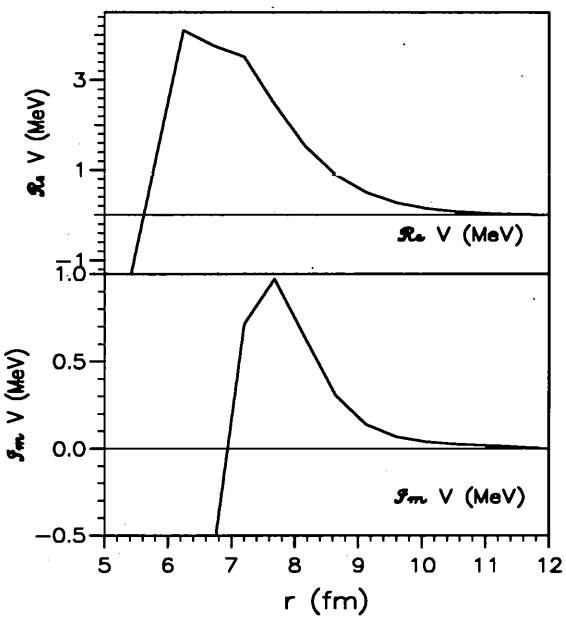

Figure 5.26: The trivially-equivalent local potential (TELP) DPP, $V^{\rm 1NT}_{\rm DPP,TELP}$, for the one-nucleon transfer channels for ^{16}O+^{62}Ni at $E_{\rm lab} = 42$ MeV, over the range $5 < r < 12$ fm.

comparatively shorter-ranged, becoming negligible by about 10 fm, whereas the inverse DPPs are significant out to $\sim$ 12 fm. The real part of $V^{\rm inel}_{\rm DPP,TELP}$ is strongly repulsive, reaching a peak of $\sim$ 200 MeV at $\sim$ 4 fm and falling to zero by $r \sim$ 10 fm. By contrast, while the $V^{\rm inel}_{\rm DPP,inv}$ in Fig. 5.18 also has a repulsive peak, it is much shallower ($\sim$ 5 MeV) and is at $r \sim$ 8 fm. There is also a shallow attractive well at $r \sim$ 10 fm which is absent in $V^{\rm inel}_{\rm DPP,TELP}$. The imaginary part of $V^{\rm inel}_{\rm DPP,TELP}$ is extremely oscillatory, only settling into something reasonably smooth for $r >\sim$ 5 fm. It is emissive at these larger radii, falling from a maximum of about 30 MeV at $r \sim$ 5 fm to zero by $r \sim$ 10 fm. The imaginary part of $V^{\rm inel}_{\rm DPP,inv}$, on the other hand, is much smoother and is absorptive for all $r <\sim$ 10 fm, reaching a minimum of about -2 MeV at $r \sim$ 9.5 fm. There is a slight emissive peak at r$\sim$ 11 fm which is absent in the imaginary part of $V^{\rm inel}_{\rm DPP,TELP}$.

The TELP for the one-nucleon transfer DPP, $V^{\rm 1NT}_{\rm DPP,TELP}$, is shown in Figs. 5.25 and 5.26. The real part is very strongly attractive in the interior ($r <\sim$ 5 fm), starting from a minimum of -900 MeV and becoming negligible by about $r \sim$ 10 fm. There is a shallow repulsive peak at $r \sim$ 7 fm ($\sim$ 4 MeV), but the potential then monotonically falls to zero. The real part of the inverse DPP, shown in Fig. 5.20, is very different. It is negligible for $r <\sim$ 7 fm, has a shallow repulsive peak at $r \sim$ 7.5 fm, has an attractive well for 8 fm $<\sim r <\sim$ 11 fm (reaching a minimum of -0.45 MeV at $r \sim$ 8.5 fm) and a shallow repulsive peak at $r \sim$ 11.5 fm. The imaginary part of the TELP DPP, $V^{\rm 1NT}_{\rm DPP,TELP}$, is quite oscillatory.

It is clear that the TELP DPPs for these channels are neither smooth nor physically reasonable. The one-nucleon transfer TELP, in particular, is far too deep in the

interior (> 800 MeV) in the real part, and the peak in the real part of the inelastic TELP is too large (> 150 MeV). Indeed, the magnitude of the TELPs is much greater than that of the inverse DPPs over almost all of the radial range, by several orders of magnitude. The TELPs are not surface-peaked, as would be expected for direct reactions, but have most of their magnitude in the interior ($r < 5$ fm). This is in contrast to the inverse DPPs, which are significant only between about 6 and 12 fm.

When calculating the partial fusion cross-sections from my inverse DPPs, $W_{\rm DPP}^{\rm inel}(r)$ and $W_{\rm DPP}^{\rm 1NT}(r)$, a problem arises. Not all the strength of the inverse DPPs will contribute to fusion; only $\xi W_{\rm DPP}$ will do so. However, because there are no measured experimental values of $\sigma_{\rm F}$ and $\sigma_{\rm F}(l)$ for this case, the usual method of determining ξ (matching the predicted value of $\sigma_{\rm F}$ to the experimental value) cannot be used here. The total fusion cross-section $\sigma_{\rm F}$ and the shape of $\sigma_{\rm F}(l)$ will both depend strongly on the value of ξ. Before the analysis can continue, assumptions must therefore be made. There are two approaches to this problem presented in this analysis: (i) to assume that the proportional contribution of the DPPs to the total fusion cross-section, relative to that of the bare potential, is the same for both the BPM and the EOM. This will give a separate value of ξ for each DPP. This approach will be labelled 'EOM1'. (ii) to assume that the value of ξ found by Satchler *et al.* [80] in the case of ^{32}S+^{64}Ni at 88 MeV will be close to its value for ^{16}O+^{62}Ni at 42 MeV. This will give a single value of ξ for all DPPs, and this approach will be labelled 'EOM2'.

$< l >_F$	bare	+inel	+1NT	+inel+1NT
BPM	7.49	8.33	7.88	8.58
EOM1	8.03	9.04	8.32	9.19
EOM2	8.03	11.93	8.20	11.88

Table 5.4: Values for the average of l for the bare potentials plus the DPPs, calculated by FRESCO using the BPM and by the 'CRC+inversion' method using the extended optical model with separate values for ξ^{inel} and ξ^{1NT} (EOM1) and a single ξ value taken from Satchler *et al.* [80] (EOM2).

$< l^2 >_F$	bare	+inel	+1NT	+inel+1NT
BPM	66.9	82.6	73.7	87.3
EOM1	166.9	200.2	164.0	194.5
EOM2	166.9	295.4	165.2	291.8

Table 5.5: Values for the average of l^2 for the bare potential plus the DPPs, calculated by FRESCO using the BPM and by the 'CRC+inversion' method using the extended optical model with separate values for ξ^{inel} and ξ^{1NT} (EOM1) and a single ξ value taken from Satchler *et al.* [80] (EOM2).

The 'EOM1' approach: $\xi^{\rm inel} = 7.537 \times 10^{-3}$ and $\xi^{\rm 1NT} = 0.1509$. The fundamental assumption of this approach is that the contribution of the DPPs to the partial fusion cross-section is proportionately the same for the extended optical model as for the barrier penetration model; i.e.,

$$\frac{\sigma^{\rm inel}_{\rm F,EOM}}{\sigma^{\rm bare}_{\rm F,EOM}} \sim \frac{\sigma^{\rm inel}_{\rm F,BPM}}{\sigma^{\rm bare}_{\rm F,BPM}}, \text{ and } \frac{\sigma^{\rm 1NT}_{\rm F,EOM}}{\sigma^{\rm bare}_{\rm F,EOM}} \sim \frac{\sigma^{\rm 1NT}_{\rm F,BPM}}{\sigma^{\rm bare}_{\rm F,BPM}}, \tag{5.26}$$

where $\sigma_{\rm F}^{\rm inel}$ stands for the fusion due to the bare potential plus the inelastic DPP, and $\sigma_{\rm F}^{\rm 1NT}$ stands for the fusion due to the bare potential plus the one-nucleon transfer DPP. This assumption implies separate values of ξ for the two DPPs, which is a useful result in its own right; the assumption that the DPPs share the same value of ξ is probably not realistic. The value of ξ is expected to vary with radius, being close to 1 in the interior (for the bare potential) and decreasing as the radius increases (the more peripheral a direct reaction, the less likely it is to contribute to fusion). The inelastic DPP is longer-ranged and much deeper than the one-nucleon DPP, so $\xi^{\rm inel}$ would be expected to be much smaller than $\xi^{\rm 1NT}$.

The EOM1 can now be written as $W_{\rm F}(r) = W_{\rm OF}(r) + \xi^{\rm inel} W^{\rm inel}_{\rm DPP}(r) + \xi^{\rm 1NT} W^{\rm 1NT}_{\rm DPP}(r)$, where

$$\xi^{\rm inel} = \frac{\sigma^{\rm inel}_{\rm F,BPM} \sigma^{\rm bare}_{\rm F,EOM}}{\sigma^{\rm bare}_{\rm F,BPM} \sigma^{\rm inel,full}_{\rm F,EOM}}, \tag{5.27}$$

(where $\sigma^{\rm inel,full}_{\rm F,EOM}$ has been calculated using the full $W^{\rm inel}_{\rm DPP}$; i.e., without a factor ξ), and likewise to calculate $\xi^{\rm 1NT}$. For this case, $\xi^{\rm inel} = 7.537 \times 10^{-3}$ and $\xi^{\rm 1NT} = 0.1509$. These values compare with that given by Satchler *et al.* [80], who found $\xi = 0.081$ for the

DPPs of $^{32}S+^{64}Ni$ at 88 MeV.

If ξ is allowed to vary with radius, then the radial shape of that part of the DPP which contributes to fusion will not necessarily be the same as the shape of the total DPP itself. However, given the absence of experimental data for $\sigma_F(l)$, there is presently no way of determining the extent of such differences in shape, or whether they could have a significant effect on the shape of $\sigma_F(l)$.

The EOM1 partial fusion cross-sections are presented in Figs. 5.27 and 5.28. The predicted values of the total fusion cross-section σ_F cannot be usefully compared with those predicted by the BPM, since they were calculated on the assumption of Eq. 5.26. Furthermore, the values of σ_F predicted by the EOM1 using the total scattering wavefunction are less than those of the BPM by more than an order of magnitude. While the predictions of the EOM1 agree with those of the BPM when the scattering wavefunction due to only the bare potential is used, the total scattering wavefunction is significantly absorbed in the region of the strong absorption radius (SAR), so that the magnitude of the integrand in Eq. 5.20 is greatly reduced. This strong absorption is shown in Fig. 5.29, which compares the scattering wavefunction due to only the bare potential with that due to the total potential.

The shape of $\sigma_F(l)$ is also significantly different. The peak is skewed to a lower l-value ($l \sim 6$) compared to the BPM (where the peak is at $l \sim 9$), and the comparative shapes of the $\sigma_F(l)$ due to the DPPs are also different from the BPM. The BPM predicts that $\sigma^{inel}_{F,BPM}(l) \sim \sigma^{1NT}_{F,BPM}(l)$ for $l < 10$ and is greater than the one-nucleon transfer partial cross-section for $l > 10$. In the EOM1, $\sigma^{inel}_{F,EOM}(l) > \sigma^{1NT}_{F,EOM}(l)$ for

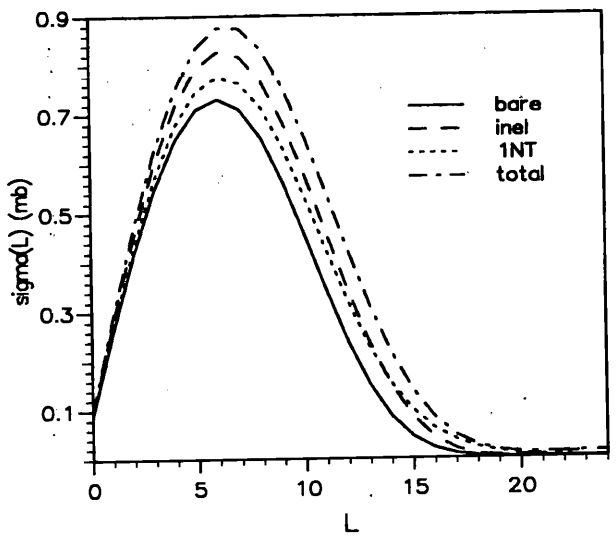

Figure 5.27: The EOM1 partial wave fusion cross-sections, $\sigma_{\mathrm{F,EOM}}(l)$s where $0 < l < 24$, for ^{16}O+^{62}Ni at $E_{\mathrm{lab}} = 42$ MeV.

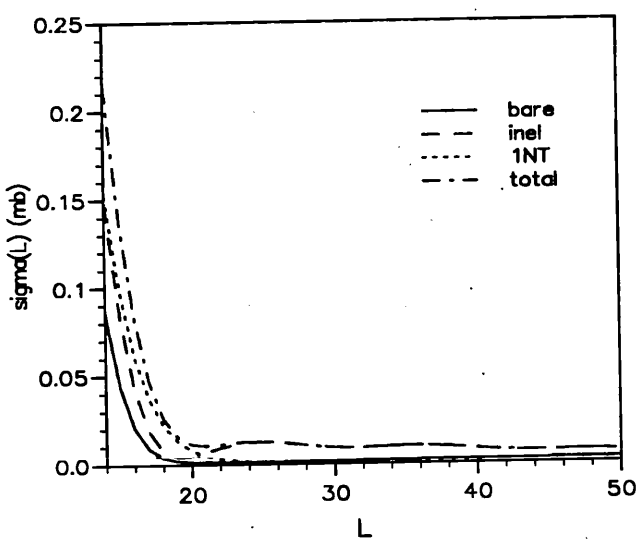

Figure 5.28: The EOM1 partial fusion cross-sections, $\sigma_{\mathrm{F,EOM}}(l)$s where $14 < l < 50$, for ^{16}O+^{62}Ni at $E_{\mathrm{lab}} = 42$ MeV.

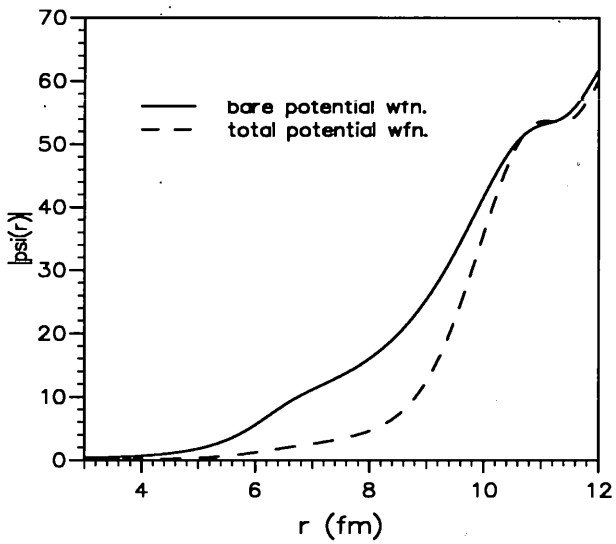

Figure 5.29: The magnitude $|\chi(r)|$ of the scattering wavefunction due to only the bare potential, compared with $|\chi(r)|$ due to the total potential for ^{16}O+^{62}Ni at $E_{\rm lab} = 42$ MeV.

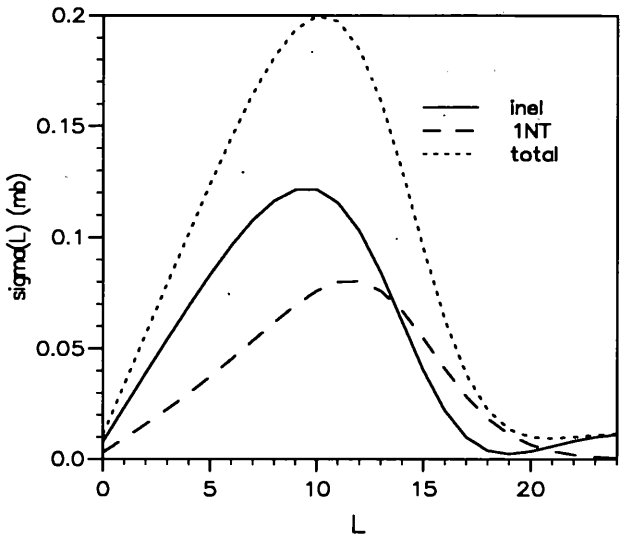

Figure 5.30: The EOM1 contributions to $\sigma_{\mathrm{F,EOM}}(l)$ by $W_{\mathrm{DPP}}^{\mathrm{inel}}$ and by $W_{\mathrm{DPP}}^{\mathrm{1NT}}$, where $l < 24$, for ^{16}O+^{62}Ni at $E_{\mathrm{lab}} = 42$ MeV.

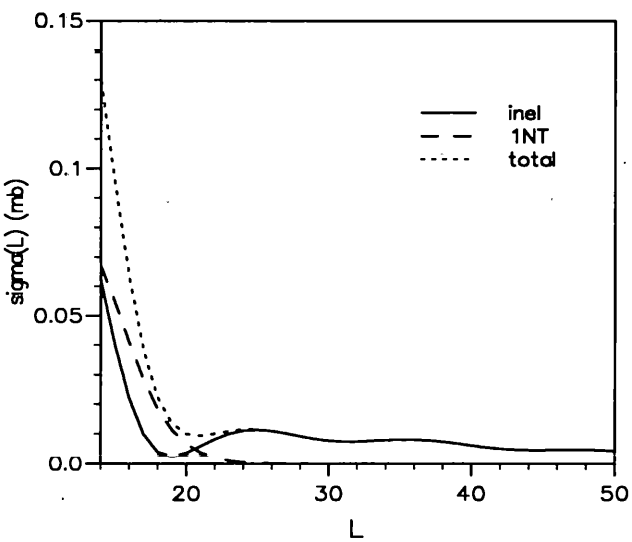

Figure 5.31: The EOM1 contributions to $\sigma_{\mathrm{F,EOM}}(l)$ by $W_{\mathrm{DPP}}^{\mathrm{inel}}$ and by $W_{\mathrm{DPP}}^{\mathrm{1NT}}$, where $14 < l < 50$, for ^{16}O+^{62}Ni at $E_{\mathrm{lab}} = 42$ MeV.

$l < 13$, the one-nucleon transfer cross-section becoming greater than that due to the inelastic DPP over the region $13 < l < 20$, while for $l > 20$, $\sigma^{\rm inel}_{\rm F,EOM}(l)$ has a long tail extending beyond $l \sim 40$ whereas $\sigma^{\rm 1NT}_{\rm F,EOM}(l)$ falls to zero by $l \sim 22$, as shown in Fig. 5.28.

The most significant fact is that there is only one peak in $\sigma_{\rm F}(l)$. This is the physically expected behaviour, and contrasts with the results obtained by Satchler *et al.* [80] for ^{32}S+^{64}Ni, in which the surface-peaked contribution of the direct reaction DPPs causes a second peak to appear in $\sigma_{\rm F}(l)$ at large l-values. This non-physical behaviour is probably due to the fact that the radial shapes of Satchler's DPPs are strongly surface-peaked. A realistic potential would probably be intermediate in shape between the volume-term bare potential and a purely surface-peaked potential. The DPPs obtained using the IP method on the coupled reaction channels S-matrices have this property, and, given a realistic value for the parameters $\xi^{\rm inel}$ and $\xi^{\rm 1NT}$, their contribution to $\sigma_{\rm F}(l)$ does not give an unphysical second peak.

Figs. 5.30 and 5.31 show the contributions of the DPPs to $\sigma_{\rm F,EOM}(l)$, with $\sigma^{\rm bare}_{\rm F,EOM}(l)$ subtracted. The inelastic contribution peaks at about $l \sim 10$, whereas that of the one-nucleon transfer DPP peaks at $l \sim 12$ and at a lower magnitude. Furthermore, the inelastic contribution has two main components: a large peak in the low l-range, and a long small tail extending from about $l \sim 20$ to $l \sim 80$, whereas the one-nucleon transfer contribution has no such tail, falling to zero by about $l = 24$. Comparing Figs. 5.22 and 5.30, it is clear that there are significant differences: the effect of channel coupling has been to broaden the spin distributions, and the main peak of the inelastic

contribution has been shifted to a lower l-value; the inelastic $\sigma_{\rm F}(l)$ also has a long tail in the high l-range which is missing in the BPM. The magnitudes of the EOM1 spin distributions are significantly less than for the BPM, by a factor of about 50. This is caused by the strong absorption of the scattering wavefunction near the SAR.

The long tail in $\sigma_{\rm F}(l)$ is due to the surface tail in $W^{\rm inel}_{\rm DPP}$, which is caused by the coupling to the Coulomb excitation of the 2^+ state of ^{62}Ni (see Section 5.3). The fact that this tail in $\sigma_{\rm F}(l)$ extends out to $l \sim 80$ is almost certainly not physically realistic, since direct reactions at such large radii would have a vanishingly small probability of leading to fusion. The problem is caused by the fact that the shape of that proportion $\xi^{\rm inel} W^{\rm inel}_{\rm DPP}$ of the inelastic DPP which leads to fusion is assumed to have the same radial shape as the full $W^{\rm inel}_{\rm DPP}$. This assumption seems reasonable in the case of $W^{\rm 1NT}_{\rm DPP}$, which has a relatively restricted radial range, but must be questioned for $W^{\rm inel}_{\rm DPP}$, which extends to the far surface.

The values of $< l >$ and $< l^2 >$ for the BPM $\sigma_{\rm F}(l)$ using the TELPs calculated by FRESCO are consistently smaller than for the spin distributions calculated from the inverse DPPs. The values of $< l^2 >$ in particular are very much larger, by a factor greater than 2. This is clear evidence of the sensitivity of $\sigma_{\rm F}(l)$ to the coupling to the inelastic and transfer channels. A similar result was found by Kubo *et al.* [81] for ^{16}O on various Ca isotopes.

The 'EOM2' approach: $\xi = 0.081$. Because of the uncertainty in obtaining exact values for ξ, due to the absence of experimental fusion cross-sections for this case, an

alternative EOM approach was also used in this analysis, to establish the sensitivity of the results to the value of ξ.

In the EOM2, I make the assumption that the values of ξ found by Satchler *et al.* [80] for the case ^{32}S+^{64}Ni at 88 MeV is appropriate for ^{16}O+^{62}Ni at 42 MeV.

Figs. 5.32 to 5.35 show the results of this assumption. The effect of the one-nucleon transfer DPP on $\sigma_{\rm F}(l)$ is suppressed relative to the EOM1, and the inelastic DPP makes a much greater contribution, accounting for almost all of the coupled-channel fusion enhancement. In fact, $\sigma^{\rm inel}_{\rm F,EOM}(l)$ is nearly three times greater than that due to the bare potential alone. This is in contrast to the BPM result, shown in Figs. 5.21 and 5.22, where the channel coupling has only a marginal effect on the fusion cross-section. However, the EOM2 results still have the same general features as the EOM1: the partial fusion cross-sections are peaked at $l \sim 10$ and the long tail for $l > 20$ is due almost entirely to the inelastic DPP. It is notable that even with the higher value of ξ for $W^{\rm inel}_{\rm DPP}$, there is still only a single peak in $\sigma_{\rm F}(l)$, contrary to Satchler *et al.*'s result [80] and in general agreement with the EOM1 results.

The contribution to $\sigma_{\rm F}(l)$ from the DPPs alone with the bare potential contribution subtracted is shown in Figs. 5.34 and 5.35, which can be compared with Figs. 5.22, 5.30 and 5.31. The contribution from the inelastic DPP dominates, being ~ 30 times greater than the one-nucleon transfer contribution. The inelastic DPP contribution has the same shape for the EOM2 as for the EOM1: it peaks at $l \sim 10$ and has the same long tail for $l > 20$. However, the magnitude is greater, since ξ in EOM2 is greater than $\xi^{\rm inel}$ in EOM1. In fact, whereas the contribution from the one-nucleon

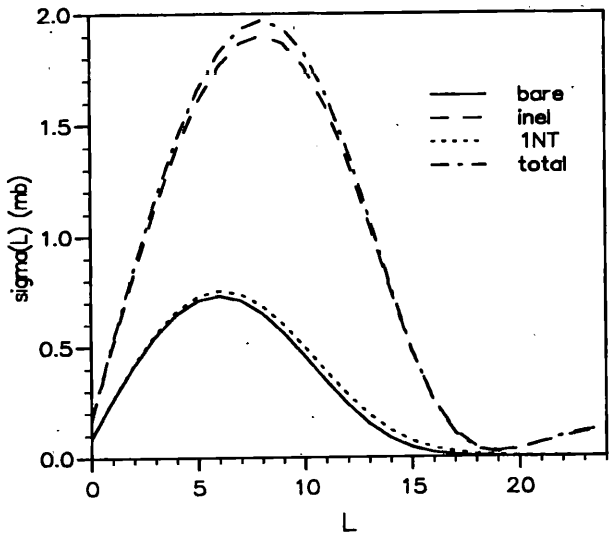

Figure 5.32: The EOM2 partial wave fusion cross-sections, $\sigma_{\mathrm{F,EOM}}(l)$s where $l < 24$, for ^{16}O+^{62}Ni at $E_{\mathrm{lab}} = 42$ MeV.

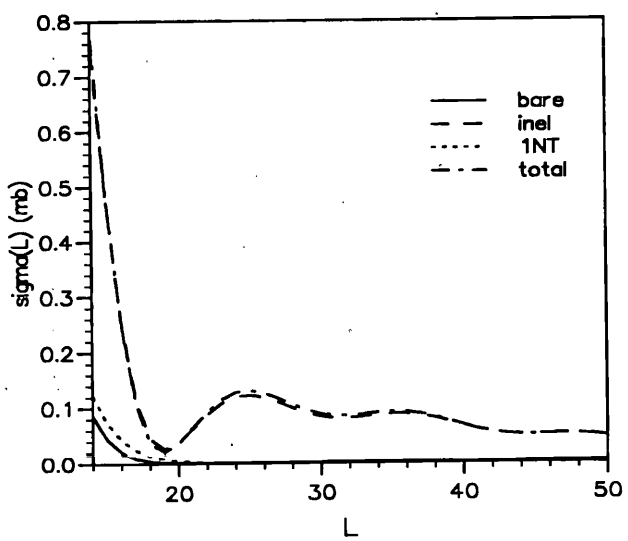

Figure 5.33: The EOM2 partial fusion cross-sections, $\sigma_{\mathrm{F,EOM}}(l)$s where $14 < l < 50$, for ^{16}O+^{62}Ni at $E_{\mathrm{lab}} = 42$ MeV.

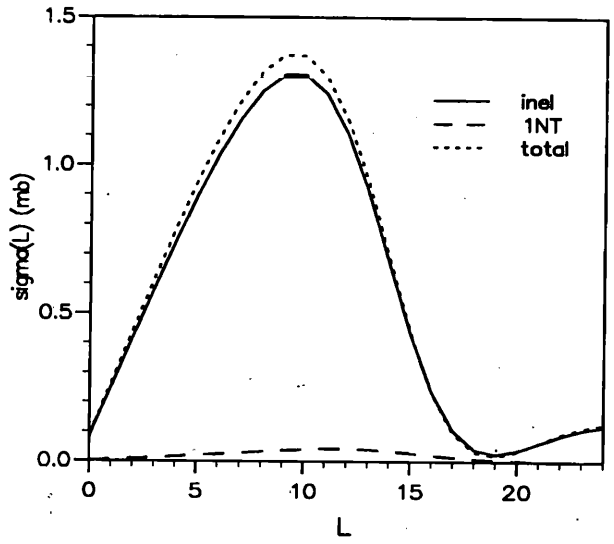

Figure 5.34: The EOM2 contributions to $\sigma_{\mathrm{F,EOM}}(l)$ by $W_{\mathrm{DPP}}^{\mathrm{inel}}$ and by $W_{\mathrm{DPP}}^{\mathrm{1NT}}$, where $l < 24$, for ^{16}O+^{62}Ni at $E_{\mathrm{lab}} = 42$ MeV.

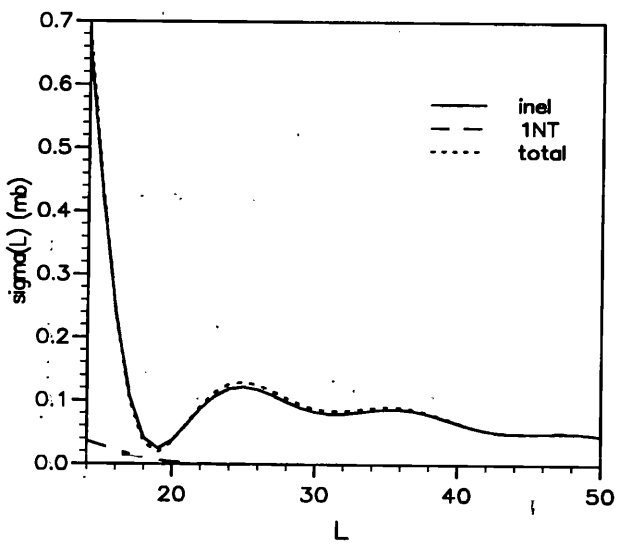

Figure 5.35: The EOM2 contributions to $\sigma_{\mathrm{F,EOM}}(l)$ by $W_{\mathrm{DPP}}^{\mathrm{inel}}$ and by $W_{\mathrm{DPP}}^{\mathrm{1NT}}$, where $14 < l < 50$, for ^{16}O+^{62}Ni at $E_{\mathrm{lab}} = 42$ MeV.

transfer DPP was comparable to that from the inelastic DPP for EOM1, in EOM2 the one-nucleon transfer DPP makes only a slight contribution.

The values of $< l >_F$ and $< l^2 >_F$ for EOM2 are compared with those for the BPM and EOM1 in Tables 5.4 and 5.5. The EOM2 mean l-value is greater than that of either the BPM or EOM1 for the inelastic DPP, but is less than that of the EOM1 for the one-nucleon transfer DPP (though still greater than that of the BPM). Since the contribution from the inelastic DPP is dominant, the EOM2 mean l-value is greater than that of the EOM1 for the total spin distribution. The mean l^2-value from the inelastic DPP contribution is very much greater for EOM2 than for either the BPM or EOM1, but the value for the one-nucleon transfer DPP is almost the same for both the EOM1 and EOM2. This behaviour of $< l >$ and $< l^2 >$ is to be expected, since the EOM2 ξ-value is greater for the inelastic DPP than the EOM1 ξ^{inel}, and the contribution from the inelastic DPP dominates at large l.

The most significant result of both the EOM1 and the EOM2 is the low magnitude of $\sigma_F(l)$ relative to the BPM results. For EOM1, $\sigma^{\mathrm{total}}_{F,\mathrm{BPM}}(l)/\sigma^{\mathrm{total}}_{F,\mathrm{EOM1}}(l) \sim 20$, and for EOM2 $\sigma^{\mathrm{total}}_{F,\mathrm{BPM}}(l)/\sigma^{\mathrm{total}}_{F,\mathrm{EOM2}}(l) \sim 10$. For the BPM and the EOM results to match, ξ would have to be close to unity, which is not physically reasonable.

The cause of this disagreement between the BPM and the EOM is the strong absorption of the scattering wavefunction in the surface region, due to the long tail in $W^{\mathrm{inel}}_{\mathrm{DPP}}(r)$. Fig. 5.29 shows very clearly the effect on $|\chi(r)|$; this accounts entirely for the suppression of the EOM $\sigma_F(l)$ relative to the BPM. It indicates the limitations of the elastic-channel potential model: the 'missing' fusion cross-section is probably being

contributed by the inelastic channels, and cannot therefore be accounted for in terms of the elastic-channel DPPs.

Conclusions. I have applied the extended optical model (EOM) in conjunction with CRC calculations and IP inversion as an alternative to the barrier penetration model (BPM). This has the potential to be useful for heavy-ion scattering near the Coulomb barrier, where channel coupling effects are expected to make a significant contribution to the fusion cross-section, both in terms of its magnitude and the shape of the partial fusion cross-section, $\sigma_{\rm F}(l)$.

In earlier EOM investigations [80], a strongly surface-peaked set of DPPs were used, which gave a second peak to the spin distribution, contrary to experimental evidence and expectation. The present DPPs were obtained as extremely accurate inversions from CRC-calculated S-matrix elements, and were intermediate in shape between the strongly surface-peaked DPPs of other investigators and the volume term of the bare potential. Their contribution to the spin distribution was therefore in accordance so far as shape is concerned with theoretical expectation, giving only a single peak at high l-values. This remained true even when the value of ξ was varied. However, there was a long tail in the contribution from the inelastic DPP in both EOM1 and EOM2. This was against the predictions of the BPM, but accorded with the results of other EOM analyses [80, 81]; however, the tail extended well beyond $l \sim 40$, and in these regions the probability of a direct reaction leading to fusion is negligible. The problem is that the factor $\xi^{\rm inel}$ is assumed to be constant, whereas in

an accurate analysis it should be expected to vary with radius.

The EOM1 approach presented here also represents a further extension to the extended optical model, since the simplifying assumption that the same proportion ξ of all DPPs will contribute to the fusion, which has been used by all previous applications of the EOM [80, 81], has no theoretical basis, and so separate factors ξ^{inel} and ξ^{1NT} were deduced under the assumption that the relative contributions to σ_{F} of the DPPs in the EOM were the same as for the BPM.

The necessity to make this link with the BPM indicates the need for accurate measurement of the experimental values of the total fusion cross-sections and the spin distributions for heavy ions near the Coulomb threshold. As this analysis has shown, the theoretical and calculational techniques now exist to make full use of the information content of an experimental $\sigma_{\text{F}}(l)$, and the detailed shape of the spin distribution can be used to deduce the relative contributions of the DPPs to fusion; that is, where I have had to use the BPM values of σ_{F} as a guide to deducing values for the factors ξ^{inel} and ξ^{1NT}, the experimental values could be used just as easily. Furthermore, the shape of the experimental $\sigma_{\text{F}}(l)$ could be use to give these factors a radial dependence, so that the shape of that part of a given DPP which contributes to fusion no longer has to be assumed to be the same as the shape of the total DPP itself. The unphysically long tail on $\sigma^{\text{inel}}_{\text{F,EOM}}(l)$ (see Fig. 5.28) indicates the need for this.

An important result obtained here is that the magnitude of the fusion cross-sections are underestimated by the EOM, compared with the BPM predictions, by a factor of between 10 and 20. This is due to the strong absorption in the surface region,

and indicates that a significant part of the fusion cross-section is from the inelastic channels, and so cannot be modelled in terms of an elastic-channel local potential. A full explanation of the fusion cross-section and spin distribution may therefore require the EOM to be extended to include potentials in some non-elastic channels.

These limitations of the EOM can be seen as limitations in the applicability of the concept of a local, smooth l-independent potential to heavy-ion fusion near the Coulomb barrier. This is a stronger test of the usefulness and range of applicability of the concept than simply verifying the existence of such a potential fitting the elastic scattering cross-section. In this case, as my analysis has shown, the exclusion of the non-elastic channels has led to a discrepancy between the predictions of the EOM and the BPM, which has demonstrated some of the limitations of a local l-independent potential obtained by inverting only the elastic scattering S-matrix.

5.5 Comparison of the one-nucleon transfer DPP with and without coupling between the excitation states in the transfer partitions

As a complement to the main investigations, this section will briefly note the difference in the inverse DPPs for one-nucleon transfer which results if the couplings between the excited states in the transfer partitions ^{62}Ni(^{16}O,^{17}O)^{61}Ni and ^{62}Ni(^{16}O,^{15}N)^{63}Cu are either excluded or included; these DPPs will be referred to as $V_{\rm exc}^{\rm 1NT}$ and $V_{\rm inc}^{\rm 1NT}$

respectively. The inelastic excitation states in the transfer partitions are specified in Section 5.1.

The distinction between $V_{\rm exc}^{\rm 1NT}$ and $V_{\rm inc}^{\rm 1NT}$ is an important one—the one-nucleon transfer DPPs presented in Sections 5.2 and 5.6 are not the same, since one of them has been inverted from a CRC S-matrix calculated with the couplings between the inelastic excitation states of the transfer partition included, and the other with them excluded. Fig. 5.36 shows the S-matrices for the potentials in Fig. 5.38. As expected, there is increased absorption due to the included channels in the transfer partitions, and the behaviour of the argument indicates increased attraction in the real potential for $V_{\rm inc}^{\rm 1NT}$ compared to $V_{\rm exc}^{\rm 1NT}$, which agrees with the inverse DPP in Fig. 5.39.

Fig. 5.37 displays the cross-sections for $V_{\rm exc}^{\rm 1NT}$ and $V_{\rm inc}^{\rm 1NT}$, compared with that for the bare potential. In the angular region between 80°–90°, the cross-section for $V_{\rm inc}^{\rm 1NT}$ actually shows slightly less absorption than that for $V_{\rm exc}^{\rm 1NT}$, although for the backward angles it shows the expected behaviour of increased absorption. To clarify this difference, a direct comparison is shown in Fig. 5.38 between the bare potential, $V_{\rm exc}^{\rm 1NT}$ and $V_{\rm inc}^{\rm 1NT}$. In Fig. 5.39, the bare potential has been subtracted so the DPPs can be directly compared. As Fig. 5.38 shows, the imaginary part of $V_{\rm exc}^{\rm 1NT}$ is close to the bare potential in the interior radial region ($r < 8$ fm). It is slightly less absorptive in a narrow region around $r \sim 8.2$ fm, has a shallow absorptive well up to 0.015 MeV deep between 8.3 and 9 fm, a broad, slightly less absorptive hump at about 9 fm, and a deeper absorptive well up to 0.035 MeV deep between about 9 and 10.5 fm. The potential which includes the coupling with the excited states in the transfer partitions,

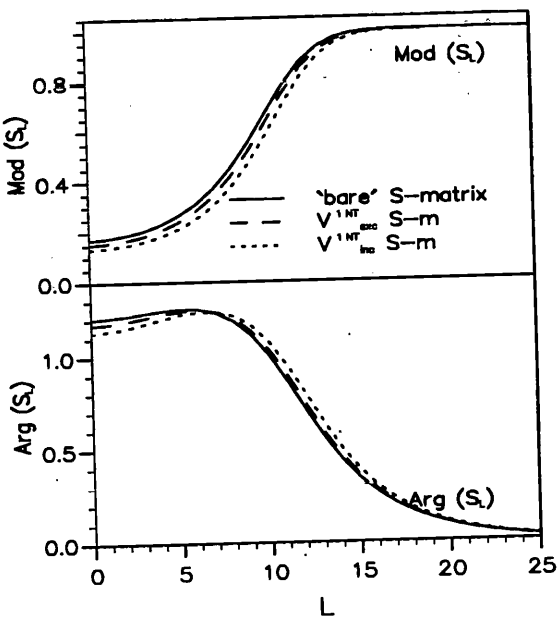

Figure 5.36: Comparison between the S-matrices for $V_{\text{exc}}^{\text{1NT}}$ and $V_{\text{inc}}^{\text{1NT}}$.

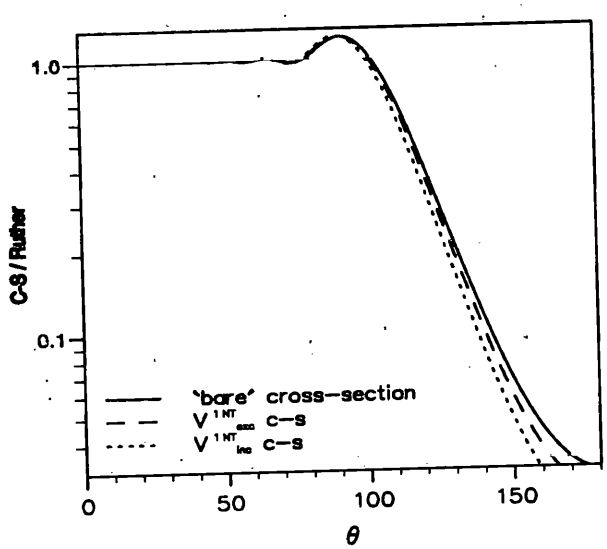

Figure 5.37: Comparison between the cross-sections for $V_{\text{exc}}^{\text{1NT}}$ and $V_{\text{inc}}^{\text{1NT}}$.

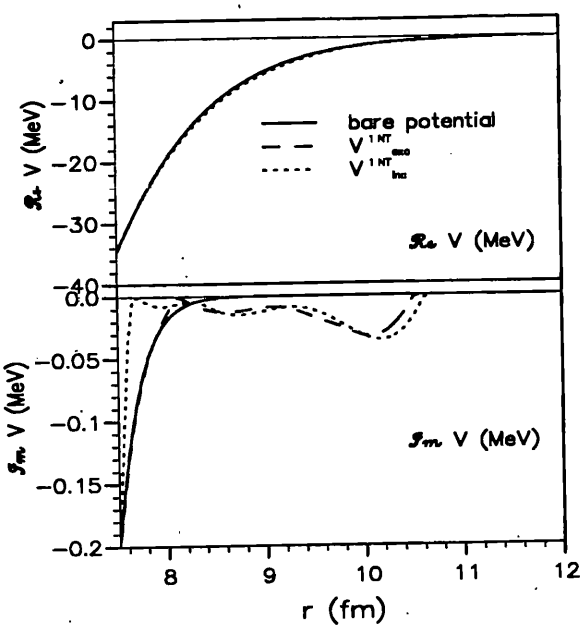

Figure 5.38: Comparison between the inverse potentials for one-nucleon transfer excluding ($V_{\rm exc}^{\rm 1NT}$) and including ($V_{\rm inc}^{\rm 1NT}$) excited states in the transfer partition, for ^{16}O+^{62}Ni at $E_{\rm lab} = 42$ MeV.

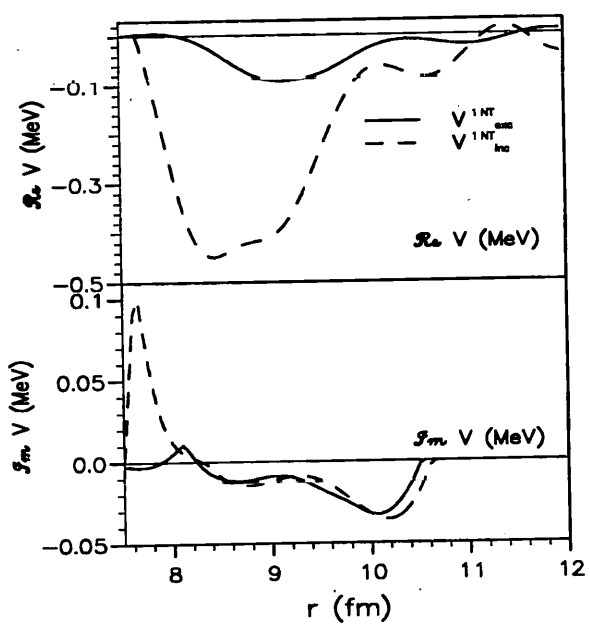

Figure 5.39: As in the previous Figure, with the bare potential subtracted to give the DPPs.

$V_{\rm inc}^{\rm 1NT}$, is rather different, however. It is less absorptive in the interior than the bare potential between $r = 7.5$ and 8 fm, which is somewhat surprising. However, for $r > 8$ fm, it follows the shape and magnitude of $V_{\rm exc}^{\rm 1NT}$ quite closely, apart from being shifted outwards by about 0.15 fm. The differences can be seen even more clearly in Fig. 5.39, where the bare potential has been subtracted to give the DPPs. The emissive peak in the imaginary part of $V_{\rm inc}^{\rm 1NT}$ between 7.5 and 8 fm is very distinctive, as is the increased attractive well in the real part.

5.6 An investigation into the additivity of the one-nucleon transfer DPPs

Introduction. The fact that under particular circumstances the DPPs are expected to contribute additively to the non-local potential can clearly be shown by writing the DPP explicitly in terms of Green's functions. We choose a particular channel, in this case the elastic channel, and we write the Schrödinger equation:

$$(T + v_{11} - E_1)u_1 = -\Sigma_i(v_{1i} - E_i)u_i, \tag{5.28}$$

where $T = (-\hbar^2/2\mu)\nabla^2$. Since we are assuming that all coupling between the non-elastic channels is zero, it follows (see Section 4.1) that the non-diagonal elements in the summation are zero, so $(T + v_{ii} - E_i)u_i = -(v_{i1} - E_1)u_1$. This can be written as $u_i = -G_i(v_{i1} - E_1)u_1$, where G_i is a Green's operator which is highly non-local and

l-dependent. Inserting this into Eq. 5.28 gives

$$(T + v_{11} - E_1)u_1 = -\Sigma_i(v_{1i} - E_i)G_i(v_{i1} - E_1)u_1. \tag{5.29}$$

Defining

$$\tilde{v}_{11} \equiv v_{11} + \Sigma_i(v_{1i} - E_i)G_i(v_{i1} - E_1), \tag{5.30}$$

the Schrödinger equation can be written as $(T + \tilde{v}_{11} - E_1)u_1 = 0$.

It is evident from Eq. 5.30 that 'switching off' the coupling between the channels which are coupled to the elastic channel would lead to the coupled channels contributing additively to the non-local potential. Whether this would remain true for the local-equivalent l-independent dynamic polarization potentials is an important question, relating to issues such as the degree of non-locality and l-dependence in the underlying potential, and to the very existence of an l-independent local potential which is smooth and well-behaved *and* an accurate fit to CRC S-matrix elements and cross-sections. We examined one-nucleon transfer in ^{16}O+^{62}Ni at 42 MeV and 56 MeV. The corresponding DPP can be subdivided into two components: neutron-pickup (^{16}O+^{62}Ni$\rightarrow^{17}$O+^{61}Ni) and proton-stripping (^{16}O+^{62}Ni$\rightarrow^{15}$N+^{63}Cu). There are therefore three DPPs to be found: $V_{\rm DPP}^{\rm 1nt}$, due to the combined effects of neutron-pickup and proton-stripping, $V_{\rm DPP}^{\rm n-p}$, due to neutron-pickup alone, and $V_{\rm DPP}^{\rm p-s}$, due to proton-stripping alone. This CRC analysis does not include the excited states of the transfer partitions, since the coupling between states would invalidate the assumption that the underlying potentials are additive. When there is no coupling between the channels that are themselves

coupled to the elastic channel, as in this case, $\mathcal{V}_{\rm DPP}^{\rm 1nt} = \mathcal{V}_{\rm DPP}^{\rm n-p} + \mathcal{V}_{\rm DPP}^{\rm p-s}$, where the $\mathcal{V}_{\rm DPP}$s are in principle non-local and l-dependent. However, the DPPs, $V_{\rm DPP}$, that are obtained by the inversion procedure are local equivalent and l-independent, and may therefore not necessarily be additive. The degree to which they depart from the property of additivity is an indication of the extent of such l-dependence and non-locality, and, given an accurate inversion procedure, testing whether or not the DPPs are additive could be used as an indicator of significant l-dependence in the underlying 'true' potential.

The one-nucleon transfer, neutron-pickup and proton-stripping DPPs at 42 MeV, obtained by inversion. The starting reference potential (SRP) for the inversions was the bare potential used in the CRC calculations — the un-normalised double-folding real potential of Keeley *et al.* [47] and a Woods-Saxon-squared imaginary potential (with $WS = 40$ MeV, $a_w = 0.4$ fm and $r_w = 1.0$ fm). The inverse potentials will be designated as $V_{\rm inv}$, while the actual DPPs, $V_{\rm DPP}$, are obtained by subtracting the bare potential from $V_{\rm inv}$; e.g., $V_{\rm DPP}^{\rm 1nt} = V_{\rm inv}^{\rm 1nt} - V_{\rm bare}$. Accurate inversions were obtained. At 42 MeV, the one-nucleon transfer potential $V_{\rm inv}^{\rm 1nt}$ had $\sigma^2 = 0.357 \times 10^{-2}$, the neutron-pickup potential $V_{\rm inv}^{\rm n-p}$ had $\sigma^2 = 0.574 \times 10^{-3}$, and the proton-stripping potential $V_{\rm inv}^{\rm p-s}$ had $\sigma^2 = 0.241 \times 10^{-2}$, where σ^2 measures the quality of fit to the elastic S-matrix produced by CRC calculations, as defined in Section 3.1.3 of this thesis.

As Fig.5.40 shows, the imaginary part of $V_{\rm inv}^{\rm 1nt}$ at 42 MeV only significantly differs from the bare potential between about 7.5 and 11 fm. There is less absorption than the bare potential between 7.8 and 8.2 fm, but greater absorption over a wide range of

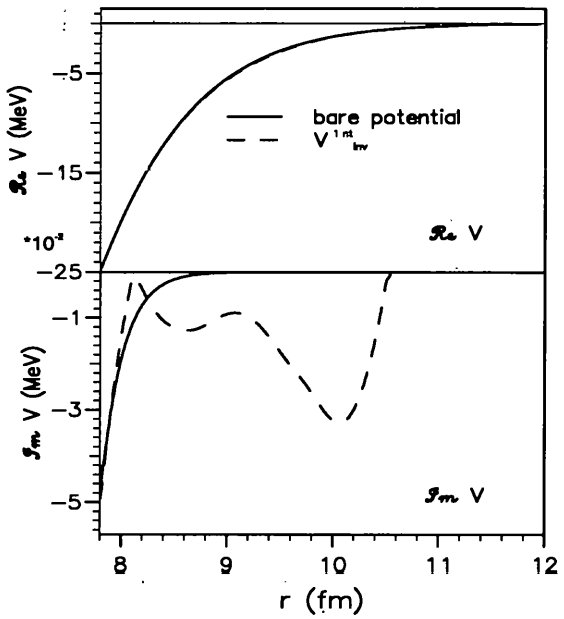

Figure 5.40: The inverse potential $V_{\rm inv}^{\rm 1nt}$ for one-nucleon transfer for ^{16}O+^{62}Ni at $E_{\rm lab}$ = 42 MeV. The scale for the imaginary part (but *not* the real part) is 10^{-2}.

radii. There is a shallow well at 8.5 fm, followed by a decrease in absorption at about 9 fm, followed by a deep well at about 10 fm. The effect of coupling to the one-nucleon transfer channels can therefore be modelled in the imaginary part by a potential which is surface-peaked at about 10 fm, which is the strong absorption radius for this case. This is what is expected for this type of direct reaction, although the detailed radial shape of the DPP cannot be predicted *a priori*. Because the real part of the bare potential is much greater than the imaginary part at these radial values, it might appear from Fig. 5.40 that the real DPP is negligible compared to the imaginary DPP; in fact, it is actually larger in magnitude, as Fig. 5.45 shows.

The inversion used 28 gaussian basis functions, and the fit to the S-matrix elements is shown in Fig. 5.41; it is very accurate, and cannot be visually distinguished

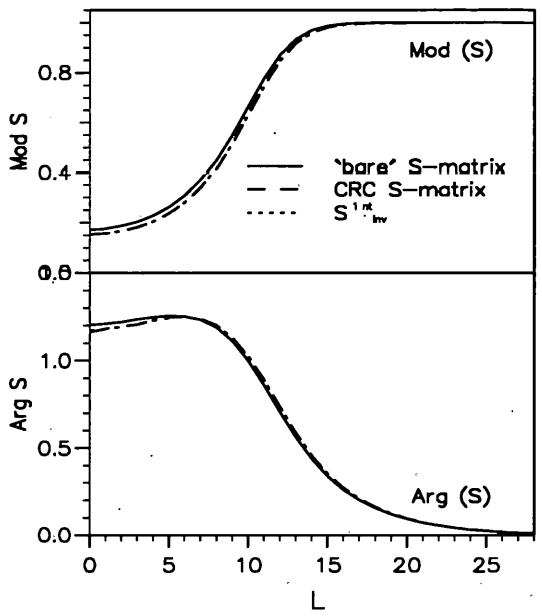

Figure 5.41: The inverse fit to the CRC-calculated target S-matrix, compared with the 'bare potential' S-matrix, for one-nucleon transfer for ^{16}O+^{62}Ni at $E_{\rm lab} = 42$ MeV.

from the target S-matrix over most of the l-range. There is therefore strong confidence that the physical features of the CRC-calculated S-matrix have been captured by the inverse potential.

The fit of $V_{\rm inv}^{\rm 1nt}$ to the cross-section produced by the one-nucleon transfer CRC calculations is shown in Fig. 5.42. It cannot be visually distinguished from the CRC cross-section over the entire angular range. This is also true for the neutron-pickup and proton-stripping inverse potentials.

The one-nucleon transfer channels consist of two components: the neutron-pickup and the proton-stripping channels. The elastic S-matrices for these channels were calculated separately using FRESCO [45] and the inverse potentials are shown in Figs. 5.43 and 5.44. The proton-stripping inverse potential is much deeper than the neutron-

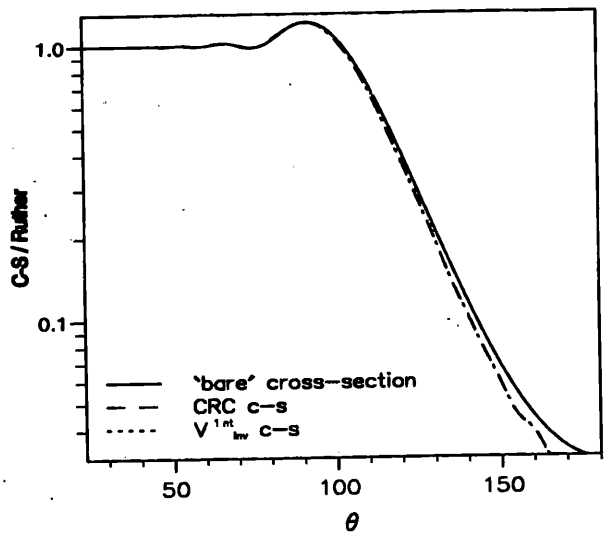

Figure 5.42: The inverse fit to the CRC-calculated cross-section, compared with the 'bare potential' cross-section, for one-nucleon transfer for $^{16}O+^{62}Ni$ at $E_{lab} = 42$ MeV.

pickup potential in the imaginary part.

The imaginary part of the neutron-pickup potential V_{inv}^{n-p} has, like V_{inv}^{1nt}, less absorption for $r \leq 8.2$ fm, and greater absorption for larger radii. There are two minima, at 8.6 fm and 10 fm, separated by a region of decreased absorption.

The imaginary part of the proton-stripping potential V_{inv}^{p-s} is more absorptive than the bare potential between about 7.6 fm and 8.3 fm, with the maximum difference at about 8 fm. Beyond 8.3 fm, the potential is less absorptive than the bare potential. This radial shape is significantly different from that of both V_{inv}^{1nt} and V_{inv}^{n-p}, and is much shorter-range, being peaked at about 8 fm rather than 10 fm.

Fig. 5.45 shows the DPPs for all three cases at 42 MeV, obtained by subtracting

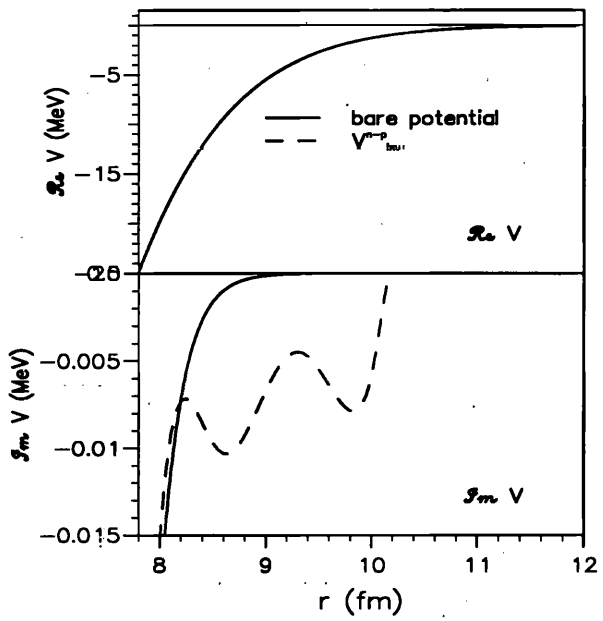

Figure 5.43: The inverse potential, $V_{\rm inv}^{\rm n-p}$, for neutron-pickup for ^{16}O+^{62}Ni at $E_{\rm lab} = 42$ MeV.

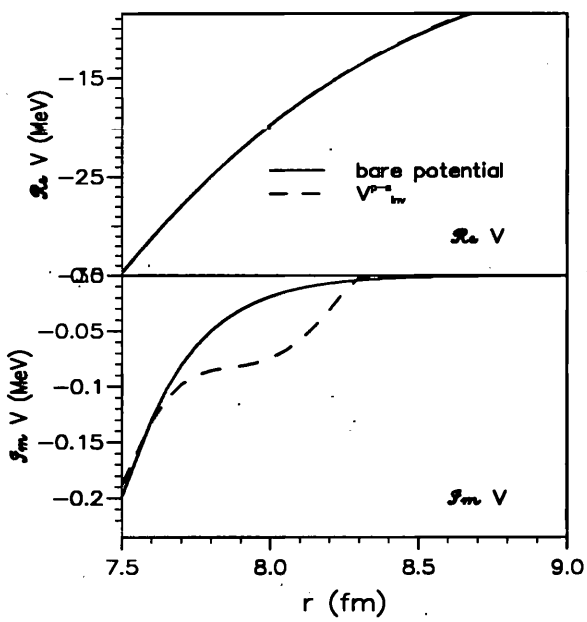

Figure 5.44: The inverse potential, $V_{\rm inv}^{\rm p-s}$, for proton-stripping for ^{16}O+^{62}Ni at $E_{\rm lab} = 42$ MeV.

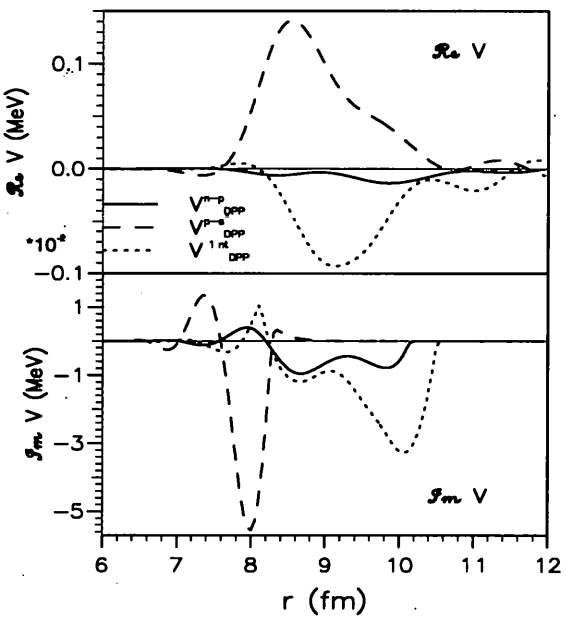

Figure 5.45: The inverse DPPs for neutron-pickup, proton-stripping and the total one-nucleon transfer for ^{16}O+^{62}Ni at $E_{\rm lab}$ = 42 MeV. The scale for the imaginary part is 10^{-2}. The solid curve is for the neutron-pickup, the dashed curve for the proton-stripping and the dotted curve for the total one-nucleon transfer DPP.

the bare potential from the inverse potentials. Both the real and imaginary parts of the DPPs are peaked between about 8 and 10 fm, as expected for a direct reaction such as particle transfer. The real parts are about three times greater than the imaginary parts. The total one-nucleon transfer DPP, $V_{\rm DPP}^{\rm 1nt}$, has an attractive real part, peaked at 9 fm and reaching a maximum depth of about 0.1 MeV, while its imaginary part has an emissive peak at 8 fm, followed by a shallow absorptive well at 8.5 fm, and a second, deeper absorptive well at 10 fm, reaching a maximum depth of about 0.035 MeV. The neutron-pickup DPP, $V_{\rm DPP}^{\rm n-p}$, follows a similar radial shape in both the real and imaginary parts, but is significantly shallower, especially in the absorptive well at 10 fm, and in the real part at all radii. The proton-stripping DPP, $V_{\rm DPP}^{\rm p-s}$, is qualitatively different from both the neutron-pickup and the total one-nucleon transfer DPPs. It has a strongly repulsive real part peaked at 8.5 fm with a magnitude of about 1.5 MeV. Its imaginary part has a small emissive peak at 7.5 fm, a strongly absorptive well at 8 fm (reaching a depth of 0.06 MeV), followed by a small emissive peak at 8.5 fm, falling to zero at larger radii.

It is clear that, given the accuracy of the inverse potentials' fit to the CRC-calculated elastic S-matrices, the local-equivalent l-independent DPPs are not additive; that is, $V_{\rm DPP}^{\rm 1nt} \neq V_{\rm DPP}^{\rm n-p} + V_{\rm DPP}^{\rm p-s}$. Since the underlying non-local l-dependent DPPs are additive in the present case, it follows that the non-additivity of the inverse DPPs is due to a significant degree of l-dependence and/or non-locality in the underlying potential. Indded, since the DPPs here are so small, we would expect them to be additive here if anywhere. It is to be expected that such underlying l-dependence would result in some

oscillatory characteristics in the local l-independent DPPs, and this does seem to be the case, especially in the imaginary part. The proton-stripping imaginary DPP exhibits this particularly clearly, with its alternating regions of absorption and emission.

Comparison of the DPPs at 42 MeV and 56 MeV. As an exploration of the energy-dependence of the DPPs, and as a check on the reliability and accuracy of the inversions, I performed the same CRC calculations for $^{16}O+^{62}Ni$ at 56 MeV, and inverted the CRC elastic S-matrix elements to obtain the potentials corresponding to neutron-pickup, proton-stripping and the total one-nucleon transfer at 56 MeV.

The inversions were more difficult than at 42 MeV, the values of σ^2 being 0.717×10^{-2} for the total one-nucleon transfer, 0.756×10^{-2} for neutron-pickup, and 0.7765×10^{-2} for proton-stripping. This is probably due to the fact that the strong absorption radius is farther out at the higher energy, and $|S_l| \sim 0$ for $l \leq 15$. The values of the argument of $S(l)$ are therefore not well-defined for $0 < l \leq 15$ and are dominated by numerical noise from the CRC calculations. The inversion procedure therefore cannot and should not fit these S-matrix elements, so higher values of σ^2 are to be expected.

Fig. 5.46 presents the inverse potentials for the total one-nucleon transfer at 56 MeV, $V_{\rm inv}^{\rm 1nt}$, compared with the equivalent potential at 42 MeV. The 56 MeV inverse potential is also strongly peaked at 10 fm, but is deeper. However, the shallow absorptive well at 8.5 fm in the 42 MeV potential is missing at the higher energy. The DPPs themselves $V_{\rm DPP}^{\rm 1nt}$, are shown in Fig. 5.47. The real DPP has a similar radial shape at both energies: a deep attractive well at 8.5–9 fm, and a smaller emissive peak at 7.5

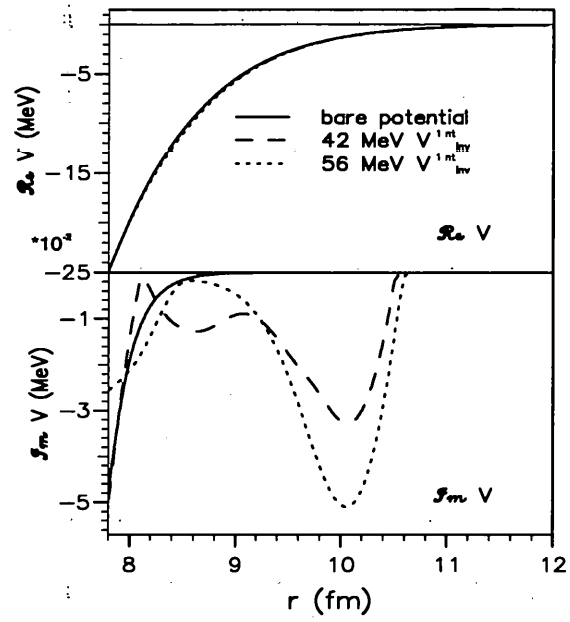

Figure 5.46: The inverse potentials, $V_{\rm inv}^{\rm 1nt}$, for one-nucleon transfer for ^{16}O+^{62}Ni at $E_{\rm lab}$ = 42 and 56 MeV. The scale for the imaginary part is 10^{-2}.

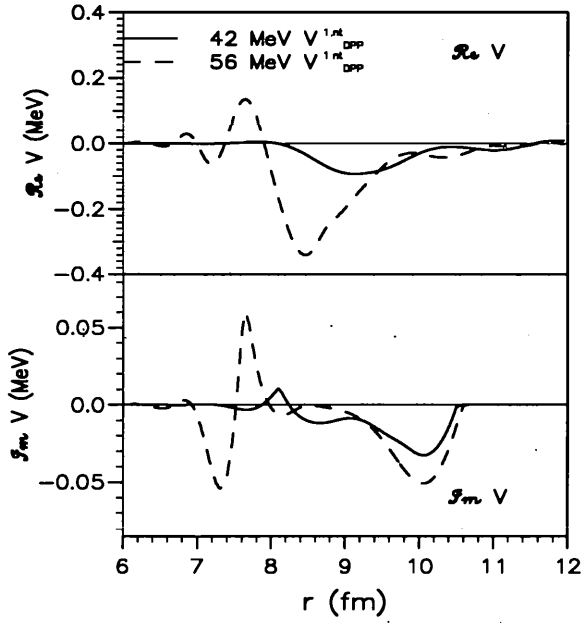

Figure 5.47: The inverse DPPs, $V_{\rm DPP}^{\rm 1nt}$, for one-nucleon transfer for ^{16}O+^{62}Ni at $E_{\rm lab}$ = 42 and 56 MeV.

fm. The higher energy DPP is deeper that at 42 MeV, and has oscillations between 6 and 7.5 fm. This may be due to some l-dependence of the underlying potential. The imaginary part of the 56 MeV DPP has similar oscillations in the same radial range, but also exhibits the same radial features as the 42 MeV DPP: a deep absorptive well at 10 fm, a shallow well at 8 fm, and a large emissive peak at 7.5–8 fm.

The strong similarities between the radial shapes of the DPPs at the two energies indicates that the radial shape has been well-determined by the inversion procedure; the differences, mainly in the magnitude of the DPPs and the position of the radial features, can be attributed to the energy dependence of the dynamic polarization potentials.

The inverse potentials at both energies for neutron-pickup, $V_{\rm inv}^{\rm n-p}$, are shown in Fig. 5.48. The 56 MeV potential is more strongly peaked at 10 fm, and the shallow absorptive well at 8.5 fm in the 42 MeV potential has become a shallow plateau in the 56 MeV potential. The real part of the neutron-pickup DPP (shown in Fig. 5.49) is much more oscillatory at 56 MeV, but is still on average attractive and surface-peaked, although much deeper than the 42 MeV real part. The imaginary DPP is also deeper at the higher energy, but has the same radial features at both energies: an absorptive well at about 10 fm, an emissive peak at 8 fm, and an absorptive well at 7.5 fm (very much deeper at 56 MeV than at 42 MeV). The 56 MeV imaginary DPP is oscillatory at lower radii.

The proton-stripping case is shown in Figs. 5.50 and 5.51. At both energies, the imaginary part of the inverse potential $V_{\rm inv}^{\rm p-s}$ is more absorptive than the bare potential between about 7.5 fm and 8.5 fm at 42 MeV, and between 7 fm and 8 fm at 56 MeV.

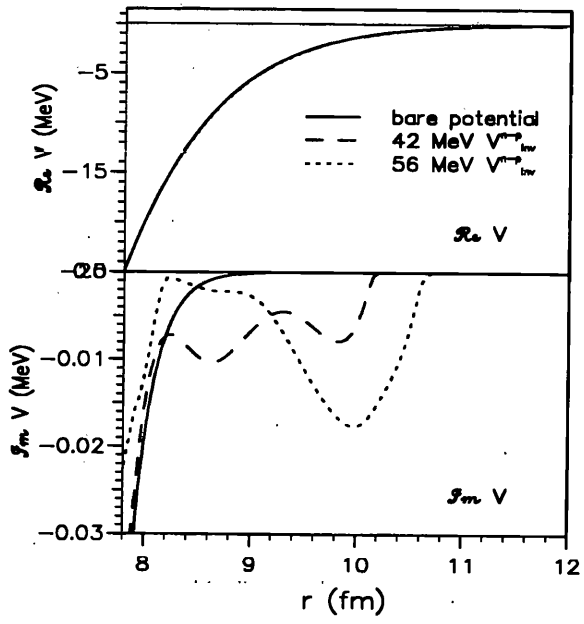

Figure 5.48: The inverse potentials, $V_{\rm inv}^{\rm n-p}$, for neutron-pickup for ^{16}O+^{62}Ni at $E_{\rm lab}$ = 42 and 56 MeV.

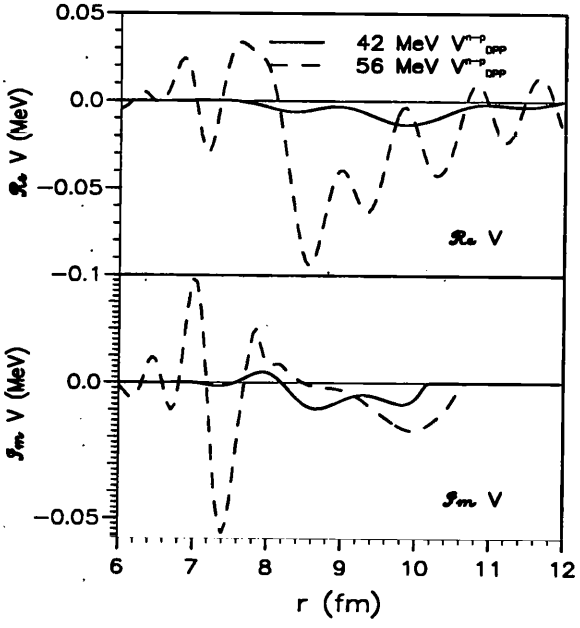

Figure 5.49: The inverse DPPs, $V_{\rm DPP}^{\rm n-p}$, for neutron-pickup for ^{16}O+^{62}Ni at $E_{\rm lab}$ = 42 and 56 MeV.

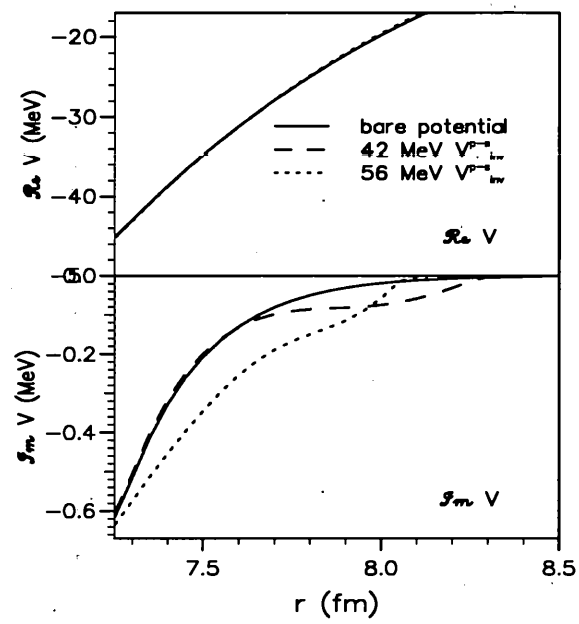

Figure 5.50: The inverse potentials, $V_{\rm inv}^{\rm p-s}$, for proton-stripping for ^{16}O+^{62}Ni at $E_{\rm lab}$ = 42 and 56 MeV.

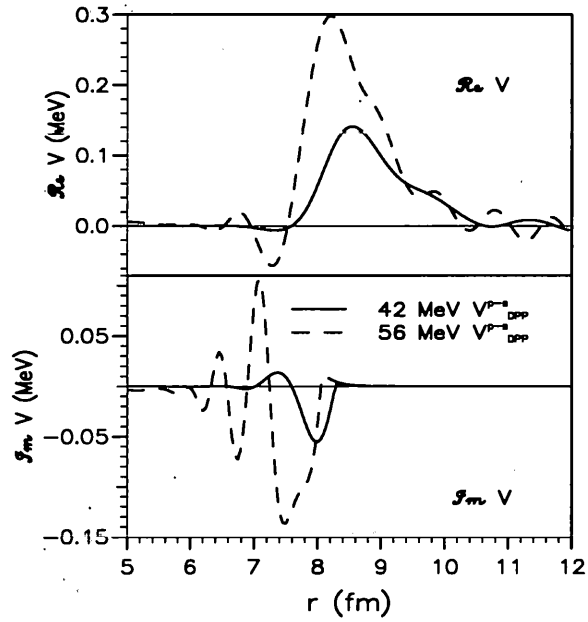

Figure 5.51: The inverse DPPs, $V_{\rm DPP}^{\rm p-s}$, for proton-stripping for ^{16}O+^{62}Ni at $E_{\rm lab}$ = 42 and 56 MeV.

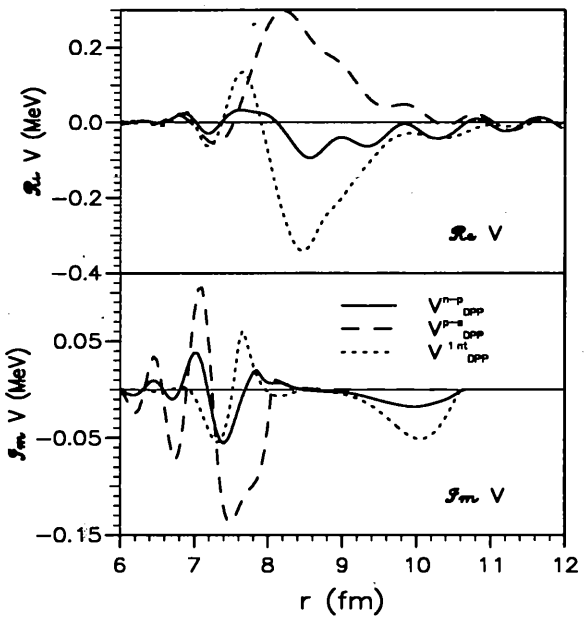

Figure 5.52: The inverse DPPs for neutron-pickup, proton-stripping and the total one-nucleon transfer for ^{16}O+^{62}Ni at $E_{\rm lab} = 56$ MeV.

Both potentials fall to zero very quickly, indicating an emissive peak in the surface region of the DPP. The proton-stripping potential has a very similar radial shape at both energies, and can therefore be said to be well-defined by the inversion procedure. The DPPs themselves, shown in Fig. 5.51, bear this out. The real part at both energies is strongly repulsive and are both surface-peaked between 8 and 9 fm, although the 56 MeV real DPP is both deeper and more oscillatory. The imaginary part is slightly shorter-range and deeper at the higher energy, but otherwise has the same basic radial features: a small emissive peak at 8.5 fm at 42 MeV and 8 fm at 56 MeV, an absorptive well at 8 fm at 42 MeV and 7.5 fm at 56 MeV, an emissive peak at 7.5 fm and 7 fm respectively, and an absorptive well at 7 fm and 6.5 fm respectively. The 56 MeV imaginary DPP is slightly oscillatory.

All three DPPs at 56 MeV, for the neutron-pickup, the proton-stripping and the full one-nucleon transfer, are compared in Fig. 5.52. It is clear that the DPPs for neutron-pickup and for proton-stripping do not add to give the total one-nucleon transfer DPP. As is the case at 42 MeV, $V_{\rm DPP}^{\rm lnt} \neq V_{\rm DPP}^{\rm n-p} + V_{\rm DPP}^{\rm p-s}$ at 56 MeV either.

Conclusions. There are two main results of this investigation: the determination of the detailed radial shape of the local l-independent one-nucleon transfer DPP, including its components, the neutron-pickup and proton-stripping DPPs, and the non-additivity of these DPPs. These two results are in fact related.

It is clear that the DPPs, which accurately fit the CRC S-matrix elements, do not have a simple radial form. In standard optical model analyses, direct-reaction DPPs such as that for one-nucleon transfer are usually approximated by surface-peaked Woods-Saxon-based forms. These generally give only approximate fits to CRC-calculated cross-sections or S-matrix elements, and their use assumes negligible l-dependence or non-locality in the underlying potential. It is clear from the inverse potentials presented here that there can be significant l-dependence in the dynamic polarization potential for heavy ion scattering even when only one or two channels are open, and this reveals itself both in the radial shape of the DPPs, which are not simple, and in the fact that the DPPs are not additive.

In my opinion, this puts into doubt the appropriateness of optical model fitting using potentials with simple, smooth radial forms for heavy ion scattering. Since such potential forms give only an approximate fit to S-matrices or cross-sections, the con-

clusion could be reached that the underlying potential has no significant l-dependence when in fact a more accurate fit with a potential radial shape which is allowed to vary freely would show evidence of such l-dependence. Of course, there is no guarantee that even if a smooth potential is found which accurately fits a given S-matrix, the underlying potential is not significantly l-dependent. If the l-dependence takes a simple form, as in the BGKP Coulomb excitation DPP (see Section 5.3 of this thesis), there may be a smooth and well-behaved l-independent local potential which fits the same S-matrix elements. In most physically realistic cases, however, the l-dependence is not simple, and will reveal itself in the l-independent local-equivalent potential in the form of radial oscillations, as in the DPPs presented here.

Chapter 6

Conclusions

The first part of this thesis presented the iterative-perturbative inversion method, and applied that inversion method to investigate the phenomenological potentials associated with heavy ion elastic scattering; specifically the cases of $^{16}O+^{12}C$ at 608 MeV and $^{12}C+^{12}C$ between 159 and 2400 MeV.

It was found that the PIPS inverted potentials produced by the two stage inversion procedure were preferable to both the more usual Woods-Saxon potentials and the potentials inverted from MWB S-matrices. This was because the fit to the experimental data was better (values of χ^2/N of 1 or 2 were typically achieved), and also because of their consistency with energy. This was partly achieved by the flexibility of the inverse potentials—the Woods-Saxon potential has a fixed radial form, and the double-folding potential changes only its normalisation parameter with energy, whereas the effects which renormalisation is intended to account for are expected to be radius dependent (e.g., the DPPs for nucleon transfer). This means that if there are several 'families'

of potential, all of which give equally good fits to the scattering data (corresponding to local minima of χ^2/N in the parameter space), potentials found using conventional optical model fitting when applied over a range of energies might give potentials at each energy which do not belong to the same 'family'. That is, a local rather than a global minimum of χ^2/N may be found in the fitting or inversion procedure, while a different local minimum might be found at a nearby energy. It is therefore very useful to impose the constraint of smoothness and consistency with energy; furthermore, the wide range of possible basis functions and starting reference potentials (SRPs) for the IP inversion procedure made it possible to explore the parameter space and find the global rather than local minima in χ^2/N. The standard fitting procedures, such as Woods-Saxon, are more constrained in the parameter space and are perhaps more easily trapped in local minima.

Using the IP inversion method, a value of $\chi^2/N \sim 1$ is achievable with good data, so that almost the full information content of the scattering cross-section data is contained in the inverted potentials. Such an accurate inversion method can serve as a tool to probe the reliability and physical reasonableness of the data. For example, if the data points do not follow any smooth curve due to an underestimation of the statistical errors, then an attempt to fit those data with a smooth S-matrix will be very difficult. The corresponding inverted potential may well, if a fit with χ^2/N close to 1 is insisted on, exhibit non-physical features near the strong absorption radius. If these oscillations are not consistent with potentials for nearby energies, and no strong l-dependence is expected, then this can be taken as an indication of a problem with

the data. However, where the errors have been underestimated, it is possible with the iterative-perturbative method to obtain smooth and physically reasonable potentials which fit the scattering data, so long as higher values of χ^2/N are tolerated. This was the case with the analysis of ^{12}C on ^{12}C at 161.1 MeV (see Section 3.3). Even systematic errors in the scattering data can be detected using this inversion method, as appears to be the case with ^{12}C on ^{12}C at 360 MeV where, in order to fit the data the PIPS S-matrix had a slight negative tail at large l-values, corresponding to a slight repulsive tail in the inverted potential. The various standard parametrized forms of S-matrix or potential fitting could not have shown such non-physical features, being constrained by their fixed form, and could therefore not have indicated such a problem with the data, other than their high values of χ^2/N. The likelihood is that the difficulties are caused by uncertainties in the overall normalisation of the data.

The power of the IP inversion method, especially as part of a two stage inversion procedure, is demonstrated by the fact that in all the investigations described here we have used the experimental errors, whereas other authors [19, 20] have applied equal weights at each angle (usually 10 percent errors). This means that the inversion procedure used in this thesis is better for investigating the quality of scattering data than alternative methods, since it can fit even the backward angles *with the experimental weights*. This inversion method therefore motivates experiments of greater precision and angular range, since physically reasonable potentials can be found which will fit those data accurately.

An interesting finding of my investigation of ^{12}C+^{12}C is that the MWB S-matrix

always gives, by accurate inversion, a potential which has a characteristic repulsive core. This repulsion only occurs for radii much less than the sensitive range around the strong absorption radius (SAR), and therefore cannot be said to be physically meaningful. It is almost certainly an artefact of the restrictive form of the MWB S-matrix, and the same feature was reported by Allen *et al.* [18] in their inversion of MWB S- matrices for $^{12}C+^{12}C$ and ^{16}O scattering at 1503 MeV, and the same repulsive core appeared in my inversion of the MWB S-matrix for $^{16}O+^{12}C$ at 608 MeV.

The inversion analysis of $^{12}C+^{12}C$ at 1016 MeV has produced further evidence in favour of the existence of an observable nuclear rainbow at about 10° to 12°, as claimed by some authors [38, 32]. This is because, although the Woods-Saxon fit has a ratio of $W/V \sim 1$ in the far surface, both the MWB and PIPS potentials are surface transparent (with $W/V < 0.2$ in the far surface), given the relatively high χ^2/N of about 7 of the Woods-Saxon fit, this surface transparency seems to be necessary for a good fit to the data, which allows the existence of an observable nuclear rainbow.

The second part of this thesis applied the method of 'CRC+inversion' to investigate the properties of the dynamic polarization potentials of $^{16}O+^{62}Ni$ at the Coulomb threshold, specifically the quadrupole Coulomb excitation DPP, and the fusion cross-section and spin distribution. Firstly, however, an apparent anomaly in the energy dependence of the potential had to be investigated to determine whether the energy dependence was intrinsic (e.g., due to channel coupling effects) or spurious (e.g., caused by the optical model fitting procedure).

The anomaly in $W(E)$ for $^{16}O+^{62}Ni$ at the Coulomb threshold observed by Keeley

et al. [47] was investigated using dispersion relation analysis. While such an analysis is dependent on some optical model potential, and shares the limitations of that model, it is a powerful method of checking the consistency of the energy dependence of the real and imaginary potentials, and has also been applied by us to $^{16}O+^{16}O$ scattering [49]. In the case presented here, I was able to show that the peak in $W(E)$ cannot be causally consistent with the corresponding $N_R(E)$ obtained by Keeley *et al.*. While Keeley *et al.*'s later analysis [52] demonstrated that it is certainly possible to produce a peak in $W(E)$ at about the right energy by coupling to an inelastic channel, they were unable to reproduce the actual peak obtained in their earlier optical model analysis either in magnitude or shape. My conclusion therefore is that the anomaly is almost certainly an artefact of the fixed geometry of the double-folding real potential or some other factor of the optical model fitting procedure which caused some spurious energy-dependence in the imaginary potential. A more general conclusion which can be drawn from this analysis is that dynamic polarization potentials obtained by optical model fitting can be unreliable, and therefore investigations of such DPPs using accurate, model-independent methods such as 'CRC+inversion' should not set too high a store on matching potentials obtained by optical model fitting.

My investigation of the analytic forms for the long-range Coulomb excitation DPP has indicated that such forms can be useful as the SRP for the iterative-perturbative inversion when fitting the large radial range with a smooth physically reasonable potential is difficult. (However, the existence of a 'shoulder' in $|S(l)|$ for $^{16}O+^{62}Ni$ at the Coulomb threshold meant that all inverse potentials had a slight emissive peak near

the SAR. This rendered the use of any long-range SRP ineffective, and so the Coulomb excitation DPP was not used as an SRP in any of the inversions presented here.) Furthermore, the comparison between the Love-Terasawa-Satchler (LTS) form, the Baltz-Glendenning-Kauffmann-Preuss (BGKP) form, and the coupled-channel calculation for quadrupole Coulomb excitation (CC) has shown how much the LTS form overestimates the absorption for heavy ions, due to the simplifying assumptions made by LTS. The BGKP form was shown to be closer to the coupled-channel calculation. An important result of the inversion was that a smooth l- independent potential could be found by inversion which almost exactly reproduces the S-matrix of a strongly l-dependent potential. The ability to compare directly the l-dependent and l-independent potentials, both of which accurately give the same S-matrix elements, is a useful by-product of the IP inversion procedure and the relative smoothness of the l-independent equivalent in this case can be interpreted as an interesting property of the l-dependent potential itself.

I investigated the fusion processes and partial wave fusion cross-section for ^{16}O $+^{62}$Ni at 42 MeV by applying the extended optical model (EOM) in conjunction with CRC calculations and IP inversion as an alternative to the barrier penetration model (BPM). DPPs representing contributions from various coupled reaction channels to the fusion of the nuclei were obtained as extremely accurate inversions from CRC-calculated S-matrix elements. These DPPs proved to be intermediate in shape between the strongly surface-peaked DPPs of other investigators [80] and the volume term of the bare potential. Their contribution to the spin distribution for fusion was therefore

in accordance, with regard to shape, with theoretical expectation, since they give only a single peak at high l-values. However, a non-physical result was that there was a long tail in the contribution from the inelastic DPP. While a moderately long tail is in accordance with the results of other EOM analyses [80, 81], the fact that it extends well beyond the l-value corresponding to the strong absorption radius suggests that the factor ξ^{inel}, which in the EOM is assumed to be constant, should actually vary with the radius, falling to zero at large r. The approach used in this thesis is a further extension of the EOM, since it modifies the simplifying assumption that the same proportion ξ of all DPPs will contribute to fusion by deducing separate values ξ^{inel} and ξ^{1NT}. The use of accurate inversion from CRC-calculated S-matrix elements allowed an important result to be obtained: that the magnitude of the fusion cross-sections are underestimated by the EOM, compared with the BPM predictions, by a factor of between 10 and 20. This is due to the strong absorption in the surface region and indicates that a significant part of the fusion cross-section is from the inelastic channels, and so cannot be modelled in terms of a purely elastic-channel local potential. I therefore conclude that a full explanation of the fusion cross-section and spin distribution for heavy ions may therefore require the EOM to be extended to include potentials in some non-elastic channels.

The investigation into the additivity of the one-nucleon transfer DPPs established two main results: (i) that the detailed radial shapes of the DPPs required to fit the CRC-calculated S-matrices are not simple and show evidence of oscillatory behaviour characteristic of strong l-dependence in the underlying potential, and (ii) that the

DPPs of the component channels do not add to give the total one-nucleon transfer DPP. These results are related, since the non-additivity of the local l-independent potentials is believed to be due to significant non-locality of the underlying potential. The use of simple radial forms for such heavy-ion DPPs in most optical model analyses is therefore shown to be problematical, since the use of such smooth, restricted radial forms presupposes negligible l-dependence in the underlying potential, and the results presented here indicate that even a few open channels can, in the case of heavy-ion scattering at least, give rise to significant l-dependence which usually manifests itself as complicated radial shapes in the local l- independent potentials. These radial shapes can be most effectively investigated using an accurate inversion procedure which makes no *a priori* assumptions about the radial shapes of the potentials.

Appendix A

Published papers

I have co-authored the following three published papers:

- S.G. Cooper, M.A. McEwan and R.S. Mackintosh, Phys. Rev. **C45** (1992) 770
- M.A. McEwan, S.G. Cooper and R.S. Mackintosh, Nucl. Phys. **A552** (1993) 401
- S. Ait-Tahar, R.S. Mackintosh and M.A. Russell, J. Phys. G: Nucl. Part. Phys. **21** (1995) 577

  Please note that I have changed my surname from McEwan to Russell.

Bibliography

[1] A. Messiah, *Quantum Mechanics*, Vols. I and II (North-Holland, Amsterdam, 1962)

[2] K. Chadan and P.C. Sabatier, *Inverse Problems in Quantum Scattering Theory* (Second Edition) (Springer, New York, 1989)

[3] H. Feshbach, Ann. Revs. Nucl. Sci **8**, 1959

[4] H. Feshbach, Annals of Phys. (N.Y.) **5** (1958) 357

[5] H. Feshbach, *ibid* **19** (1962) 287

[6] R.S. Mackintosh, J.Phys. G. **5** 1587 (1979)

[7] R. Lipperheide, R. Fiedeldey and H. Leeb, in *Advanced Methods in the Evaluation of Nuclear Scattering Data* (Springer, Berlin, 1985), p.249

[8] G.R. Satchler and W.G. Love, Phys. Reports **55C** (1979) 183

[9] A.M. Kobos, R.S. Mackintosh and J.R. Rook, Nucl. Phys. **A389** 205 (1982)

[10] R.S. Mackintosh, S.G. Cooper and A.A. Ioannides, Nucl. Phys. **A476** 287 (1988)

[11] S.G. Cooper and R.S. Mackintosh, Phys. Rev. **C43** 1001 (1991)

[12] J.A. McIntyre, K.H. Wang and L.C. Becker, Phys. Rev. **117** 1337 (1960)

[13] S.G. Cooper, program CSFIT, unpublished.

[14] E.K. May, M. Münchow and W. Scheid, Phys. Lett. **141B** 1 (1984)

[15] H. Leeb, W.A. Schnizer, H. Fiedeldey, S.A. Sofianos and R. Lipperheide, Inverse Problems **5** 817 (1989)

[16] R.S. Mackintosh and A.M. Kobos, Phys. Lett. **116B** 95 (1982)

[17] S.G. Cooper and R.S. Mackintosh, Inverse Problems, **5** 707 (1989)

[18] L.J. Allen, K. Amos, C. Steward and H. Fiedeldey, Phys. Rev. **C41** 2021 (1990)

[19] M.C. Mermaz, Z. Phys. **A 321** 613 (1985)

[20] M.C. Mermaz, B. Bonin, M. Buenerd and J.Y. Hostachy, Phys. Rev. **C34** 1988 (1986)

[21] S.G. Cooper and R.S. Mackintosh, Nucl. Phys. **A517** 285 (1990)

[22] M.A. McEwan, S.G. Cooper and R.S. Mackintosh, Nucl. Phys. **A552** (1993) 401

[23] S.G. Cooper, program IMAGO, unpublished.

[24] R.S. Mackintosh and A.M. Kobos, J. of Phys., **G5** 359 (1979)

[25] W.H. Press, B.P. Flannery, S.A. Teukolski and W.T. Vetterling, in *Numerical Recipes* (Cambridge University Press, 1989), p.52

[26] M.-E. Brandan *et al.*, Phys. Rev. **C34** 1484 (1986)

[27] M.-E. Brandan, Phys. Rev. Lett. **60** 784 (1988)

[28] R.C. Fuller, Phys. Rev. **12** 1561 (1975)

[29] M.-E. Brandan and G.R. Satchler, private communication.

[30] S. Kubono *et al.*, Phys. Lett. **127B** 19 (1983)

[31] A.J. Cole *et al.*, Phys. Rev. Lett. **47** 1705 (1981)

[32] M. Buenerd *et al.*, Nucl. Phys. **A424** 313 (1984)

[33] J.Y. Hostachy *et al.*, Nucl. Phys. **A490** 441 (1988)

[34] J.E. Poling *et al.*, Phys. Rev. **C13** 659 (1976)

[35] M.-E. Brandan and G.R. Satchler, Nucl. Phys. **A487** 477 (1988)

[36] M.El-Azab Farid and G.R. Satchler, Phys. Lett. **B146** 389 (1984)

[37] D.A. Goldberg and S.M. Smith, Phys. Rev. Lett. **29** 500 (1972)

[38] M. Buenerd *et al.*, Phys. Rev. **C26** 1299 (1982)

[39] C.W. de Jager *et al.*, Atomic Data and Nuclear Data Tables **14** 479 (1974)

[40] C. Steward *et al.*, Phys. Rev. **C51** 836 (1995)

[41] N. Ohtsuka *et al.*, Nucl. Phys. **A490** 715 (1988)

[42] M.-E. Brandan *et al.*, Phys. Rev. **C38** 673 (1988)

[43] R.S. Mackintosh *et al.*, Nucl. Phys. **A582** (1995) 283

[44] I.J. Thompson, Comput. Phys. Rep. **7** (1988) 167

[45] I.J. Thompson, program FRESCO

[46] L. West, Jr., K.W. Kemper and N.R. Fletcher, Phys. Rev. **C11** (1975) 859

[47] N. Keeley *et al.*, Nucl. Phys. **A 582** (1995) 314

[48] N. Keeley, private communication.

[49] S. Ait-Tahar, R.S. Mackintosh and M.A. Russell, J. Phys. G: Nucl. Part. Phys. **21** (1995) 577

[50] N. Keeley and K. Rusek, Phys. Rev. **C 56** (1997) 3421

[51] D. Pereira *et al.*, Phys. Lett. **B 220** (1989) 347

[52] N. Keeley *et al.*, Nucl. Phys. **A 603** (1996) 97

[53] I. Martel *et al.*, *ibid* **A 582** (1995) 357

[54] I. Martel *et al.*, *ibid* **A605** (1996) 417 (1985) 55

[55] W.G. Love, T. Terasawa and G.R. Satchler, Nucl. Phys. **A291** (1977) 183

[56] A.J. Baltz, N.K. Glendenning, S.K. Kauffman and K.Preuss, Nucl. Phys. **A327** (1979) 221

[57] M. Beckerman, Rep. Prog. Phys. **51** (1988) 1047–1103

[58] S. Landowne and S. C. Piper, Phys. Rev. C **29** 1352–7 (1984)

[59] S. Landowne and C.H. Dasso, Phys. Lett. **138B** 32–4 (1984)

[60] M. Beckerman *et al.*, Phys. Rev. Lett. **45** 1472–5 (1980)

[61] R.G. Stokstad *et al.*, Z. Phys. A **295** 269–86 (1980)

[62] R.G. Stokstad and E.E. Gross, Phys. Rev. **C23** (1981) 281

[63] H. Esbensen, Nucl. Phys. **A352** (1981) 147

[64] W. Reisdorf *et al.*, Phys. Rev. Lett. **49** (1982) 1811

[65] U. Jahnke *et al.*, Phys. Rev. Lett. **48** (1982) 17

[66] L.C. Vaz *et al.*, Proc. Intern. Conf. on Nuclear physics with heavy ions (Stony Brook, 1983)

[67] R.A. Broglia, Proc. Intern. Conf. on Heavy Ion Physics and Nuclear Physics (Catania 1983)

[68] R.A. Broglia *et al.*, Phys. Rev. **C27** (1983) 2433

[69] T. Udagawa, B.T. Kim and T. Tamura, Phys. Rev. **C32** (1985) 124

[70] M.J. Rhoades-Brown and P. Braun-Munzinger, Phys. Lett. **136B** (1984) 19

[71] A.B. Balantekin and N. Takigawa, Ann. Phys. (N.Y.) **160** (1985) 441

[72] P. Fröbich, R. Lipperheide and K. Möhring, Z. Phys. **B78** (1990) 325

[73] N. Yahlali, J. Díaz and T. Sami, Phys. Rev. **C53** (1996) 1845

[74] P.H. Stelson, Phys. Lett. **B205** (1988) 190

[75] A. Iwamoto and K. Harada, Z. Phys. **A326** (1987) 201

[76] J. Schneider and H.H. Wolter, Lecture Notes in Physics **317**: Heavy Ion Interactions Around the Coulomb Barrier (Springer Verlag) (1988) 14

[77] T. Udagawa, T. Tamura and B.T. Kim, Phys. Rev. **C39** (1989) 1840

[78] M.L. Halbert *et al.*, Phys. Rev. **C40** (1989) 2558

[79] G.R. Satchler *et al.*, Ann. of Phys. **178** (1987) 110

[80] G.R. Satchler *et al.*, Phys. Rev. **C41** (1990) 1869

[81] K.-I. Kubo, Nucl. Phys. **A534** (1991) 381

K.-I. Kubo, P. Manyum and P.E. Hodgson, Nucl. Phys. **A534** (1991) 393